University of Tennessee, Knoxville
TRACE: Tennessee Research and Creative Exchange

Doctoral Dissertations | Graduate School

12-2007

A Study of the Secondary Electrons

Yinghong Lin
University of Tennessee - Knoxville

Follow this and additional works at: https://trace.tennessee.edu/utk_graddiss

 Part of the Materials Science and Engineering Commons

Recommended Citation

Lin, Yinghong, "A Study of the Secondary Electrons. " PhD diss., University of Tennessee, 2007.
https://trace.tennessee.edu/utk_graddiss/228

This Dissertation is brought to you for free and open access by the Graduate School at TRACE: Tennessee Research and Creative Exchange. It has been accepted for inclusion in Doctoral Dissertations by an authorized administrator of TRACE: Tennessee Research and Creative Exchange. For more information, please contact trace@utk.edu.

To the Graduate Council:

I am submitting herewith a dissertation written by Yinghong Lin entitled "A Study of the Secondary Electrons." I have examined the final electronic copy of this dissertation for form and content and recommend that it be accepted in partial fulfillment of the requirements for the degree of Doctor of Philosophy, with a major in Materials Science and Engineering.

David C. Joy, Major Professor

We have read this dissertation and recommend its acceptance:

Philip D. Rack, Joseph E. Spruiell, Anthony J. Pedraza, Harry M. Meyer

Accepted for the Council:

Carolyn R. Hodges

Vice Provost and Dean of the Graduate School

(Original signatures are on file with official student records.)

To the Graduate Council:

I am submitting herewith a dissertation written by Yinghong Lin entitled *"A Study of the Secondary electrons"* I have examined the final electronic copy of this dissertation for form and content and recommend that it be accepted in partial fulfillment of the requirements for the degree of Doctor of Philosophy, with a major in Materials Science and Engineering.

David C. Joy, Major Professor

We have read this dissertation and recommend its acceptance:

Philip D. Rack

Joseph E. Spruiell

Anthony J. Pedraza

Harry M. Meyer

Accepted for the Council:

Carolyn R. Hodges

Vice Provost and Dean of the Graduate School

(Original signatures are on file with official student records)

A Study of the Secondary Electrons

A Dissertation Presented for

the Philosophy

Degree

The University of Tennessee, Knoxville

Yinghong Lin

December, 2007

Acknowledgements

At first I would like to thank my advisor Dr. David Joy for his always academic advisement and financial support on my research during the past 4 years. His kind help has come in many ways from coaching me on trivial experimental work to opening me chances to academic and industrial world. I could never make either academic achievements or mental maturity today I have without his consistent encouragements and patience.

During the work I had received numerous help from Dr. Harry Meyer in ORNL on not only operating the PHI 680 SAN but also communication with the PHI Electronics. Thanks him for making the instrument available to me for so many times through the busy schedules. So many helps I have received from international doctors and professors. I appreciate Dr. Ronald Negri in PHI Electronics for suggestions and explanations on the devices physics of the PHI instruments. Thanks to Dr. Tanuma S. for the discussion on the CMA structure. The public AES calibration software package Compro8 and the database of SASJ in Japan are important references of this thesis. Thanks to Dr. Philip Rack from UT for providing me the alloy samples. Special appreciation refers to Dr. Peter Cumpson in NPL in the United Kingdom for sharing their AES calibration software free of charge.

It was my great pleasure to work with my former and current group members Dr. Xiaohu Tang, Jing He, Dr. Satya Prasad, Dr. Yeong-Uk Co, Dr. Young Choi, Dr. Wei Li, Dr. Medhi , Jihoon Kim, Satya Bari, Sachin Deo, Ranjan , Kiran Jaladhi, Dr. Bernard Frost, Dr. Carolyn Joy, and Dr. John Dunlap. Numerous help have been received from them. Including Dr. Joy, Dr. Rack, and Dr. Meyer, I want to thank my other two committee members Dr. Anthony Pedraza and Dr. Joseph Spruiell for their consistent coach. Special thanks to our group secretary Jennifer Trollinger for her help in so many ways.

My deepest thanks go to my husband Daoyong Gao and my parents for their trust and encouragement. Thanks to my first baby who will be on this world in this August. He/she has been very cooperative during my process of writing thesis.

Abstract

Slow secondary electrons (SEs) (E<50 eV) are those emitted from a sample as the result of bombardment by energetic particles. They are the most important signal source for SEM and for other advanced microanalysis techniques. SE yield δ and spectrum N(E) are the two important parameters evaluating the capability of a sample on producing SEs and the energy distribution of SEs generated from the sample respectively. Measuring δ and N(E) is not easy since SEs are easily affected by sample surface condition and by experimental configuration. Though SE has been studied since its first find in 1902, experimental date of it are inconsistent and unsystematic. Theoretical models on the SE production are not well established.

To better understand the secondary electrons, an optimization of a scattered experimental SE yield database was carried out by fitting the data to a semi-empirical universal curve and by a Monte Carlo simulation. The profiles of SE yield versus beam energy and the values of SE excitation energy ε and mean SE escape depth λ were generated for 44 elements. An atomic shell filling effect was found on the maximum SE yields and the corresponding beam energies.

To obtain more accurate and systematic SE yield data, a novel experimental method by collecting electron spectra on an AES instrument (PHI 680 SAN) equipped with a cylindrical mirror analyzer (CMA) was developed. The principles of the CMA and the micro channel plate (MCP) in analyzing and multiplying electron signal were studied. The efficiency of the PHI 680 SAN in response to the electron energy in the range of 0~3200 eV was deduced to calibrate intensity of any as received spectrum.

Measurement on elements and the Cr-W and Cu-Au binary alloys were conducted. The measured SE yields were 50% lower than the optimized values but showed the atomic shell filling effect as expected. Both the SE and BSE yields of the binary alloys showed linear relationship with atomic percent of specimen constituents. Linear synthesis of the elemental SE spectra of the Cr-W alloys agreed well with the measured.

Table of Contents

List of Tables

List of Figures

List of Symbols

PE: primary electrons, incident electrons
SE: secondary electrons, secondaries
BSE: backscattered electrons
E_{PE}: primary energy
λ: mean free path length, SE mean attenuation length
δ: secondary electron yield
η: backscattered yield
σ: total electron yield, cross section
δ_{PE}: the number of SE released per PE,
δ_{BSE}: the number of SE released per BSE
β: the efficiency of BSE in generating secondaries relative to that of PE
E_F: Fermi energy
ϕ: work function
E_{SE}^m: most probable SE energy
Z: atomic number
MFP: mean free path
EMFP: elastic mean free path
IMFP: inelastic mean free path
SE_I: secondary electrons produced by the forward-traveling incident electrons
SE_{II}: secondary electrons produces by the backscattered electrons
SE3: secondary electrons generated from the SEM chamber and pole piece of the lens by irradiation of the high energy BSE from the sample.
FWHM: full width of half maximum
HRSEM: high resolution SEM
LVSEM: low voltage SEM
δ^m: maximum SE yield
E_{PE}^m: beam energy corresponding to δ^m
I_b: incident beam current
I_{sc}: specimen current
I_{scb}: specimen current when sample is biased
E_1, E_2: two beam energies for which σ=1. $E_1 < E_2$
VPSEM: variable pressure SEM
ESED: environmental secondary electron detector
GSED: gaseous secondary electron detector
Ω: solid angle
$d\sigma/d\Omega$: differential cross section respect to direction
$d\sigma/dE$: differential cross section respect to energy

α : screening factor in Rutherford cross section
N_a : Avogadro's number
ρ : density of the target in g/cm^3
A : atomic weight in g/mol
λ_{el} : elastic MFP
λ_{in} : inelastic MFP
dE/dS : stopping power of the target in $keV/(g/cm^2)$
J : mean ionization potential in keV
R : beam range
λ_{es} : SE escape depth
λ_{at} : SE attenuation length
RFS: retarding field analyzer
ARESES: angle resolved-SE-spectrometer
EEM: emission electron microscope
CMA: cylindrical mirror analyzer
CSA: concentric sector analyzer
AES: Auger electron microscope
SAN: scanning Auger nanoprobe
MCP: micro channel plate
CEM: channel electron multiplier
XPS: X-ray photoelectron spectroscope
FAT: fixed analyzer transmission work mode that is common in AES
FRR: fixed retard ratio work mode, the same as FAT
CRR: constant retard ratio work mode that is common in XPS
D: CMA energy dispersion constant
T(E): CMA transmission efficiency
W: optical transparency of the entrance window of CMA
T: spatial transmission of CMA
$\overline{\Omega}$: fraction of the effective solid angle subtended by the CMA entrance window
D(E): detection efficiency of the MCP detector
F: detection efficiency of the electronic system in PHI 680 SAN
Q(E): electron spectrum intensity response function of PHI 680 SAN system
$N_0(E)$: true spectrum
N(E): measured spectrum in PHI 680 SAN experienced collection efficiency deficiency
E_p : sweeping energy of the outer cylinder in the CMA

1. Chapter Ⅰ: Introduction

1.1 Why study secondary electrons

Secondary electrons (SEs or secondaries) are those electrons emitted from the sample surface with kinetic energy less than 50eV and are the result of bombardment by energetic particles (electrons, ions, neutral particles). Since their discovery by Austin and Stark in 1902, they have been widely used in many fields for their specific properties. The first use of SE was in various particle multipliers to enhance weak electron signals. The multi-step production of SE in a usual channeltron or micro channel plate (MCP) can give a signal gain as high as 10^8. This kind of multiplier is used in many detectors found in a wide range of applications from complicated analyzing machines to fancy night vision goggles. Secondary electrons carry electronic structure information from the substrate they emitted, and are a useful signal in analytical instrumentation such as the electron probe microanalyzer (EPMA). The most famous application of secondary electrons is as the imaging signal of the scanning electron microscope (SEM). Nearly all of the over 50,000 SEM operating in research or commercial laboratories apply SE as the primary signal sources for imaging. Further, because secondary electrons are negatively charged particles and can be generated easily from a sample, the emission of SE is manipulated to adjust sample charge balance or surface potential in applications sch as particle accelerators and plasma display panels (PDP). The emission of SE is not always favorable. In irradiation experiments SE emission complicates generally all measurements of ion or electron current. SE emission also leads to fast charge-up of insulating surfaces, which may not be desirable, e.g., on bodies in outer space or in plasma physics experiments.

Our ability to manipulate the SE signal is determined by how well we understand its behaviors and the theories that describe it. The need of this research is much more urgent than it might first appear. Though both experimental and theoretical research have been carried out on SE for over a century, producing many models on its production and stacks of data quantifying its characterization, there are still many ambiguous points. For the

relatively well understood metals, e.g. near free-electron metal Al and noble metals, the spatial distribution of the SE on the sample surface can not be simulated to the precision of nanometer scale, making any claims on the high resolution of a modern SEM unconvincing. For insulators and semi conductors, the SE generation mechanisms remains unclear, and the SE yield of most of these materials can be obtained only by estimation. The semi-conductor industry is struggling today to alleviate charge accumulation when inspecting non-conducting wafers. A huge amount of money is spent each year to solve this problem by improving tool design and optimizing application practice.

In this thesis, the secondary emissions under electron beam bombardment will be mainly discussed. The incident particles will be electrons except where specially pointed out.

1.2 Basic Features of secondary electrons

1.2.1 Energy distribution

When energetic electrons bombard a sample surface, they will penetrate into the sample, experience many elastic and inelastic interactions with the sample atoms and emit a variety of signals. For elastic scattering processes, the incident electrons, the so-called primary electrons (PE), deviate in a large angle from their previous direction with almost no energy transfer to sample atoms. This kind of scattering is the result of the coulombic interaction between negatively charged incident electrons and positively charged atomic cores or negatively charged electrons of the sample. For inelastic scattering the PE will interact with sample atoms and experience a change in both deviation and energy, producing various signals in the following ways:

1. Energetic PE may ionize the atom by removing one inner shell-electron from its orbit, to produce characteristic X-rays or Auger electrons, which in turn may generate fluorescence X-rays and SE ;

2. PE may be decelerated in the coulomb field of the specimen atoms and produce bremsstrahlung or continuous X-rays giving the background of the characteristic X-ray radiation line;

3. For an insulator, the excitation of the electrons in the solids across the band gap can cause cathodoluminescence;

4. The scattered primary electrons with reduced energy together with the excited electrons of the sample may further excite electrons in the conduction band of a metal or outer shell valence electrons in semi conductors and insulators, causing collective oscillations (---- plasmons) or directly produce secondary electrons;

5. Finally but not the least, all of these electrons may interact with the crystal lattice, causing vigorous atom vibration and produce a temperature rise of the sample.

Emitted electrons have all energies up to primary beam energy E_{PE}. A typical spectrum displaying the energy distribution is shown schematically in Figure 1-1(a). The energies of elastically scattered electrons are distributed as a sharp peak around E_{PE}. On the background of inelastically scattered electrons, there are often peaks corresponding to plasmon oscillations, Auger electrons, and the secondary electrons. Under most conditions SE have the highest intensity of all inelastic signals as shown for Si at E_{PE}=1keV (Figure 1-1(b)). The large intensity of SE should allow for microanalysis performed with much higher speed than other weaker signals [1].

Terminology of secondary electron needs to be clarified to avoid confusion in the later part of this thesis. The term "secondary electron" has different meanings in different contexts:

1. In describing the electron-solid interaction process, all those electrons excited from the sample as a result of inelastic scattering are called secondary electrons. Of these SEs, most have energies of several tens eV and are called *slow secondary electrons*, a small amount have high energy up to half of beam energy are called *fast secondary electrons*.

2. In most literature, SEs are differentiated from the backscattered electrons (BSEs) according to their kinetic energies when leaving the sample. Those electrons with

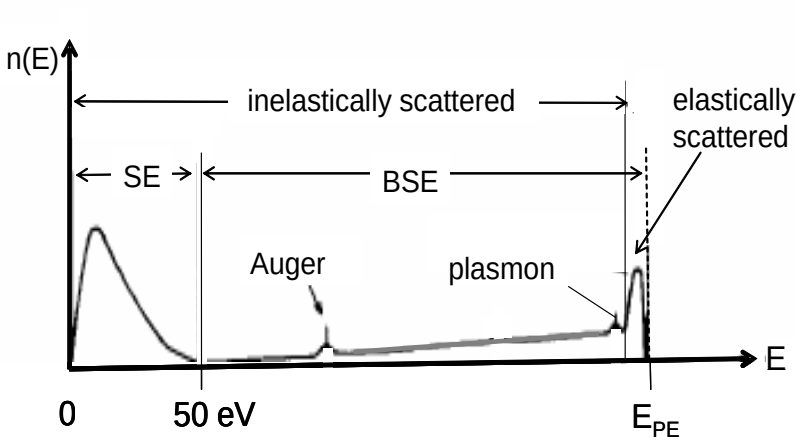

(a)

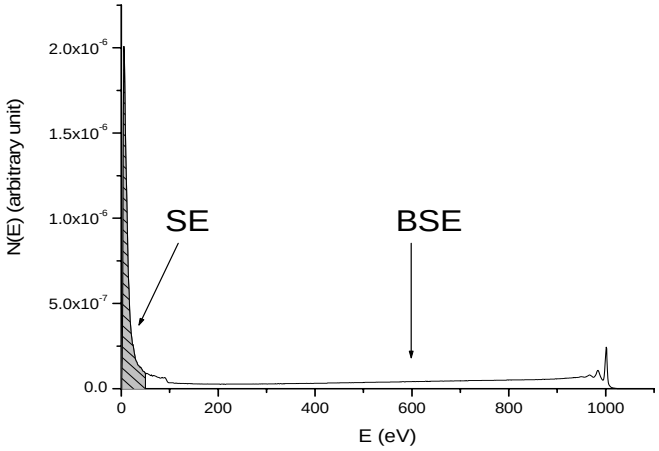

(b)

Figure 1-1: Energy distribution of electrons emitted from a surface as a result of electron bombardment.

(a) Schematic illustration.

(b) The true energy distribution electrons emitted from Si at E_{PE}=1keV. Data in this graph is collected on PHI 680 AES and calibrated by method in chapter 4. The shaded area represents count of SE; white area under curve represents that of BSE.

energies in the range of 0 to 50eV are defined as SE, all other electrons including both elastically scattered and inelastically scattered ones with energies above 50eV and up to E_{PE} are BSE. Since more than 90% of the secondaries are emitted with less than 10eV of energy, it is conservative enough to set 50eV as the upper cutoff for defining secondary electrons. These electrons are usually called true secondary electrons. In some early work, other values such as 30eV or 100eV were used as the cutoff energy.

The energy distribution of SE is nearly independent of the energy of the PE, and is characterized by the most probable energy E_{SE}^{m} and the half width (HW). Typically E_{SE}^{m} is 5eV and 50% of the total SE falls within the range 0-12eV. E_{SE}^{m} and HW both depend on the material. HW is usually smaller for insulators than for metals according to Dietrich and Seiler[2] as in Figure 1-2, but contrary results have also been observed in experiment[1]. Thin surface layers can affect the SE energy distribution. A clean sample produces SE spectrum with higher peak energy and broader peak width[1]. Theoretical prediction of the SE spectrum profile needs complex models and detailed information on the electronic structure of the sample[3]. Chung and Everhart [4] expressed the shape of the energy distribution for free electron metal in the form:

$$\frac{dN}{dE} = k \cdot \frac{E - E_F - \phi}{(E - E_F)^4} \qquad (1\text{-}1)$$

where k is the material constant, E_F is the Fermi energy, and ϕ is the work function. N is the SE count at the emitted energy E measured with respect to the Fermi Level. Experimental spectra from clean sample shows good match with the expression of Chung and Everhart [5]. According to Henke et al [6], for insulators:

$$\frac{dN}{dE} = \frac{E + \chi}{E^3} \qquad (1\text{-}2)$$

where E is taken with respect to the bottom of the conduction band and χ is the electron affinity.

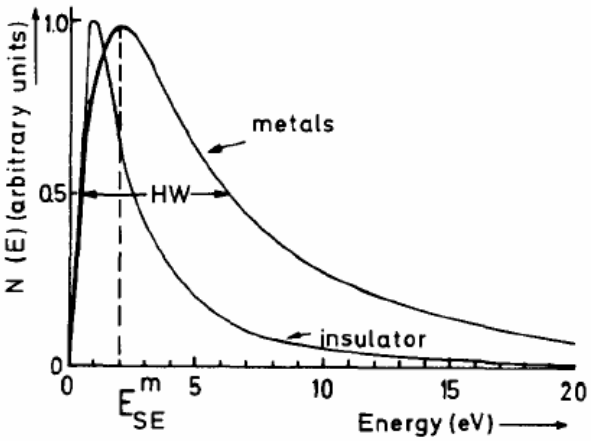

Figure 1-2: schematic energy distribution of SE from metal and insulator surfaces. Image courtesy of Seiler H. [7]

1.2.2 Angular distribution

The angular distribution of SE from polycrystalline surface is a cosine function relative to the local sample and is nearly independent of the angle of incidence of the primary electrons [8-11], see Figure 1-3. This is a result following directly from the isotropic nature of elastic scattering within the specimen[3].

1.2.3 Escape depth

Secondaries are produced anywhere within the interaction volume of the primary electrons with the sample, but because of their low kinetic energies, only those from a shallow layer below the sample surface can escape. SEs produced deeper in the sample suffer more inelastic scatterings and thus more energy loss along their path to the surface, as a result they might not have enough energy to overcome the energy barrier to escape. The escape depth of SE is small compared to other signals resulting from electron-solid interactions (Figure 1-4). According to Seiler [7, 12], the maximum escape depth is $T \approx 5\lambda$, where λ is the mean free path (MFP) of the secondaries; for metals $\lambda \approx 0.5 \sim 1.5nm$, thus $T \approx 5nm$; for insulators $\lambda \approx 10 \sim 20nm$, thus $T \approx 75nm$. These values for T are only rough estimates

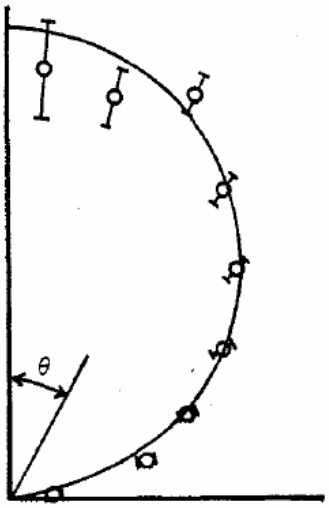

Figure 1-3: Angular distribution of SE follows cosine law.

Image courtesy of Shimizu R. [10]

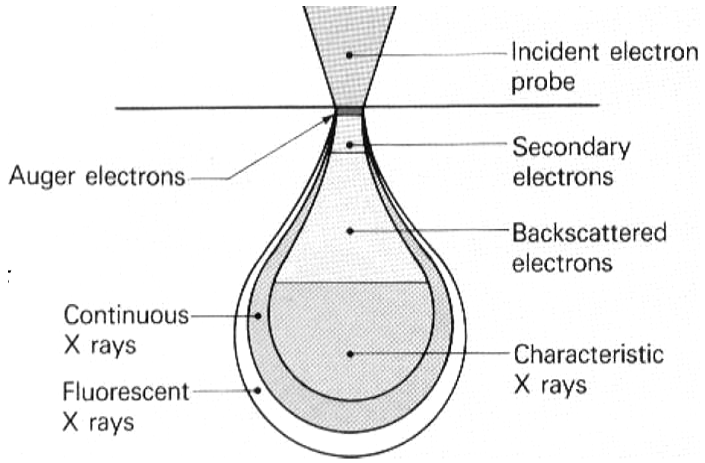

Figure 1-4: Schematic illustration of escape depths for various signals as a result of electron-solid interaction.

since λ varies with material and the energy of the secondaries. The substantially large SE MFP is assumed to be a direct consequence of the fact that inelastic scattering of secondary electrons takes place chiefly with conduction electrons, which are abundant in metals but greatly reduced in insulators. [13]

Though SEs escape only from the surface layer, it is not correct to assert that SEs provide information of only the surface. Emitted SEs are composed of two parts, SE_I and SE_{II}. SE_I are produced by the incident beam electrons as they penetrate through the escape zone and SE_{II} are generated in the same zone by the backscattered electrons leaving sample, see Figure 1-5. While these two distinct SEs are generated by different electrons, they are identical in nature. There is no way to differentiate between them experimentally. Since SE_{II} are consequence of BSE, they carry information from deep within sample. For imaging buried sample features, SE_{II} generated from high primary beam energies are preferred.

1.2.4 Spatial distribution

SE_I and SE_{II} have different spatial distributions and therefore different functions for imaging. SE_I are localized on the area illuminated by the incident beam and thus are capable of high resolution. The full width of half maximum (FWHM) of SE_I is

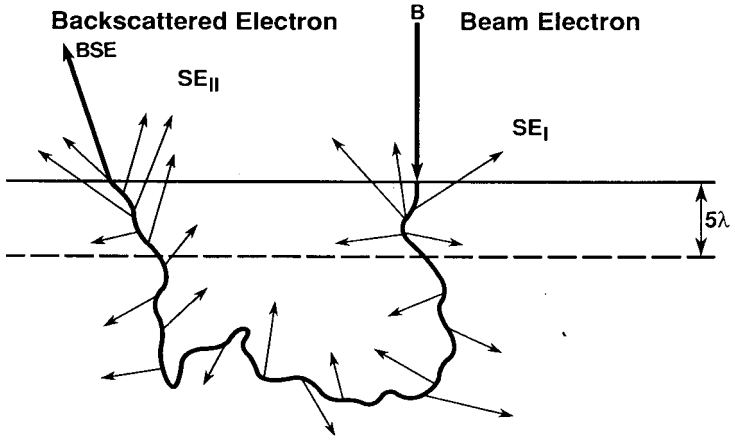

Figure 1-5: Schematic illustration of the origin of two sources of secondary electrons in the sample: SEI generated by the incident electron beam and SEII generated by the BSE leaving the sample. SE escapes from within only 5λ below the sample surface.

Image courtesy of Goldstein J. et.al. [13]

determined by the mean free path λ of the SE and is on the order of a nanometer [14-16]. SE_{II} emerge over a much wider area, approximating the size of the BSE distribution and thus are low resolution signal. According to Hasselbach and Rieke [17] the spatial distribution of SE_{II} can be approximated by a Gaussian distribution.

The distributions of SE_I and SE_{II} vary differently with beam energy. Since SE_I are characterized by λ, they will not change with beam energy. The widths of SE_{II}, however, vary strongly with beam energy from several um for $E_{PE} = 30keV$ to several nm for $E_{PE} = 1keV$. The spatial distributions of combined SE are shown in Figure 1-6: under high beam voltages, SE_{II} are the dominant signal forming a long tail that almost immerses SE_I; under low beam voltages, the distribution of SE_{II} shrinks into the size close to that of SE_I, SE_{II} make contributions to high resolution signals in this case. SE_I thus determines the ultimate resolution of SEM [18]. In any effort to obtain high resolution, SE_I is the part that should be strengthened and SE_{II} should be suppressed. Because of the narrow SE distribution as well as other advantages[19], low voltage SEM (LVSEM) working under $E_{PE} \leq 5keV$ is currently popular for wafer inspection. For a high beam energy and high magnification (>100,000X) the size of the SE_{II} distribution is comparable to the field of view (<1 um). Since the magnitude of the SE_{II} signal is constant over the whole scanned area; only the SE_I part contributes to contrast in the image. [13]

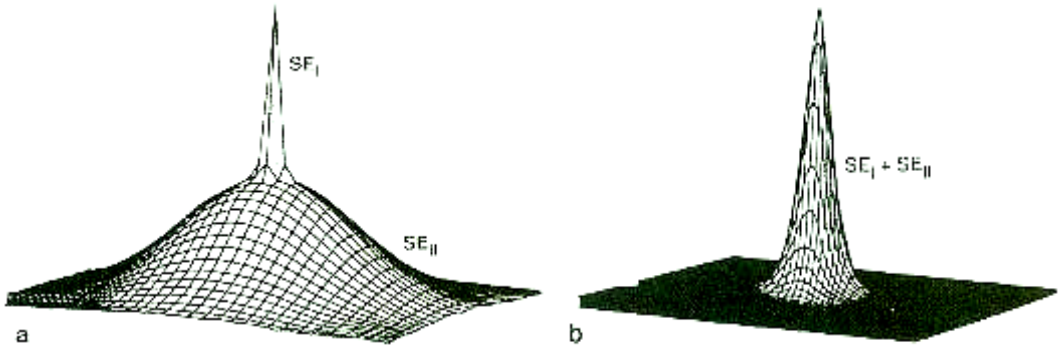

Figure 1-6: Schematic spatial distribution of SE on sample surface.
Image courtesy of Joy D.C. [20]
(a) Under high beam energy. (b) Under low beam energy

1.2.5 SE yield

SE yield δ is the ratio of the number of SE to PE and is an important parameter to quantify the SE emission. The yield δ is composed of the two parts from SE_I and SE_{II}:

$$\delta = \delta_{PE} + \eta\delta_{BSE} = \delta_{PE}(1 + \beta\eta) \quad (1\text{-}3)$$

$$\beta = \delta_{BSE} / \delta_{PE} \quad (1\text{-}4)$$

where δ_{PE} is the number of SE released per PE, δ_{BSE} is the number of SE released per BSE, and β represents the relative efficiency of the backscattered electrons in generating secondaries. Because the backscattered electrons are lower in energy than the primary electrons, and since they approach the surface over a range of angles that are more favorable for producing SE, β is always greater than 1. Both simulation and experiment demonstrate that β has typical values of 3~6, and varies with atomic number and beam energy [3, 12, 21, 22]. In a typical metal or semiconductor for which $\eta \approx 0.3$, less than 50% of the total SE signal is produced by the incident electrons.

The SE yield δ as a function of beam energy E_{PE} has a general profile as shown in Figure 1-7 for all materials: the yield rises from zero at the lowest energies, reaches a

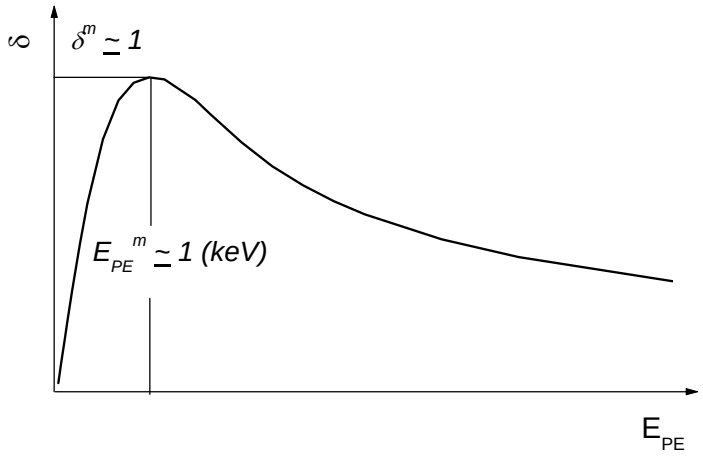

Figure 1-7: Schematic profile of SE yields δ as a function of primary energy E_{PE}. The values for δ^m and E_{PE}^m in the figure are typical for metals.

maximum δ^m at some energy E_{PE}^m and then falls monotonically as about $1/E_{PE}$ at higher energies [7, 23]. At low E_{PE}, the inelastic cross section is not big enough to produce much SE; at high E_{PE}, most of the SE produced are too deep to escape, the SE yield is small again; at intermediate E_{PE}, most of the internal SEs are in the 5λ depth and can contribute to δ, giving a maximum value δ^m. For most metals $\delta^m \approx 1$, $E_{PE}^m \approx 1$ keV. Insulators have much higher SE yields. MgO is the most famous oxide with $\delta^m \approx 20$ and is widely used as surface protective material in plasma display panels[24].

The SE yield varies with beam incidence angle θ following the relationship of [25]:

$$\delta(\theta) = \delta_0 \sec(\theta) \qquad (1\text{-}5)$$

where δ_0 is the SE yield at normal incidence. For most conditions when the primary beam penetrates deeper than the SE escape depth, the path length of the PE in this zone is enhanced by a factor of $\sec(\theta)$ and causes the same fractional enhancement of SE yield. The factor $\sec(\theta)$ applies only for SE_I part of the secondaries. But since BSE yield also increases with sample tilt angle[13], the total SE yield increases as the sample is tilted. Under low E_{PE} when beam penetration is limited within the 5λ depth, all internal SE generated can escape; tilt has no effect on the value of δ. The effect of sample tilt on δ is illustrated in Figure 1-8.

Unlike BSE, for which variation of η increases monotonically with the atomic number Z [26], the SE yield δ as a function of Z is not as well understood. This topic will be discussed in detail in chapter 3.

1.3 Applications of SE in SEM

Though the idea for the SEM was initiated by M. Knoll in 1935, and by M. von Ardenne for the transmission mode (STEM) in 1938, the first commercial scanning electron microscopes did not appear until the work of C. W. Oatley and his coworkers at

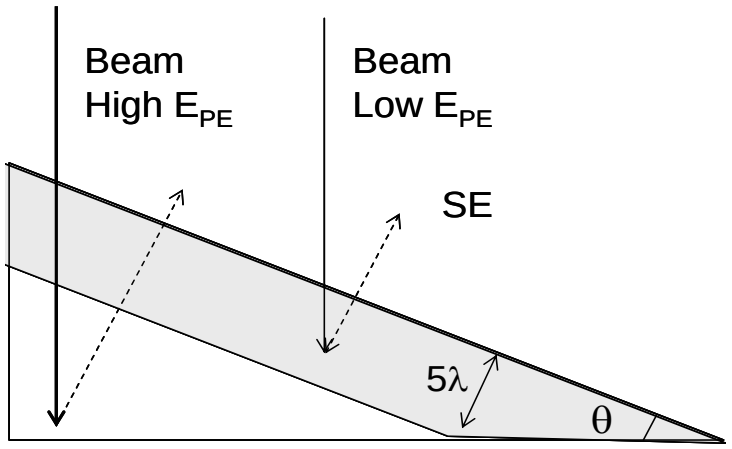

Figure 1-8: Schematic illustration of the effect of specimen tilt angle θ on the SE yield. Under high E_{PE} primary electrons have longer path in the escape zone 5λ; SE yield δ is enhanced over normal incidence. Under low E_{PE}, the whole path of PE is in 5λ; δ is not a function of θ.

Cambridge University started in 1965. Since that time SEM has grown to an established technique for surface imaging. The main advantages of this technique are a resolution of 1-10nm, a large depth of focus, and the numerous types of signals that can be used in both imaging and analyzing modes. The range of applications covers materials science, biology and medicine, industrial research, and semiconductor inspection, including electron-beam lithography and metrology.

Schematic structure of a SEM is shown in Figure 1-9: an energetic electron beam is focused and guided to the specimen by the optical system which includes the illuminating and final lenses. The beam raster scans on the specimen under the control of the scan coil and interacts with the sample. The emitted electron signals are detected and reconstructed into a virtual image on a TV screen that is synchronically scanned, with pixel grayscale signals intensities at the sites of beam impingement. According to the energies of the electrons that are detected, the SEM images can be categorized as SE images and BSE images. SE is the most popular image mode owing to its capability for high contrast [7].

Low energy SE can be deflected and accelerated towards a detector with weak electric fields without disturbing the energetic primary beam. These low energy secondary electrons contribute most to the SE image. In most common SEMs, secondary

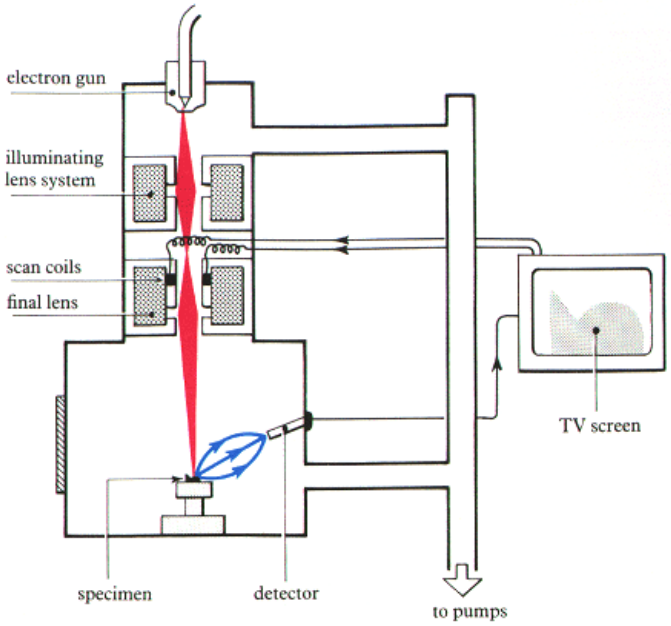

Figure 1-9: Schematic structure of a scanning electron microscope with secondary electrons forming the images on the TV screen.

Image courtesy of: http://acept.asu.edu/PiN/rdg/elmicr/elmicr.shtml, Aug 31, 2006

electrons are collected by an Everhart-Thornley (E-T) detector mounted on the side wall of the specimen chamber above the specimen with a positive bias voltage of several hundred electron volts. The trajectories of the SE in all directions are bent toward the detector under the effect of this bias voltage, providing collection efficiency of almost 100% for a smooth surface [13]. It is this high collection efficiency together with the already intense SE signal and the multiplication of the E-T detector that make the integration of SE images at television scan rates possible.

1.3.1 Topography contrast

Topography contrast is the most striking feature of SE images. The surface topography has strong 3-D features that closely resemble the sample, as if the sample was illuminated by a strong light beam from the detector and viewed from a point off to one side. A SE image is extremely powerful for failure analysis in material analysis. Ductility properties and source point of a fracture surface are apparent at first glance, as shown in Figure 1-10.

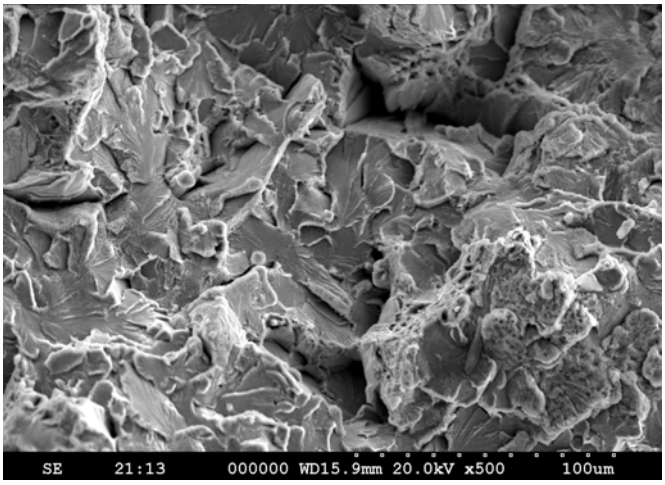

Figure 1-10: SE image of a fracture under punch for a Fe rod shows strong 3-dimensional feature. The comb-like area is caused by ductile fracture. The tongue-like areas is caused by brittle fracture, round particles in the dimples are the origin of this kind of fracture. Image taken on Hitachi S-4300SEM under beam voltage of 20keV with magnification of 500.

The topography contrast is a combined effect of non-uniform SE emission yield and collection efficiency of the detector. On the edges and micro inclined facets of a rough surface, the SE yield δ is higher than that from regions normal to the beam incidence. This enhancement of SE yield ceases under low beam energies, as analyzed in section 1.2.5. Sample tilt can increase the topography contrast caused by angular variations [7]. Two types of SE detector: the lateral Everhart-Thornley detector and the in-lens detector located in or above the objective lens and collecting SE by a strong extraction field react differently to the SE angular distribution. The E-T detector located on a side wall of the chamber has lower collection efficiency for facets facing away the detector as compared to those facing the detector. This collection efficiency difference produces a shadowing effect. Dark areas on SE images typically correspond to notches on the sample (Figure 1-10) and Figure 1-11(a)), because the electric field produced by the biased detector is not strong enough to collect SE produced in the deep valleys. SE images formed with E-T detector thus have strong shadowing effects. The in-lens detector has more uniform collection efficiency with respect to the angular distribution of SE. Therefore, details in deep valleys can be viewed with very high brightness (Figure 1-11 (b)). In most cases, features are sharper when viewed with in-lens detectors, while stronger shadowing and 3-D effect are examined with lateral Everhart-Thornley detectors.

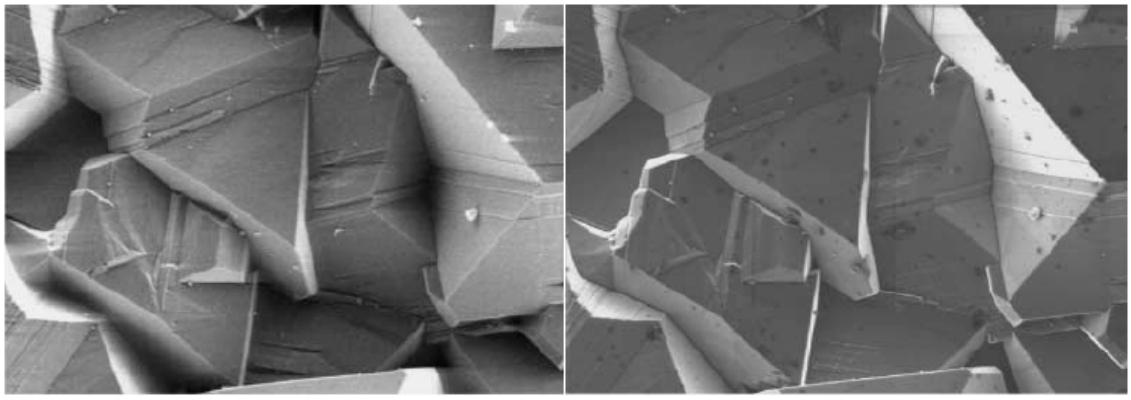

(a) **(b)**

Figure 1-11: Micro-structures diamond specimen with graphitized residues obtained using a SE (LEO, Gemini DSM 982) with working distance 2mm, beam energy 5keV with different detector.

Image courtesy of Cazaux J. [27]

(a) Lateral E-T detector: image has strong shadowing and 3-D effect.

(b) In-lens detector: image has sharper features.

1.3.2 Charging controls for insulator

SE imaging of poor conductors or insulators is difficult because of a charging effect. Charging occurs when the emitted electron current is larger or smaller than the incident. The extra charges can not flow to the ground as with a conducting sample, and they assemble in local subsurface area and produce a strong field as high as 10^7V/cm. This strong local field may interfere with the collection of secondary electrons, deflect the incident beam, or can even damage the specimen. In serious charging conditions, SE images are featureless with bright or dark areas fluctuating with time. Control or elimination of charging is an important aspect of effectively using an SEM.

According to charge conservation,

$$I_b = I_{sc} + I_b \cdot \delta + I_b \cdot \eta \qquad (1\text{-}6)$$

where I_b is the incident beam current; I_{sc} is specimen current (the extra charges accumulated inside the sample in unit time); and δ and η are the SE yield and BSE yield respectively. Incident charges are balanced by the emitted part $I(\delta + \eta)$ and the

residual I_{sc}. There are two ways to stabilize surface potential in insulators: either to connect the current (I_{sc}) to ground by coating the sample with a thin film of conductor or to choose conditions such that the total yield σ satisfies:

$$\sigma = \delta + \eta = 1 \qquad (1\text{-}7)$$

Because BSE yield is almost a constant function of E_{PE} comparing to SE, the total yield σ varies with beam energy in a manner similar to that of SE yield δ. σ normally has a peak value greater than one, and therefore it crosses 1 at two energies E_1 and E_2, as shown in Figure 1-12.

A steady normal SE image can be obtained on insulators at E_1 and E_2. When $E_1 < E_{PE} < E_2$, $\sigma > 1$, and the sample will be positively charged, therefore SE are attracted back to the sample surface, cause SE images to appear dark, especially at high magnifications. Conversely, when $E_{PE} > E_2$ or $E_{PE} < E_1$, $\sigma < 1$, and the sample will be negatively charged, therefore SE are repelled from the sample surface, causing the SE images to appear bright. In extreme cases when $E_{PE} >> E_2$, the negative potential of the surface can reach very high values up to the potential of the electron gun. Working near E_2 is the most stable condition, because beam energies can make self-adjustment when it is off this point by acceleration of the positive potential or deceleration of the

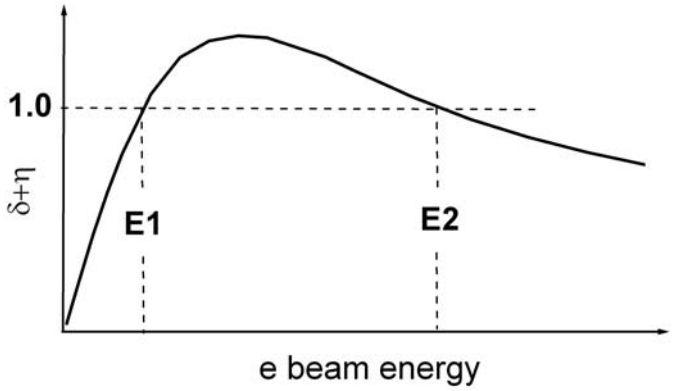

Figure 1-12: Schematic variation of total yield σ=δ+η with beam energy.

negative potential of slightly charged samples. E_2 ranges from 0.5 keV to 3 keV for most insulators [19]. Tilting the sample increase δ and thus E_2, allowing stable SEM performance on higher beam energies.

1.3.3 VPSEM

Unlike the traditional SEM, which is performed in a vacuum with pressures below 10^{-2} Pascal, the variable pressure SEM (VP-SEM) allows observations to be carried out in the presence of gases at pressure up to about 1000 Pascal in the specimen chamber. This arrangement makes it possible to image many kinds of samples that would be unsuitable for a conventional SEM due to dirt or moisture. In addition, poorly conducting or insulating sample can be imaged in a VP-SEM at high beam energies (typically 10-30 keV) without the need for a conductive coating. The fact that the VP-SEM instrument now accounts for over 50% of the market for conventional (i.e., non-field emission) scanning microscopes proves the appeal of this concept [28].

The conventional Everhart-Thornley can not be used in a VP-SEM because the MFP of the secondaries in the gas in too short to permit them to reach the detector. Signals are normally detected in three modes [29]: BSE modes using the conventional BSE detector and two other SE modes that detect the specimen current (environmental SE detector or ESED) or detect the avalanched SEs (gaseous SE detector or GSED). In both of the SE modes, electrons are attracted to a positively charged electrode above the sample, causing ionization of the gas particles. Continuous acceleration of the electrons and ionization of the gas result in a cascade production of electrons and positive ions. This increase in the amount of electrons effectively amplifies the original secondary electron signal. The positively charged gas ions are attracted to the negatively biased specimen and offset any charging that takes effect. Set-up of the ESED and GSED modes are schematically shown in Figure 1-13 [30].

Images produced by ESED can virtually eliminate the effects of specimen charging while retaining most of the characteristics of normal SE images. BSE images can be taken under high pressure SEM using the normal BSE detector without necessarily

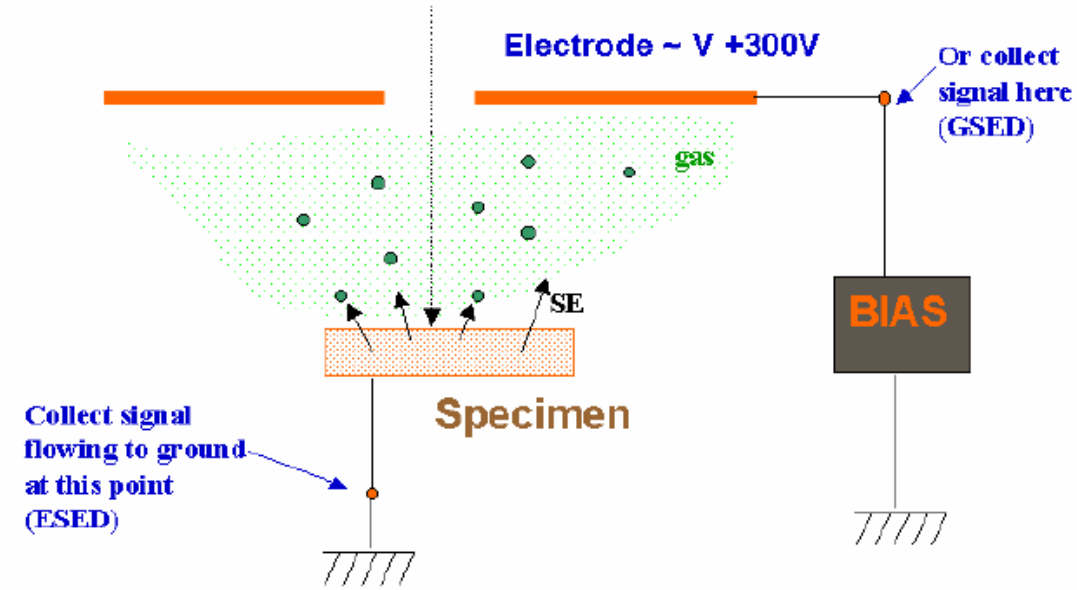

Figure 1-13: Schematic diagram of signal detection for SE imaging on VPSEM. Image courtesy of Joy D.C. [30].

deteriorating the resolution. A set of images under various conditions are compared in Figure 1-14.

1.4 Scope of thesis

In the following chapters, a review of the theories of SE generation will be given (Chapter 2). To better understand SE emission and to provide better reference values, optimization of the scattered SE yield database was done by using a Monte Carlo simulation and was tested using a semi empirical law (Chapter 3). A shell filling effect was found for some parameters describing SE emission as a result of the database optimization. To test this result and to gain further understanding of SE generation in binary compounds, and to avoid systematic errors encountered in more traditional approaches, a new measurement on the SE yield was developed and performed. This innovative SE yield measurement was made using a PHI 680 SAN. Before performing the measurement, absolute intensity calibration and performance optimization were carried (Chapter 4). In the last chapter (Chapter 5), the experimental set-up is described and results are discussed.

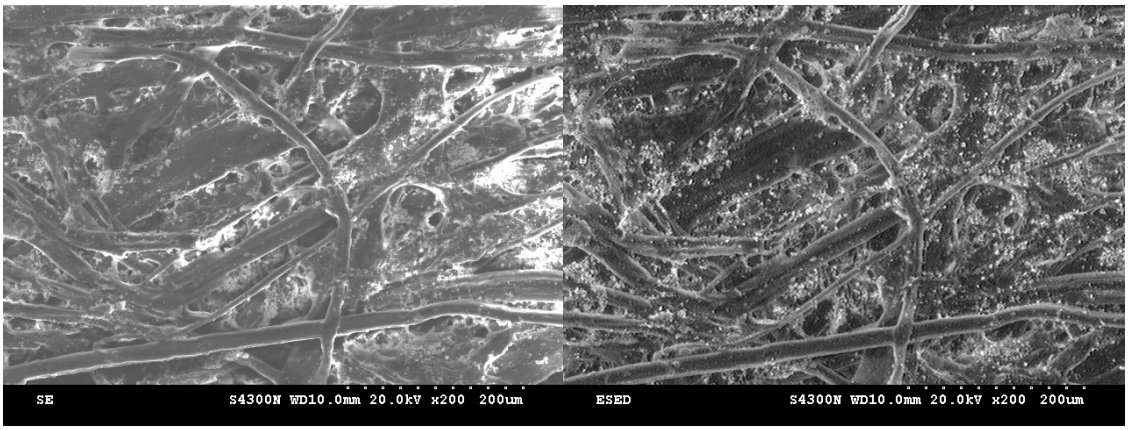

(a) **(b)**

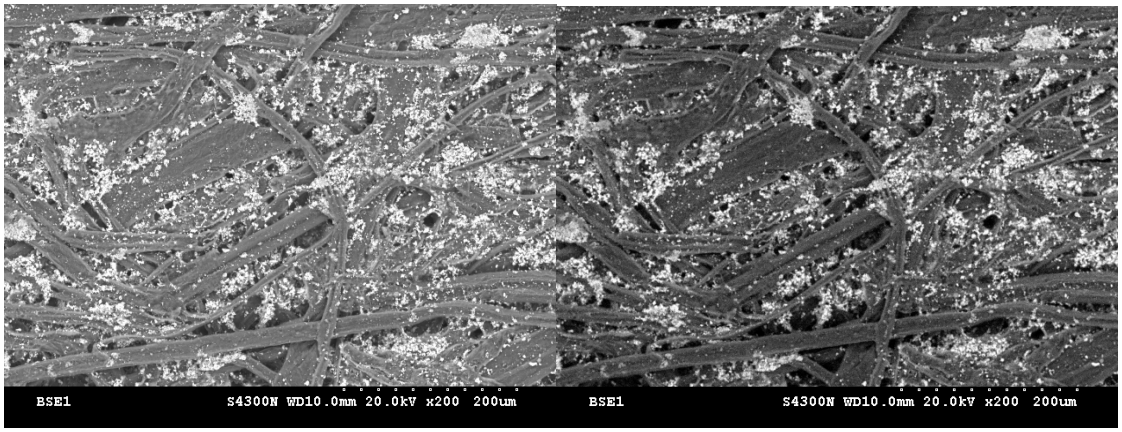

(c) **(d)**

Figure 1-14: Comparison of the SE and BSE images of a piece of paper taken in SEM working in conventional high vacuum (10^{-3} Pascal) mode and high pressure mode with air in the specimen chamber. Images are taken on Hitachi S4300 SE/N with working distance of 10mm and beam energy of 20 keV.

(a) SE image detected by Everhart-Thornley detector on high vacuum mode. Charging is apparent.

(b) SE image detected by ESED with air pressure of 200 Pascal. Charging is greatly reduced. 3-D topography features are more pronounced than the BSE images as (c) and (d)

(c) BSE image detected under high vacuum.

(d) BSE image detected with air pressure of 100 Pascal.

2. Chapter Ⅱ: Basic mechanisms and models of secondary electron emission

2.1 Introduction

Since their discovery in 1902, secondary electrons (secondaries or SE) have been the object of theoretical and experimental analysis. Historically the models describing the emission of secondaries can be classified into three categories: semi-empirical, transport theories on the SE cascade process, and Monte Carlo simulations.

The semi-empirical models use macroscopic properties as input quantities and omit the detailed history of secondary generation. It was first rigorously presented by Bethe [31] and Salow [32]. Following their studies, Baroody [33], Jonker [34], Bruining [35], and Dekker [23] developed detailed phenomenological models on SE emission, of which the most famous is the universal law describing SE yield as a function of primary energy. These models made some simplifications on the SE generation process, and still had good agreement with experiments.

A major step toward a comprehensive theory on SE generation was taken by Wolff [36], who developed a transport treatment for electron-induced secondary electron emission to obtain the spectrum of emitted secondaries, as well as estimating the maximum yield. Later, many authors such as Cailler and Ganachaud [37], Schou [38, 39] and Devooght et al. [40] used the Boltzmann transport equation to describe the cascade of SE during transportation to the sample surface.

The Monte Carlo method is a statistical sampling technique using random numbers to solve determinable problems. Since its first application in 1940 and with the development of high-speed computers, it has become a standard technique in such areas as particle transport, statistical physics, etc., and is widely used to simulate the trajectory of scattered electrons. Various Monte Carlo models using different approximations for the microscopic scattering cross sections of electrons in the target have explained and confirmed many proprieties of secondary electron emission.

This chapter will start from a brief description on the terminologies that are usually used to describe electron-solid interactions and the method of Monte Carlo simulation, and then focus on the topic of secondary emission. First, the mechanisms of the generation, transportation and escape of SE are described, and then the semi-empirical models and several approaches to Monte Carlo simulation models are introduced. The approach to SE emission by solving the Boltzmann transportation equation is not applied in this thesis, and thus is not described here. The principles of SE generation by cascading will be briefly introduced in section 2.3.2 as well as SE transportation as one of the mechanisms of SE emission.

2.2 Electron-solid interactions

Electrons moving within the specimen will be scattered by electrons and/or nuclei of the material. Borrowing the definitions from classical particle collisions, scattering of electrons is also categorized into two types: elastic and inelastic scattering. Elastic scattering is the net change in direction that the incident electrons or internal secondaries undergo as a result of the coulombic attraction between the negatively charged electrons and the positively charged atomic nuclei, as well as the corresponding repulsion between the orbiting electrons and the incident or secondary electrons. The deviation of the trajectory from its original direction can vary from 0-180^{o}, with little or no change in energy. For inelastic scattering, electrons can transfer a part or all of their energies to the sample atoms with direction deviations of only 0.1^{o} or less. The probability for these two types of scattering can be described by two parameters: the scattering cross section σ and the mean free path λ.Stopping power is a parameter to evaluate the average rate of energy dissipation during inelastic scattering using a continuous slowing down approximation. As the energy dissipates electrons will ultimately thermalize inside the specimen or escape. The space where these scattering and trajectory events happen inside the specimen is called the interaction volume. Beam range scales the size of the interaction volume and is an important parameter for electron-solid interactions.

2.2.1 Scattering cross section

The scattering cross section σ is defined as:

$$\sigma = N/n_i n_t \qquad (2\text{-}1)$$

where N is the number of scattering events per unit volume, n_i is the number of incident particles per unit area, and n_t is the number of target sites per unit volume. σ thus has unit of $events \cdot area/e^- /atom$, which is actually $area$ since the number of events, electrons and atoms are unitless, and is the reason why this term is called the cross section. The differentiations $d\sigma/dE$ and $d\sigma/d\Omega$ are also frequently used to describe the preference of a scattering event to a specific solid angle Ω or electron energy E.

2.2.1.1 Elastic scattering

A Rutherford-like formula is one of the most popular expressions for the elastic scattering cross section. In this model electrons are considered as classical particles scattered by the nuclei. Considering on the screening effect of the outer-shell electrons, the total cross section σ_E is [41]:

$$\sigma_E = 5.21\times10^{-21}\frac{Z^2}{E^2}\frac{4\pi}{\alpha(1+\alpha)}\left(\frac{E+511}{E+1024}\right)^2 \qquad (2\text{-}2)$$

where E is the electron energy in kilo-electron volts (keV), Z is the atomic number of the target, and α is the screening factor that takes into account the fact that the incident electron does not see all of the charge on the nucleus because of the orbiting electron cloud. α is usually evaluated using an analytical approximation, Bishop [42] gave it as:

$$\alpha = 3.4\times10^{-3}\frac{Z^{0.67}}{E} \qquad (2\text{-}3)$$

As incident electron energy decreases and the atomic number of the sample increases, the wave mechanical effect of the incident electron becomes stronger. The Mott scattering model, first proposed by Mott in 1929 [43] and then developed by Reimer and Krefting [44], calculates the scattering cross section by the partial wave method and well describes the elastic scattering process in this case. A systematic investigation of the Mott scattering model can be found in [45]. Though the Mott cross section is expected to be

more accurate at low energies and for high atomic number materials, the screened Rutherford model is also widely used for its simplicity and is of great value when simulating trajectory of electrons of energies of kilo-electron volts.

2.2.1.2 Inelastic scattering

Inelastic scattering includes phonon excitation, SE excitation, bremsstrahlung or continuum X-ray generation and ionization of inner electron shells. A scattering cross section exists for each process and is specific for each material. The detailed expressions for these cross sections are complicated and sometime impossible because of the unavailability of the exact electronic structure of sample atoms.

2.2.2 Mean free path

Mean free path (MFP) λ is the average distance the electron travels in the specimen between certain scattering events. The mean free path can be calculated from the total cross section by the equation

$$\lambda = \frac{A}{N_a \rho \sigma} \qquad (2\text{-}4)$$

where N_a is the Avogadro's number, ρ is the density of the target, and A is the atomic weight. Units of the mean free path are expressed in length. To determine the mean free path λ_j for a particular type of event j, the specific cross section σ_j for that type of event is substituted into equation (2.4). The smaller the cross section, the longer the MFP, and the less likely this event will occur.

2.2.2.1 Elastic scattering

Elastic MFP λ_{el} is typically of the order of a few hundred angstroms at 100 keV and an order of magnitude less at 10 eV. Materials with higher atomic numbers cause more elastic scattering than elements of lower atomic number and thus have a shorter mean free path. This trend is illustrated in Figure 2-1 for a range of energy greater than 500eV. For most materials, elastic mean free paths have minimum values when the electron has an energy value of several tens of eV, with values increasing monotonically as the energy

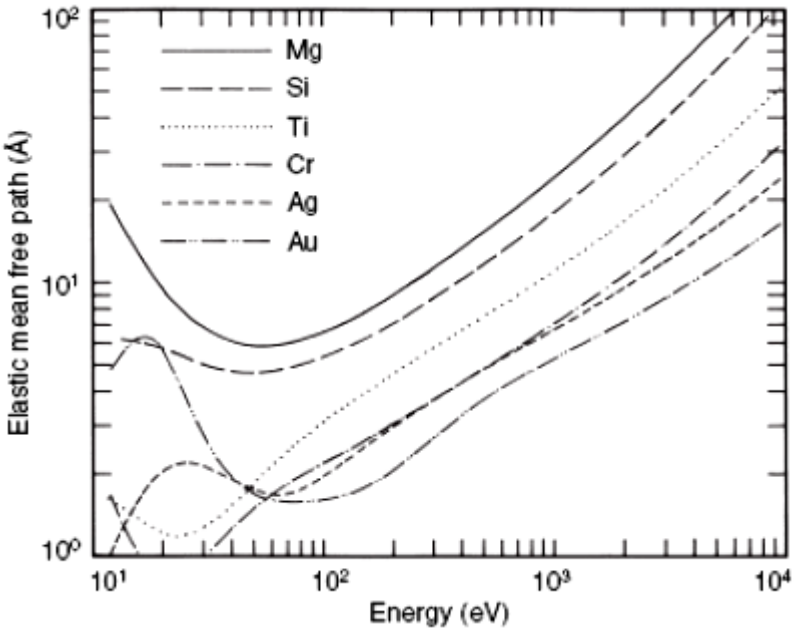

Figure 2-1: The energy dependence of elastic mean free path for several metals. Calculations are based on the Mott's scattering model.

Figure source: Ding and Shimizu [46].

increases on the high energy end. When electron energy is several tens of eV, the trends for elastic MFP are complicated.

2.2.2.2 Inelastic scattering

The common expression for inelastic mean free path λ_{in} is the combination of MFP for each individual event involved in inelastic scattering, e.g. ionization, plasmon excitation or conduction electron excitation:

$$\frac{1}{\lambda_{in}} = \frac{1}{\lambda_{plasmon}} + \frac{1}{\lambda_{core}} + \frac{1}{\lambda_{conduction}} + \ldots \qquad (2\text{-}5)$$

A typical profile of inelastic MFP for silver is shown in Figure 2-2. Values for the mean free path range from several angstroms to several tens of nanometers or more and vary with electron energies. In Figure 2-2 the minimum value at about 100 eV corresponds to a strong excitation of plasmons in Ag at these energies. At higher energies, electrons tend to ionize inner shell electrons, which are the least probable electron to be excited, and the inelastic mean free path increases. At lower energies, there is no mechanism to cause

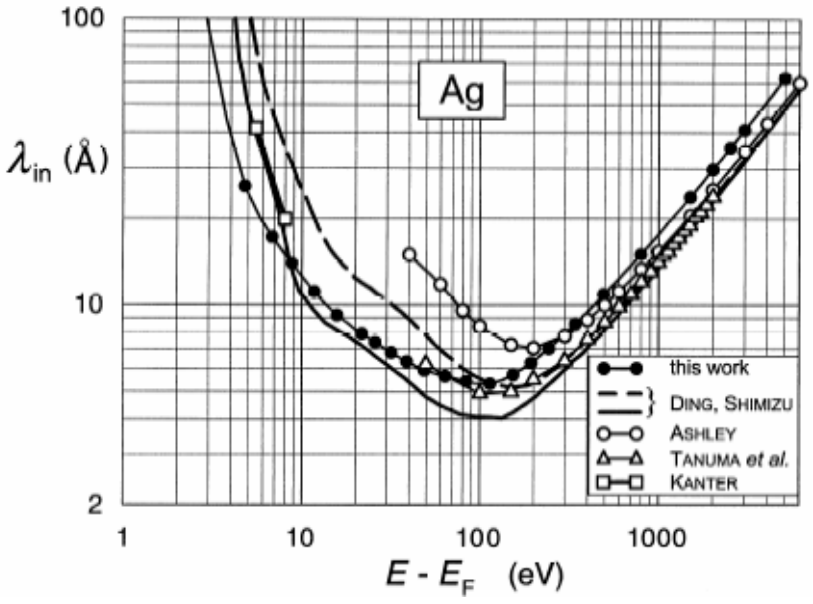

Figure 2-2: Inelastic mean free path vs. electron energy in Ag; the data resources are: Kuhr and Fitting (this work) [47], Ding and Shimizu[48, 49], Ashley, Tanuma et al[50], and Kanter[25].

Figure courtesy of Kuhr J. and Fitting H. [47]

inelastic electron scattering and inelastic mean free paths increase dramatically. Elastic scattering is the dominant scattering in this energy range.

To describe this general form of the inelastic mean free path varying with electron energy, Seah and Dench [51] produced a predictive formula for metals:

$$\lambda(E) = a\left\{\frac{538}{(E-E_F)^2} + 0.41\left[a(E-E_F)\right]^{1/2}\right\} \text{ nm} \qquad (2\text{-}6)$$

where E_F is the Fermi energy and a is the thickness of a monolayer for the target. E and E_F are in eV and a is in nanometers. A formula of similar form for general materials is not available. A database provided by the National Institute of Standards and Technology (NIST) collected information of IMFP from several different sources, including the predictive formula above, and can be of a valuable reference.

2.2.3 Stopping power and energy dissipation rate

In most cases the interactions between electrons and solids are studied on bulk materials, therefore consideration on the average effect of the electrostatic drag exerted by the positively charged nuclei and the energy dissipation happened during the inelastic

scatterings for energy loss of the incident electrons is enough. In stead of a complete approach to incorporate these energy losses individually, an assumption can be made that the incident electrons are slowing down continuously as they travel. This method of treating energy dissipation is called the "continuous slowing approximation". Energy dissipation rate, dE/ds, where s represents the distance traveled in the specimen and E is the energy of the external electron that is interacting with the specimen, is such a parameter to quantify the rate of energy loss. Stopping power dE/dS where S is the production of ρ the density of the target and the distance traveled along the trajectory s, was first used to evaluate energy loss rate of X-ray photons interacting with material. It is apparent that the stopping power had an extra term of mass density comparing to the energy loss rate and has the relationship of:

$$\frac{dE}{dS} = -\frac{1}{\rho}\frac{dE}{ds} \qquad (2\text{-}7)$$

Since both parameters evaluate power of a material to stop the energy of incident particles, energy dissipation rate dE/ds is sometimes referred as stopping power in some literatures. Figure 2-3 illustrates that the energy dissipation rate is a combined effect of individual energy loss events.

The rate at which energy is lost by the incident electron was shown by Bethe in a classic paper [52] to be expressible in the form of equation 2-8, and is characterized by the atomic number Z, and atomic weight A, and the mean ionization potential J of the target material.

$$\frac{dE}{dS} = -78{,}500 \times \frac{Z}{AE} \times \ln\left(\frac{1.166E}{J}\right) \qquad (2\text{-}8)$$

In equation 2-8, E is in kilo-electron volts, S is in g/cm^2, and J in units of kilo-electron volts represents the effective average energy loss per interaction between the incident electron and the solid. This single parameter incorporated into its value all possible mechanisms for energy loss that the electron can encounter, thus allowing the Bethe equation to provide a convenient and compact way of accounting for the variety of energy losses experiences.

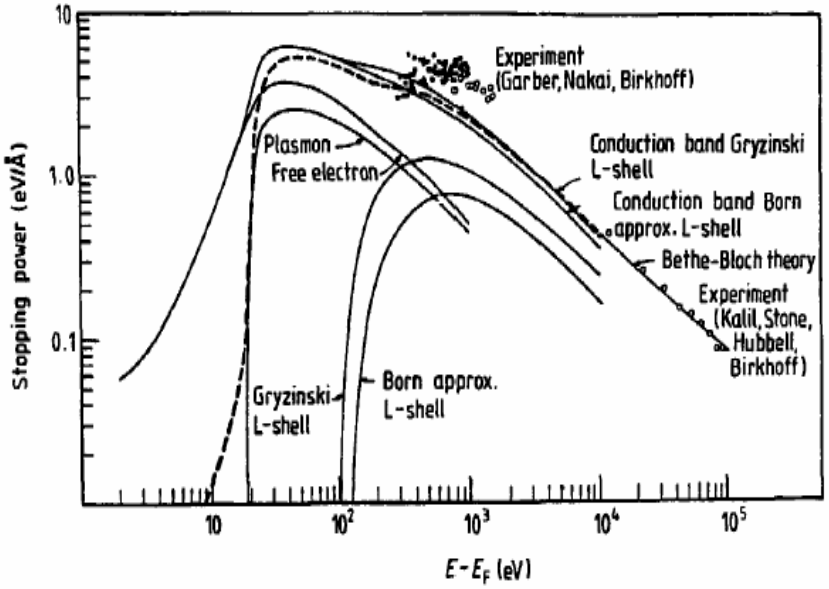

Figure 2-3: Contributions of individual excitation mechanisms to the total stopping power for Al. The Bethe stopping power is also shown in the high energy region to compare with experimental data [53, 54]. The solid lines are calculated by Richie et al [53]. The broken line is calculated from the dielectric function [54].

Figure source: Shimizu and Ding [55]

It was found during experimental measuring the value of mean ionization potential J, of the order of 0.3~0.6 keV, is almost monotonically linearly increases with atomic number of the element. Berger and Seltzer [56] showed that this variation could be fitted with good accuracy by the relation as is shown in equation 2-9:

$$J = 9.76Z + 58.8Z^{-0.19} \text{ (eV)} \qquad (2\text{-}9)$$

Because of its simplicity, Bethe's model has been used extensively for empirical investigation. It is an excellent approximation for high energies such as $E \geq J$, but it is not physically reasonable at low energies, because dE/dS will be a positive value when $E \leq J$. In fact, since stopping power is the total effect of the individual inelastic scattering process, it can be expressed as the summation of their respective stopping powers as long as our knowledge of the material is enough to deduce the individual cross sections for each inelastic event. Aluminum is a simple and near free electron metal and serves as a standard material for a lot of theoretical and experimental studies. Figure 2-3

shows the composition of stopping power for Al and how actual stopping power (the line on the top that covered all other lines) is extended down to several eV. It is obvious that stopping power should have the opposite trend with electron energy as compared to inelastic mean free path. As confirmed by Fitting [57] the summation of the individual stopping power is in very good agreement with experiment in low-energy ranges down to 0.8 keV.

Because the inelastic scattering data for most materials is not available, some empirical extrapolation has been done by Rao-Sahib and Wittry [58] to fill in the trend for the continuous approximation curve at the low energy end. Joy and Luo [59] developed a formula in the form of equation 2-10 that can produce good results for SE yields.

$$\frac{dE}{dS} = -78{,}500 \times \frac{Z}{AE} \times \ln\left(\frac{1.166(E + 0.85J)}{J}\right) \qquad (2\text{-}10)$$

Another way to theoretically deduce the stopping power in a wider energy range is base on the dielectric function of the material. The theoretical formulation for inelastic scattering of a penetrating electron in solid can be well established in terms of the dielectric function $\varepsilon(q,\omega)$. This formulation provides the differential cross-section for inelastic scattering as:

$$\frac{d^2\lambda_{in}^{-1}}{d(\Delta E)dq} = \frac{1}{\pi a_0 E}\,\mathrm{Im}\left(\frac{-1}{\varepsilon(q,\omega)}\right)\frac{1}{q} \qquad (2\text{-}11)$$

where $\hbar q$ and $\Delta E = \hbar\omega$ are the momentum transfer and energy loss respectively from an incident electron of kinetic energy E. $\mathrm{Im}(-1/\varepsilon)$, the energy loss function, is the imaginary part of $(-1/\varepsilon)$. The dielectric function $\varepsilon(q,\omega)$ can be theoretically calculated for several free electron metals such as Al. When there is no momentum transfer ($q = 0$), $\varepsilon(0,\omega)$ is the optical dielectric constant which can be obtained through synchrotron irradiation for a wide material range. Proper integration [60, 61] can put equation (2-11) into the form $d\lambda_{in}^{-1}/d(\Delta E)$, giving the probability of an electron losing energy ΔE per unit step length λ_{in}. Stopping power can be obtained in the way of:

$$-\frac{dE}{ds}=\int_0^{E-E_E}(\Delta E)\frac{d\lambda_{in}^{-1}}{d(\Delta E)}d(\Delta E) \qquad (2\text{-}12)$$

This method has been intensively investigated by several groups such as Ding and Shimizu [46, 62], and Kuhr and Fitting [47].The calculated values agree well with both experimental data and Bethe's stopping power in the high energy range beyond 10 keV.

2.2.4 Interaction volume and beam range

As electrons deviate from their original directions in elastic scattering and experience energy loss during inelastic scattering, they will be directed to form a volume with certain width and depth. The interaction volume is the envelope that holds these various electron trajectories. Direct visualization of this volume is possible in the lab and can be easily simulated by Monte Carlo methods that will be introduced below. Certain plastics, such as polymethylmethacrylate (PMMA), undergo a chemical change during electron bombardment that renders the material sensitive to etching in a suitable solvent. This phenomenon is the basis for important steps in the lithography fabrication of semiconductor microcircuits. The information on the interaction volume is important not only for microfabrication, but also for microscopy and microanalysis. It tells how broad and deep the sampling is of the specimen around the incident electron beam.

Beam range R is the average distance traveled by the incident electrons within the solid. This parameter can be used as a coarse estimation of the interaction volume. If a suitable expression is available for the rate of energy loss dE/ds with distance traveled, then a rigorous definition of the total distance traveled by an "average" electron is given by:

$$R=\frac{1}{\rho}\int_0^{E_{PE}}\frac{-1}{dE/ds}dE \qquad (2\text{-}13)$$

At relative high energies, R is several μm; at E<1 keV, R falls with a minimum of several nm at 30-40 eV; and at E<40 eV, $R\sim E^{-2.5}$, not much inelastic scattering events exist [20].

Because of the complex nature of the electron stopping, a number of different definitions of the electron range exist in the literature, of these expressions, the one given by Bethe and Kanaya-Okayama for electron range are the two most frequently cited.

The Bethe range expression for dE/ds in equation (2-12) can be substituted in equation (2-13) so that the integral gives the total distance along an electron trajectory, the so-called Bethe range. The Bethe range finds important applications in x-ray generation calculation. However it significantly overestimates the maximum depth of the interaction volume as it does not take into account the "curl up" effect of the trajectory caused by elastic scattering.

Kanaya and Okayama [63] considered the combined effects of elastic and inelastic scattering to derive an electron range that more closely approximates the depth dimension of the interaction volume:

$$R = \frac{27.6AE_{PE}^{1.67}}{Z^{0.89}\rho} \quad \text{nm} \qquad (2\text{-}14)$$

where E_{PE} is the beam energy in keV, A is the atomic weight in g/mol, Z is the atomic number and ρ is the density of the target material in g/cm^3. Or it can be expressed as:

$$R = \frac{76}{\rho} \cdot (E)^{1.76} \quad \text{nm} \qquad (2\text{-}15)$$

2.2.5 Monte Carlo simulation on electron trajectory

The first approach for the systematic study of scattering processes of fast charged particles in solids was initiated by Berger in 1963 [64]. His approach was based on Bethe's stopping power for energy dissipation and the Rutherford scattering model for trajectory deviation. More systematic investigations were accomplished by Bishop (1965) [65], and Shimizu et al (1965) [66]. Availability of high-speed computers soon allowed the simulations to be run on personal computers and directly based on scattering models. In 1976 a conference entitled "Use of Monte Carlo Calculations in Electron Probe Microanalysis and Scanning Electron Microscopy" was held at the National Bureau of Standards in Washington D.C. (NBS, now is named as National Institute of Standards and Technology (NIST)). The proceedings of that meeting [67] form one of the basic resources for information in this field, and procedures developed by the NBS group have formed the starting point for many of the programs in current use.

The Monte Carlo simulation of electron transport is based on a stochastic description of the scattering process. Electron penetration is approximated by a classical zigzag trajectory (as shown in Figure 2-4). The sample is considered as a structure-less continuum and the step lengths S_i are determined by the randomized scattering mean free paths rather than the crystal lattice parameters. The scattering angles θ_i and ϕ_i are deduced from the elastic scattering model combined with appropriate weighting factors. The coordination for each scattering point is recorded according to equation (2-16). Electron energy loss happens continuously along the trajectory or instantaneously at the scattering point depending on treatment. The trajectories are followed until either the energy of the electron has decreased to arbitrary cut-off energy or the electron escapes from the sample through the surface. The accuracy obtained by the Monte Carlo simulation depends on how precisely the approximations introduced in the model describe these elastic and inelastic scattering processes.

$$\begin{pmatrix} x_{n+1} \\ y_{n+1} \\ z_{n+2} \end{pmatrix} = \begin{pmatrix} x_n \\ y_n \\ z_n \end{pmatrix} + S_n \begin{pmatrix} \sin\theta_n \cos\phi_n \\ \sin\theta_n \sin\phi_n \\ \cos\theta_n \end{pmatrix} \qquad (2\text{-}16)$$

A simple example illustrating the power of the Monte Carlo method is the simulation of the interaction column, as shown in Figure 2-5. The interaction volume as well as the energy dissipation is visualized by recording numerous electron trajectories. The interaction volume is shallower and flatter for high atomic number material (Ag in Figure 2-5 (a) Al in Figure 2-5(b)). Electrons penetrate deeper in material with low atomic number (Al) forming a volume that is narrow right below surface and broad deep into sample, close to the shape of a pear. At a grazing incident, the interaction volume is intercepted by a larger area of the sample surface (Figure 2-5 (c) vs. Figure 2-5 (b)).

2.3 Mechanisms on SE emission

Emission of secondary electrons by bombardment of a sample with fast charged particles is usually described by three distinct stages. First, internal electrons are excited by the incident electrons during penetration. Second, the slowing primary electrons and

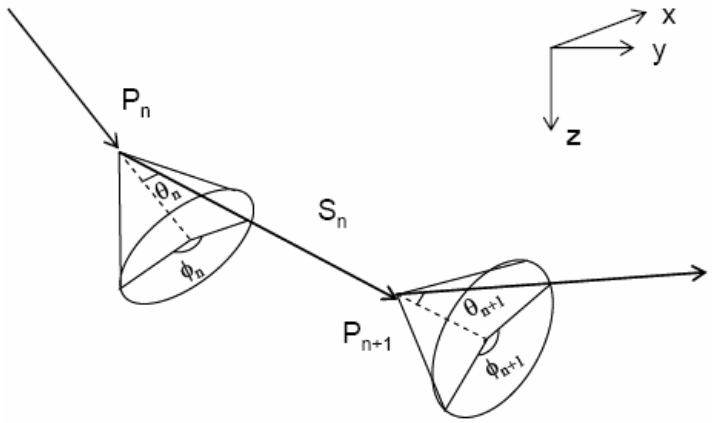

Figure 2-4: Schematic view of an electron trajectory in Monte Carlo simulation [55]

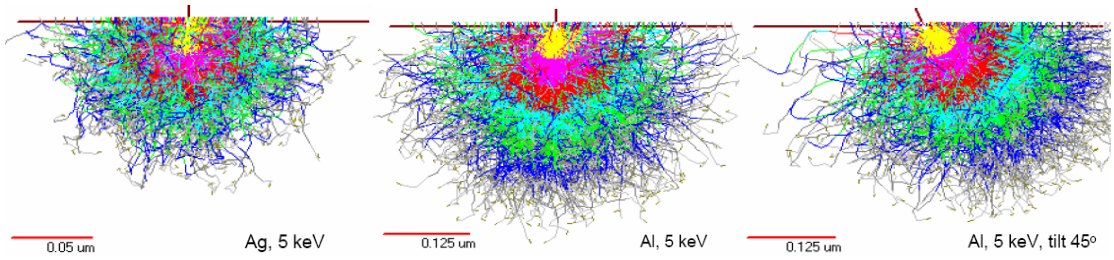

(a) **(b)** **(c)**

Figure 2-5: Monte Carlo simulation of interaction volume of electrons of energy 5 keV with different solids. Incident electron number is 1000. Fading of trajectory color from yellow to gray along depth starting from sample surface represents decrease of electron energy.

(a) Ag, normal incidence; (b) Al, normal incidence; (c) Al, incident angle 45^o

Monte Carlo code (plural scattering model) is by courtesy of Joy D.C.

the excited sample electrons may have enough energy to interact with the medium, leading to a multiplication of SE in a cascade process. Finally, some of the electrons that reach the surface may overcome the energy barrier and escape as true secondary electrons.

2.3.1 SE generation

Secondary electrons are the product of inelastic scattering between fast electrons and sample atoms. Most theories agree that the SE generation is a process of one electron excitations from the conduction and inner shell electrons, and one electron transitions from the plasmon decay for metals. Expressions for the cross section for these individual inelastic events vary among different authors such as Luo and Joy [3, 22], Rosler and Brauer [68], and Shimizu and Ding [55], but the main approaches are similar. The expressions listed below were applied by Luo and Joy [3, 22] in describing noble metals Cu ([Ar]$3d^{10}4s^1$), Ag ([Kr]$4d^{10}5s^1$), Au ([Xe]$4f^{14}5d^{10}6s^1$) and standard metal Al ([Ne]$3s^23p^1$).

2.3.1.1 One electron excitations of valence and d-shell electrons:

The differential cross section for production of SE from valence or d-shell electrons is:

$$d\sigma(E') = \left(\frac{1}{4\pi\varepsilon_0}\right)^2 \frac{\pi e^4 dE'}{EE'^2} \qquad (2\text{-}17)$$

where E is energy of the incident electron E' is the energy transferred by incident electrons to the valance or d-shell electrons.

2.3.1.2 Excitation of core and L shell electrons:

When incident electron energies are big enough the core or L shell electrons can be excited. Gryzinski [69] derived an excitation function according to the semi quantum mechanical treatment:

$$d\sigma(E') = \frac{\pi e^4}{EE'^2}\left(\frac{E}{E+E_j}\right)^{3/2}\left(1-\frac{E'}{E}\right)^{E_j/(E_j+E')} \qquad (2\text{-}18)$$

$$\times\left\{1-\frac{E_j}{E}+\frac{4E_j}{3E'}\ln\left(2.7+\left(\frac{E-E'}{E_j}\right)^{1/2}\right)\right\}dE'$$

where E_j is the binding energy of the core or shell electron.

2.3.1.3 Plasmon excitation:

A plasmon is the collective oscillations of valence electrons caused by penetrating electrons. In this process, the energy losses of the exciting electrons are between 5 and 60 eV. Theoretical calculations of this mechanism were made by Chung and Everhart [70] and are only available for Al. The differential inverse mean free path or probability per distance creating SEs by volume-plasmon decay is:

$$\frac{d(1/\lambda)}{dE} = \lambda_{eff}^{-1}(E_0,\theta_1)D(E,h\omega_p,\Gamma_\upsilon) \qquad (2\text{-}19)$$

where

$$\lambda_{eff}(E_0,\theta_1) = \frac{2a_0E_0}{h\omega_p}\left[\ln\left(\frac{\theta_1^2\theta_E^2}{\theta_E^2}\right)\right]^{-1} \qquad (2\text{-}20)$$

and $D\left(E,h\omega_p,\Gamma_\upsilon\right)$, which describes plasmon decay by one-electron transitions, is

$$D\left(E,h\omega_p,\Gamma_\upsilon\right) = \sum_g n_g g\left|W_g\right|^2\left[\tan^{-1}\left(\frac{E-E_0^g-h\omega_p}{\mathrm{T}_\upsilon\sqrt{2}}\right)-\tan^{-1}\left(\frac{E-E_F-h\omega_p}{\Gamma_\upsilon\sqrt{2}}\right)\right] \times\left\{\pi\sum_g n_g g\left|W_g\right|^2(E_F-E_0^g)\right\}^{-1} \qquad (2\text{-}21)$$

$$E_0^g = \frac{h\omega_p - h^2g^2 - 4\left|W_g\right|^2}{2h^2g^2/m} \qquad (2\text{-}22)$$

where $h\omega_p$ is the plasmon energy, E_0 is the incident electron energy, a_0 is the Bohr radius, and W_g is the g^{th} Fourier coefficient of the lattice pseudo potential for the reciprocal lattice vector g.

Simulations show that in aluminum the majority of the secondaries originate from the volume plasmon decay (mostly at 1 to 3keV), while the contribution from the surface plasmon is negligible [22, 70], as in Figure 2-6. For all metals valence electrons

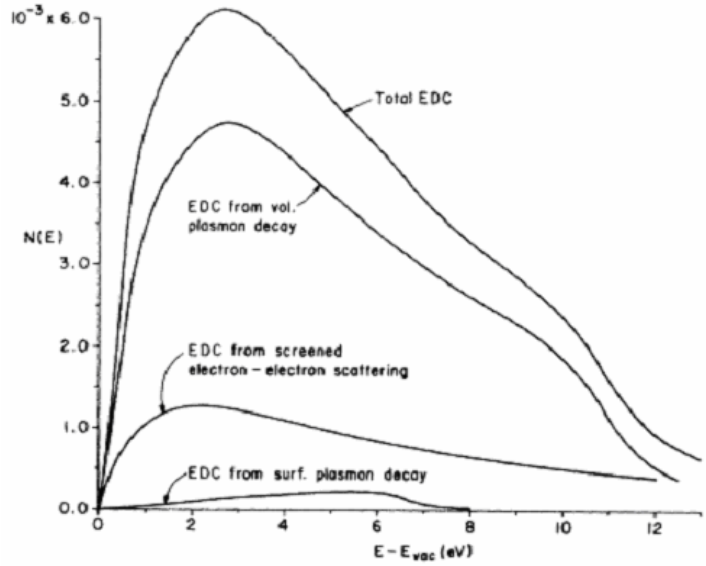

Figure 2-6: The contributions as noted in the figure to the secondary electron for Al under 1 keV of beam energy. Data is calculated theoretically by Chung and Everhart [70].

contribute a large part to the secondaries. While for Cu, Ag, and Au the contribution of the d-electrons is also important.

2.3.2 SE transportation

In the inelastic SE generation process, the primary electron transfers part of its energy to the excited internal secondary. Each of these two electrons, in turn, may have energy high enough for generating new secondary electrons, giving rise to electron multiplication or cascade process, or they may escape directly out of the sample. This process continues until the energies of the cascade fall to some minimum value at which there are no inelastic processes of sufficiently large cross section for further interaction. The cascade then diffuses through the sample, suffering mostly elastic scattering events, until the SE either escapes into the vacuum or drops back to join the sea of conduction and valence electrons in the solid. The theory of SE multiplication by cascade was first pointed out by Wolff [36]. It is this important mechanism that explained why a primary electron can generate more than one secondary electron from most materials.

In the cascade process, a single SE can undergo inelastic interactions with core or outer shell electrons by the same mechanisms discussed previously for PE. As the

cascade progresses, the energies of most secondaries will decrease to about ten electron volts (or more) relative to the bottom of the conduction band before escaping, or interacting with conduction electrons and plasmons, in the case of metals. Electron-phonon interactions also undoubtedly occur, but the fact that SE from metals is independent of temperature indicates that they play only a minor role in the slowing down process [23].Since both of the elastic and inelastic mean free paths are about several angstroms in this low energy range, the scatterings will happen very locally, as in Figure 2-7. The maximum distance between the initiation point of a cascade and the eventual escape through the surface by a SE is of the order of 5 to 15 nm for most materials. At the end of the cascade process, the energy of the SE is not high enough to cause more inelastic collisions. The cascade then diffuses through the sample, suffering mostly elastic scattering events, until the SEs are either thermalized or, if they have approached the surface potential barrier at a suitable angle and with sufficient energy, escape to the vacuum.

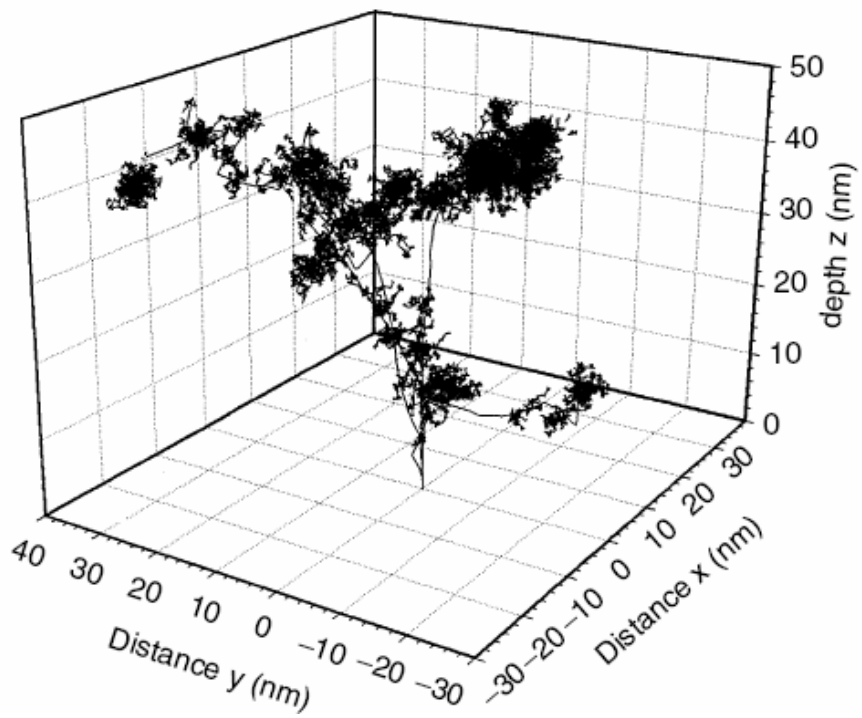

Figure 2-7: 3-dimentional trajectory of 4 primary electrons with energy of 5 keV penetrating in Cu. The clustered clouds illustrated the SE cascades happened locally at the end of the trajectory.

Figure source: Ding and Shimizu [46].

2.3.3 SE escape

Due to the discontinuity of the potential in the vicinity of surface, a slow electron may be refracted or even reflected at such a barrier. For a slow secondary electron with energy E approaching the surface with angle α relative to the surface normal (Figure 2-8), the quantum mechanical transmission probability is:

$$T = \frac{4\sqrt{1 - U_0 / E\cos^2\alpha}}{\left(1 + \sqrt{1 - U_0 / E\cos^2\alpha}\right)^2} \qquad E\cos^2\alpha > U_0$$
$$T = 0 \qquad \text{otherwise} \qquad (2\text{-}23)$$

where U_0 is the inner potential. For metals $U_0 = E_F + \phi \approx 10eV$, where E_F is the Fermi energy and ϕ is the work function; for insulators or semiconductors $U_0 = \chi \approx 1eV$. In classical treatments the maximum angle α at which the SE can approach the surface is determined by taking the normal component of momentum $P\cos\alpha$ equal to the value

$$P_c = \sqrt{2m}(E_F + \phi) \qquad (2\text{-}24)$$

Thus the escape probability $p(E)$ for an SE of energy E at the surface is [18]

$$p(E) = \frac{\int_0^{\alpha} \sin\alpha d\alpha \int_0^{2\pi} d\phi}{2\pi} = 1 - \cos\alpha = 1 - \frac{P_c}{P} = 1 - \sqrt{\frac{E_F + \Phi}{E}} \qquad (2\text{-}25)$$

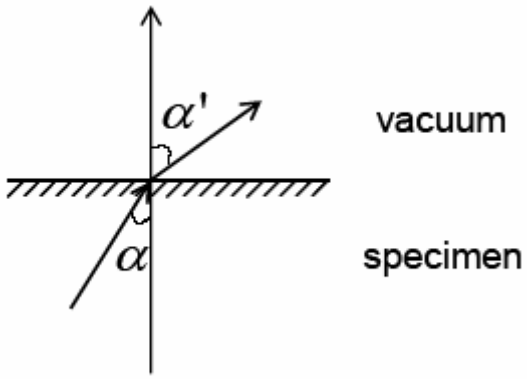

Figure 2-8: Illustration of angles for SE approaching sample surface.

2.4 Semi empirical models

Semi-empirical explanations of the phenomena of secondary emission were well developed before the more advanced investigations based on the quantum mechanical theories and Monte Carlo simulation techniques. Semi-empirical models developed by Bethe [31], Salow [32], Baroody [33], Jonker [34], Bruining [35], and Dekker [23] etc. are still in favor today because of their effectiveness and simplicity. Errors arising from the use of semi-empirical treatments are negligible when compared to the uncertainty of experimental measurements or advanced theoretical calculations. In the semi-empirical models, only the generation and transportation processes are considered. All SEs that arrive the surface are assumed to escape.

2.4.1 Constant SE generation energy

Dekker [23] first used the stopping power based on the continuous slowing down approximation to estimate the SE generation rate $n(E)$:

$$n(E) = \frac{1}{\varepsilon} \cdot \left(-\frac{dE}{ds} \right) \qquad (2\text{-}26)$$

where s is the path length measured along the electron trajectory, dE/ds is the stopping power of the incident electron, and ε is the effective energy required to produce a secondary electron. It is obvious from equation (2-25) that two basic assumptions are applied: first, the SE excitation energy is constant, and second, all inelastic scatterings causing energy loss of the primary electrons effectively contribute to SE generation. The constant SE generation energy is over-simplified since the mechanisms for SE excitation vary at different ranges of electron energy. Equation (2-25) also over-estimates the number of SE produced since the inelastic scattering can cause other excitations such as X-rays, rather than secondary electrons.

2.4.2 Straight-line approximation on SE transportation

The straight-line approximation of the SE escape probability is the statistical result of the SE cascade. It assumes that the internal SEs will experience no more elastic scattering events between the site of SE generation and the sample surface. It also assumes that the

SEs will move to the surface along a "straight line" after being excited during the inelastic event, as in Figure 2-9 (a). Any inelastic scattering causes absorption within this distance. The escape probability of these electrons at depth z is simply given by an exponential (equation 2-26), characterized by a mean escape depth and the escape angle α with respect to surface normal ($\alpha = (90^o - \theta)$ with θ noted in Figure 2-9).

$$p_z = A\exp\left(-\frac{z}{\lambda_{in}\cos\alpha}\right) \qquad (2\text{-}27)$$

where A is a constant of order of unity and λ_{in} is the inelastic mean free path. λ_{in} is the maximum depth from which a SE can escape, thus it is called the SE escape depth λ_{es}. It can also be view as the attenuation of the emitted electron flux caused by inelastic scattering, and in that case called attenuation length λ_{at}. This theory on SE escape was applied in the early SEE descriptions by Baroody [33] and Bruining [35], and although the assumptions are not strictly valid [70], the error that is introduced is usually negligible.

In fact, it is known that the scattering of excited SE does not produce absorption of all these SE. On average, a SE undergoes averagely 0.5 inelastic scatterings and 7 elastic

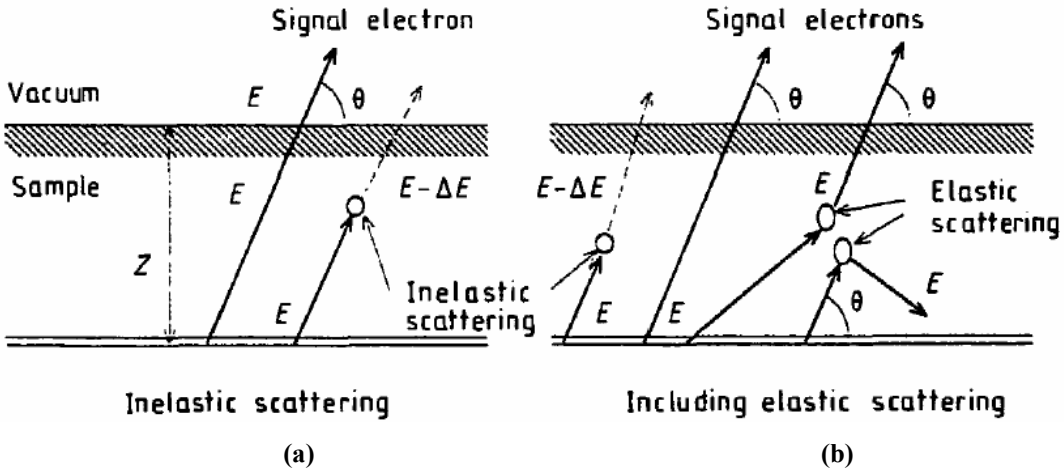

Figure 2-9: Schematic illustrations of the effect of elastic scattering on the SE escape depth.

(a) Only inelastic scatterings are counted, SE escape along a straight line (b) The elastic scattering cause trajectory of SE deviate from a straight line

Figure source: Shimizu and Ding [55].

scatterings before escaping, according to Devooght et al [71] and as illustrated in Figure 2-9 (b). The deeper a SE escapes from the solid, the more elastic scatterings it could experience. The SE escape probability should be modified as:

$$P(z) = A\exp\left(-\frac{z}{\lambda_{at}(E)\cos\alpha}\right) \qquad (2\text{-}28)$$

The attenuation length λ_{at} is always smaller than the inelastic mean free path λ_{in} by the "curling-up" effect of the elastic scattering. Werner et al.[72, 73] and Kuhr and Fitting [47] found that the mean attenuation length approaches the inelastic mean free path in the energy range E>100eV. Jablonski [74] states that the elastic scattering results in a reduction of 30% of λ_{es} or λ_{at} and Shimizu and Ding [55] indicate 20%. However for energies below 100eV the scattering dominated by elastic scattering and the attenuation length passes a minimum, approaching roughly 20% of the inelastic mean free path (Figure 2-10).

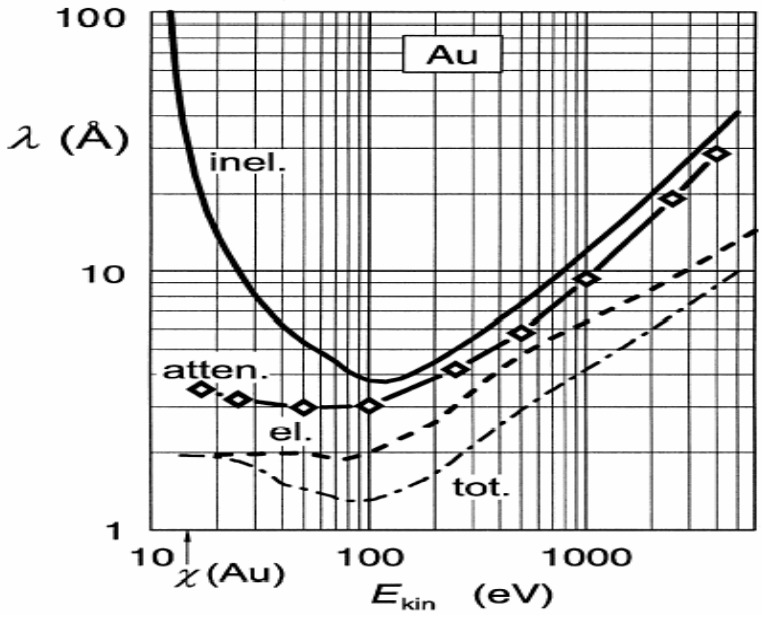

Figure 2-10: Comparison of inelastic MFP, elastic MFP, total MFP (of elastic and inelastic) and mean SE attenuation length varying with electron kinetic energy. Atten in the figure is the SE attenuation length λ_{at} or escape depth λ_{es}.

Figure source: Kuhr and Fitting [47].

Though the semi-empirical method is simple and is effective in explaining certain phenomena, it has unavoidable deficiencies. Aside from the over-simplification of SE generation and the transport probability, the contribution of reflected electrons and the cascade multiplication are difficult to include in this model. Monte Carlo methods can track the electron from the point it starts in the solid to the point it escapes, as well as calculate each deviation of the trajectory from a "straight line", and also take into account the multiplication of the reflected and the cascade electrons.

2.5 Monte Carlo simulation methods

The Monte Carlo method has been widely applied predicting SE behavior since the initial work of the groups in Nantes (Cailler and Ganachaud [37] in 1972) and Osaka (Koshikawa and Shimizu [10] in 1974). Construction of a Monte Carlo model for SE production involves three separate steps: determining the trajectory of the incident electron, computing the rate of SE generation along each portion of this trajectory, and finally calculating the fraction of SE that escape from the solid after a series of cascade processes. The various treatments of the SE emission process can be combined into the Monte Carlo models. The Monte Carlo method can be used to simulate the details of each scattering following a direct simulation scheme or to calculate semi-empirically following the continuous slowing-down approach. Often, these two schemes are combined and used as hybrid models.

2.5.1 Direct simulation scheme

The basic assumption of the direct method is that the interactions of charged particles with the scattering centers take place locally and instantaneously. Between two successive collisions, the particle propagates freely, with its energy and momentum unchanged. Large deflection angles caused by elastic scattering can be deduced from Rutherford or Mott scattering model. Secondary electrons are generated at the inelastic scattering centers with energy E_s and scattering angles determined by whatever inelastic scattering model was selected, as shown in Figure 2-11. This assumption is valid if it is first assumed that the scattering centers are random and the potential inside the solid is

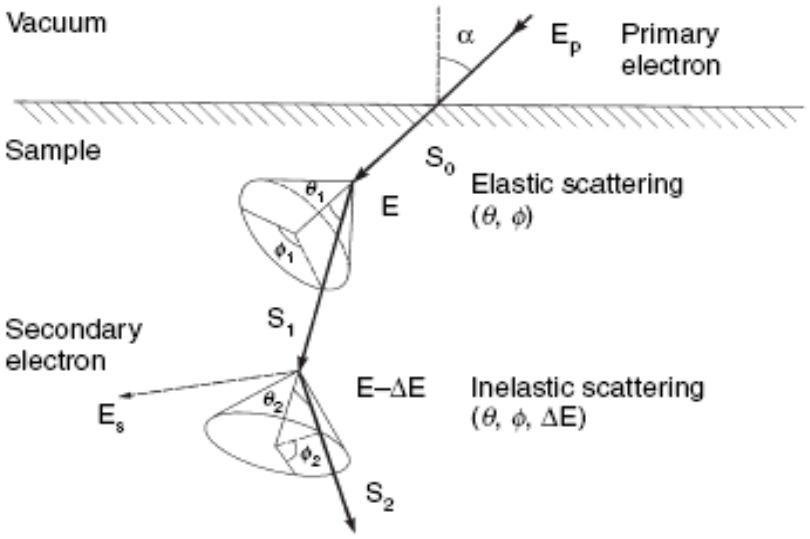

Figure 2-11: Schematic illustration of electron scattering and trajectory in direct Monte Carlo simulation.

Image source: Ding and Shimizu [46].

uniform. In the direct simulation scheme, one follows the particle history and single scattering events are treated one at a time.

From a theoretical viewpoint, calculating individual inelastic scattering processes is the most basic approach to understanding the SE excitation. Simulations of SE emission from Al agree well with experimental data. However, this approach requires exact knowledge of individual inelastic scattering events, and such information is only available for a few materials, most notably aluminum.

2.5.2 Continuous slowing-down scheme

The continuous slowing-down scheme is applied to evaluate the stopping power in relation to inelastic scattering and to calculate the SE generation rate in semi-empirical empirical methods. A similar approach can be used in the Monte Carlo simulation. The main assumptions of this method are that the energy degradation of the charged particles is a continuous process along the trajectory whereas large angle scatterings occur locally and instantaneously at scattering centers. The screened Rutherford formula or a partial

wave expansion is used to calculate large angle deflection caused by elastic scattering, and the stopping power dE/ds is used to evaluate the energy degradation. If the i th segment of the trajectory has a length S_i, the residual electron energy E_i after the i th segment is given by:

$$E_i = E_{i-1} - \left|\frac{dE}{ds}\right|_i S_i \qquad (2\text{-}29)$$

The choice of the path length S_i is arbitrary. In practice, one can take a fixed value for the order of magnitude of the total mean free path (single scattering model), or a fixed fraction of the total beam range (plural scattering model). The continuous slowing-down method requires less computational effort than the direct simulation method and can be applied at relative high beam energy. It is important to notice that this model neglects the fluctuations of the energy loss making it well suited for calculating integral characteristics. However, it is unable to predict differential characteristics, such as fine structure appearing in the energy spectrum.

2.5.3 Hybrid scheme

2.5.3.1 Hybrid stopping power

Since the contribution of valence electrons to the generation of secondary electrons is significant for most of metals, it is important to take them into account separately in the Monte Carlo simulations. A hybrid scheme applied on stopping power offers a compromise between the unavailability of the scattering function, long calculation times, and the over-simplification of the continuous slowing-down scheme. Applying a hybrid model to the stopping power means to treat the contributions of inner shell and valence electrons separately. Depending on the basic assumptions and functional forms taken, this problem is treated differently by different groups.

Shimizu and Ding[55] assumed that the generation of SE was composed of the stopping of inner shell and valence electrons, as shown in Figure 2-12. In this model each individual inner-shell ionization was simulated according to Gryzinski's formula, while the stopping power of the valence electrons is taken as the difference between the Bethe's

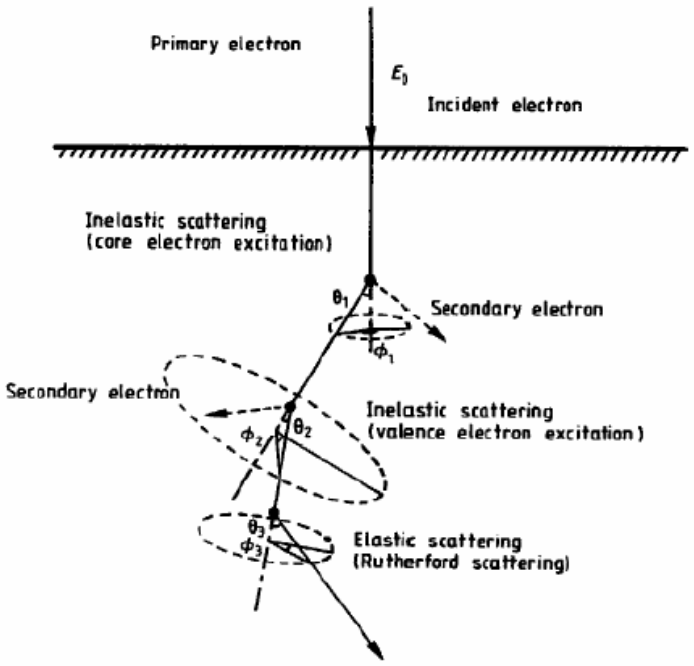

Figure 2-12: Schematic illustration on the source of SE generation. The contribution of shell and valence electrons are treated separately.

formula and the total contribution of the inner shells $\sum_n \left(-dE/ds\right)_n$.

$$\left(-\frac{dE}{ds}\right)_{valence} = \left(-\frac{dE}{ds}\right)_{Bethe} - \sum_n \left(-\frac{dE}{ds}\right)_n \qquad (2\text{-}30)$$

This scheme has been used by several researchers, including Reimer and Krefting [44], Murata [75], and Ichimura and Shimizu [44, 55, 64, 76], to simulate the generation of secondary electrons in compounds and alloys.

In his fast secondary model, Joy [18] treats the SE produced when an incident electron interacts with a free electron (so called knock-on collisions) using the cross section suggested by Evans[77]:

$$\frac{d\sigma}{d\Omega} = \frac{\pi e^4}{E^2}\left(\frac{1}{\Omega} + \frac{1}{(1-\Omega)^2}\right) \qquad (2\text{-}31)$$

where E is the incident electron energy. Ω $(\Omega < 0.5)$is a random number determining the probability that an inelastic event will happen, the energy (ΩE) and the deflection angle of the generated secondary electron. Between two inelastic events, both the scattered incident electrons and generated secondary electrons are continuously slowed down. This

model is simple but useful for evaluating the spatial distribution of secondary electrons or the electron energy deposited in the interaction volume, which ultimately determines the spatial resolution for electron beam lithography and x-ray microanalysis at high beam energies [18, 78]. As shown in Figure 2-13, the spatial spread of the secondary electron is broadened into an almost cylindrical shape by the fast secondary electrons and is deviated almost perpendicularly to the beam penetration.

2.5.3.2 Hybrid SE cascade process

The straight-line approximation is used to semi-empirically estimate the probability that a secondary electron can escape. It is manipulated by Luo and Joy [3, 22] to not only describe diffusion of the SEs to reach the sample surface, but also calculate the probability of producing new SEs. Since $p_{z'}$ is the probability for a SE with energy E to travel from z to z' without any collision,

$$p_{z'} = 0.5 \exp\left(- \frac{|z - z'|}{\lambda(E) \cos 45^{o}} \right) \qquad (2\text{-}32)$$

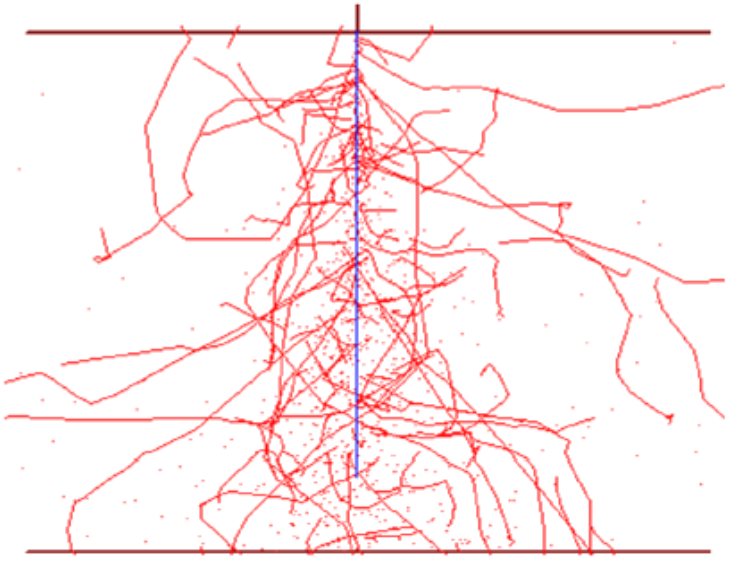

Figure 2-13: Monte Carlo simulation on the fast secondary electron trajectory in PMMA thin film. Dots are birth places for those SE with low energy; lines are the trajectory of those with high enough energy. Parameters are: film thickness 50nm, beam energy 5 keV, electron trajectory 1000.

Monte Carlo code (fast secondary electron model) is by courtesy of Joy D.C.

The probability $p_{z'+\Delta z'}$ for the SE to travel from z to $z'+\Delta z'$ without any inelastic collision is:

$$p_{z'+\Delta z'} = 0.5\exp\left(-\frac{|z-(z'+\Delta z')|}{\lambda(E)\cos 45^o}\right) \quad (2\text{-}33)$$

so that between z' and $z'+\Delta z'$ the probability for the SE to interact with another electron and to take part in the cascade is $\Delta p_{z'}$

$$\Delta p_{z'} = p_{z'} \cdot \Delta z' / \lambda(E)\cos 45^o \quad (2\text{-}34)$$

In the formula above $\lambda(E)$ is the inelastic mean free path which can be calculated using the proper formula, such as equation 2-6.

SE cascade multiplication treated in this way can produce reasonable SE yield and save significant calculation time since the part of SE that escape do not need to be tracked any further. Because most of the generated SE do not have energies high enough to travel a long distance, the spatial distribution simulated by this model is usually acceptable.

2.6 Conclusions

The emission of SE can be divided into three steps: generation by various mechanisms, cascade multiplication inside the sample and during transport to the surface and finally escape from the sample by overcoming the surface energy barrier. Secondary electrons are the product of inelastic scattering between the primary or high-energy internal secondaries and the sample atoms. Secondaries can be excited from core and outer shell-electrons, conduction or valence electrons, and by one electron transitions of plasmon decay. Plasmon decay contributes the greatest part of SE for near free-electron metal, such as aluminum. Conduction or valence electrons play important roles for most materials.

Calculating the SE emission can be categorized into three main types: semi-empirical methods, Monte Carlo methods and treating the SE transport by solving the Boltzmann equation. In the semi-empirical method, a constant excitation is combined with the electron stopping power to calculate the SE generation rate; the exponential decay law is applied to estimate the SE escape probability. The Monte Carlo method can be used to

directly simulate the detailed trajectory and treat the scattering events one by one; or by following the continuous scheme to estimate the integral characteristics of SE. A hybrid Monte Carlo model can be created by combing several different schemes to simulate experimental results with the advantage of strengthening important contributions.

3. Chapter Ⅲ: Optimizing the SE yield database

3.1 Introduction

Secondary electron yield δ, defined as the number of secondaries produced per incident electron, has been analyzed and measured as one of the important parameters since the first observation of SE. The information that is required in any study on the secondary electron emission is how the yield δ varies with incident energy E_{PE} of the [79]primary electron beam. Consequently in the century since secondary electrons were identified, secondary yield δ has been measured as a function of primary electron energy E_{PE} and atomic number Z for materials of interest, including both elements and compounds. Such yield profiles are useful for investigative purpose in many technological areas such as SEM imaging[7], particle accelerators, plasma TV displays [24, 79], the performance of high voltage insulators, and the stability of space satellites in the solar wind [5]. They also provide a way of testing and calibrating Monte Carlo simulations for electron-solid interactions and SE generation [18].

A compilation of SE yield profiles is available for download from http://pciserver.bio.utk.edu [80] and also from http://www.napchan.com/bse/index.htm or directly from the authors. This database includes incident electron energies up to 50 keV, and covers 51 elements and 42 compounds, representing over 80 years of published data from more than 100 different research groups. An initial examination of the data in this collection is discouraging, because it is evident that even for common elements (such as aluminum or gold) for which there are often a dozen or more independent sets of data available, the level of agreement is rarely better than 25%, often showing relative divergences of 100% or more. The result of this situation is that anyone seeking yield data to explain an observation or to validate a model can usually find multiple values spanning a large enough range to support or disprove any assertion.

The “universal yield curve of SE production” [7, 23, 32] is one of the products of the semi-empirical theory on secondary emission. It can be used as a tool to examine the experimental results contained in the database, to identify and correct the possible

sources of error in the data, and then to generate an optimized SE yield profile for each element (providing there is an adequate supply of experimental results is available). We believe that these synthesized yield profiles provide much more reliable data on secondary electron emission for predictive or test purposes than the corresponding "raw" published values. As an additional benefit the magnitude of the several parameters discussed below, which appear in the analytical expression for the yield curve, can be examined as a function of atomic number Z to provide additional insights into the way in which secondary electron emission depends on the target material.

3.2 Examining the database

The experimental SE yield values in the database represent the work of more than 100 authors spread over a time period of nearly 100 years. Consequently the quality of the data varies greatly and, except for those examples where only a single set of measurements is available, there are always significant variations between yield values at a given energy. These differences may be the result of sample preparation, experimental arrangement, or poor laboratory technique.

Figure 3-1 shows the available 13 sets of separately measured $\delta(E_{PE})$ data for aluminum, a typical near-free-electron metal that has been extensively studied as a standard material. It can be seen that although all of the data agrees that the maximum SE yield δ^m occurs at an energy value of 400 eV, the measured value of δ^m is variously quoted from 0.5 to 3.3. Therefore, the question is how relative numerical values of the yield versus energy can be obtained given the often enormous spread of experimental values. This goal can be realized through a tool called the "universal law of SE yield" to extract the best estimate of the SE yield $\delta(E_{PE})$ versus energy E_{PE} from these assorted data sets.

3.3 Optimizing the database

3.3.1 The semi-empirical universal law

As discussed in section 2.4, in the semi empirical approach, the emission of

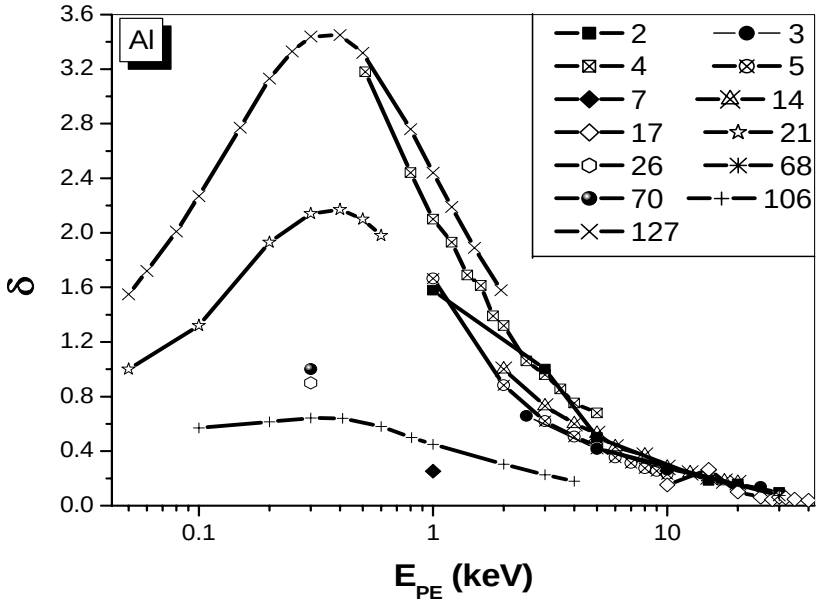

Figure 3-1: Plot of the measurements on the SE yield δ as a function of primary beam energy E_{PE} for Al. Numbers following the symbols are the references cited in the database [80]. For all the curves while E_{PE}^{m} are at about 400 eV, δ^{m} vary between 0.5 and 3.3.

secondaries is controlled only by the generation and transportation steps. The secondary electron (SE) emission rate $\delta(E_{PE})$ depends on the rate $n(z,E)$ at which SE are generated as a function of depth z [7, 23] and the probability $p(z)$ [33, 35] that a generated SE will escape back to the incident surface.

$$n(z,E) = -\frac{1}{\varepsilon}\cdot\frac{dE}{ds} \qquad (3\text{-}1)$$

where s is the path length measured along the electron trajectory, dE/ds is the stopping power of the incident electron, and ε is the effective energy required to produce a secondary electron.

$$p(z) = A\exp(-\frac{z}{\lambda}) \qquad (3\text{-}2)$$

where $A = 0.5$ assuming that SE are scattered symmetrically in the specimen. λ is the SE attenuation length. Thus

$$\delta(E_{PE}) = \int n(z,E)\cdot p(z)\cdot dz \qquad (3\text{-}3)$$

For all materials for which data has been obtained (http://pciserver.bio.utk.edu and http://www.napchan.com/bse/index.htm), the general yield curve of $\delta(E_{PE})$ with E_{PE} has the shape shown in Figure 1-7. The yield rises from zero at the lowest energies, reaches a maximum δ^m at some energy E_{PE}^m with $\delta^m \approx 1$, and $E_{PE}^m \approx 1$ keV and then falls monotonically as about $1/E_{PE}$ at higher energies.[7, 23]

Because all experimental yield curves have this same generic shape, there have been many attempts to provide an analytical description of the profile. The simplest approach would be to assume a constant stopping power [23, 32, 81], then

$$-\frac{dE}{ds} = \frac{E_{PE}}{R} \qquad (3\text{-}4)$$

where R is the range or penetration depth of the incident electron. Equation (3-3) then gives

$$\delta = 0.5\frac{E_{PE}}{\varepsilon} \cdot \frac{\lambda}{R}(1 - e^{-R/\lambda}) \qquad (3\text{-}5)$$

Other simple approximations describing the stopping power[7, 81] give similar results to equation (3-5). The electron range R as a function of energy E_{PE} is

$$R = \frac{B}{\rho} \cdot (E_{PE})^n \qquad (3\text{-}6)$$

where $n = 1.67$ according to Lane and Zaffarano[82], $B = 76\,\text{nm}$ for E_{PE} in keV, and ρ is the density of the target material in g/cm^3.

Dionne[83] calculated the maximum SE yield δ^m and the corresponding primary energy E_{PE}^m by differentiating an equation similar to (3-5), and showed that when $\delta = \delta^m$,

$$\frac{R}{\lambda} = (1 - \frac{1}{n})(e^{R/\lambda} - 1) \qquad (3\text{-}7)$$

So for $n = 1.67$,

$$R(E_{PE}^m) = 1.614\lambda \qquad (3\text{-}8)$$

Substitution (3-8) into (3-6) gives,

$$E_{PE}^m \approx 0.099(\rho \cdot \lambda)^{0.60} \qquad (3\text{-}9)$$

Substitution of (3-9) into (3-5) gives

$$\delta^m \approx \frac{0.024(\rho \cdot \lambda)^{0.60}}{\varepsilon} \qquad (3\text{-}10)$$

It has been proved that δ^m / E_{PE}^m is a constant of material characteristics[18, 26]. In our calculation,

$$\frac{\delta^m}{E_{PE}^m} = \frac{0.248}{\varepsilon} \qquad (3\text{-}11)$$

Because ε and λ are not known in general, they must be eliminated from the expression. This can be done by combining equation (3-5), (3-6), (3-9), (3-10), which gives δ / δ^m as a function of E_{PE} / E_{PE}^m that is independent of the material:

$$\frac{\delta}{\delta^m} = 1.28\left(\frac{E_{PE}}{E_{PE}^m}\right)^{-0.67}\left(1 - \exp\left(-1.614\left(\frac{E_{PE}}{E_{PE}^m}\right)^{1.67}\right)\right) \qquad (3\text{-}12)$$

This result is usually referred to as "the universal law for SE yield" and provides a conventional description of the phenomena of SE emission. Other forms of this law have been given by many other authors[7, 23, 33, 34, 83, 84]. The fitting of the universal curve with the measurements in the database is shown as a dashed line in Figure 3-2 for Al. The

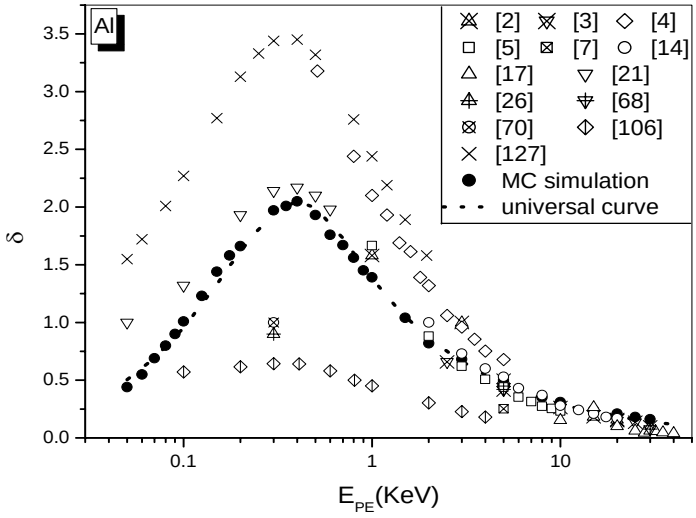

Figure 3-2: Plot of the measurements and calculations on the SE yield δ as a function of primary beam energy E_{PE} for Al.

universal curve with E_{PE}^{m}=0.4 keV and δ^{m}=2.5 fits several sets of measured data, approaching the mean value of the measurements and providing the general SE yield profile for the target material aluminum. A Monte Carlo simulation method can fill the same optimizing purpose.

3.3.2 Calculating the SE yield by Monte Carlo method

For the purposes of computing a SE yield curve against energy given values of E_{PE}^{m}, δ^{m} or correspondingly ε, λ , a simple Monte Carlo (MC) extension [85] of the model of Salow[32] or Dekker[23] can be used. The basic assumptions and modifications of this model by Joy [18] are:

1. The SE generation rate follows the equation (3-1). Instead of assuming a constant stopping power, the modified Bethe's stopping power by Luo and Joy [3, 18, 22, 59] (equation 2-10) is used in the calculation. This treatment incorporates more detailed information like atomic number Z, atomic weight A, and mean ionization potential J of the target material. The effective SE excitation energy ε is the parameter that needs to be inserted into the simulation.
2. All SE that reach the sample can escape. The escape probability $p(z)$ follows the equation (3-2), within which λ is another parameter that needs to be assumed. The multiplication of SE during transportation is considered by incorporating the hybrid model on the SE cascade process as described in section 2.5.3.
3. The electron scattering is treated using a modified plural scattering model. Each trajectory with a total length of the beam range is assumed to be composed of 50 steps of equal length to save calculation time. The deflection angle is calculated from the corrected Rutherford cross-section [41]. Secondaries are generated along each of these steps as a result of the slowing down of the primary electrons and escape from the midpoints of these steps. All electron incidences are assumed normal to the sample surface, and the electron trajectory number is set larger than 2000 for good statistics.

On a modern PC this computation can be carried out very rapidly for energies between 0.1 and 20keV with specified ε and λ values, and provide a completed yield curve that combines the essential concept of the universal law with the added benefit of an enhanced physical model. Under most circumstances, the agreement between the universal curve according to equation (3-5) and the Monte Carlo (MC) simulation with inserted ε, λ values is very good. Either representation of the yield could therefore be employed. For convenience, in the subsequent discussion, both versions will be displayed, as shown in Figure 3-2.

3.3.3 Optimization template and procedures

Figure 3-3 shows yield curves calculated using the MC model discussed above, assuming the sample to be aluminum and varying the parameters ε and λ. For example, the two profiles for which $\lambda = 1nm$ have similar shapes with a maximum yield occurring at 0.3 keV. Similarly the two profiles for which $\lambda = 3nm$ also show δ^m occurring at the same energy (0.5keV). This is, of course, consistent with equation (3-8). Changing the value of λ, while keeping ε constant leads to a shift in E_{PE}^{m} as well as a change in the value of δ^m. If we treat the data of Figure 3-3 as a template, then it is clear that those experimental data sets which show smaller E_{PE}^{m} represent smaller λ values. Smaller or larger values of δ^m can similarly be correlated with higher or lower values of ε. Note also that at high energies ($E_{PE} >> E_{PE}^{m}$), the yield δ is directly dependent on $(\lambda/\varepsilon)E_{PE}^{1-n}$ according to equation (3-5) and (3-6) and thus has a slope of about $(\lambda/\varepsilon)E_{PE}^{-n}$.

Our procedure has therefore been to empirically fit the available yield curves from different authors for a given material using the results of equations (3-8), (3-9) and (3-10) and to estimate initial ε and λ values which are then incorporated into the Monte Carlo simulation. The fit of this prediction with the various experimental results is then optimized to obtain final values of ε, λ and hence of δ^m and E_{PE}^{m}. By focusing on ε, λ and hence the shape of the yield curve, rather than on the actual values of δ, a more reliable assessment of the data can be made.

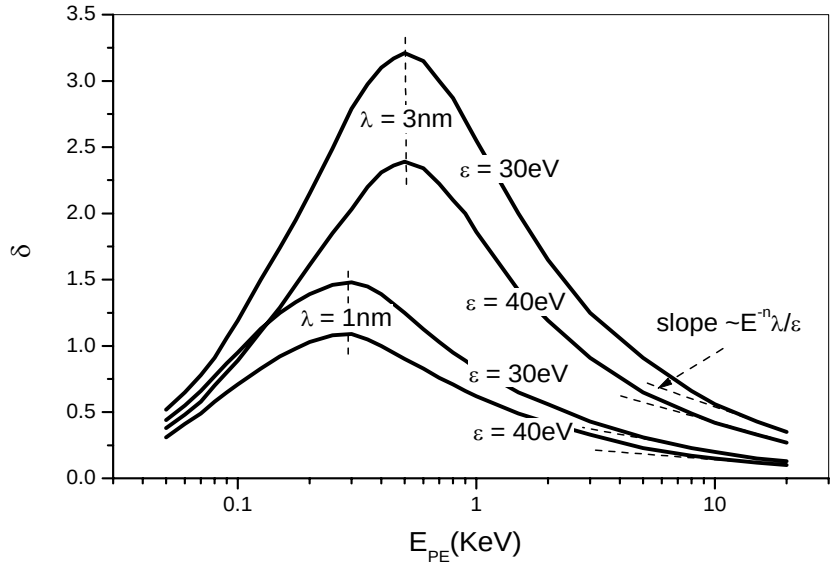

Figure 3-3: Template for MC simulation of SE yield profile. SE excitation energy ε and effective escape depth λ are two key parameters.

The database contains results for 51 elements. Most of these have two or more independent sets of data, and 19 have five or more. In a few cases the data is very sparse and consists only of E_{PE}^{m} , δ^m values and no attempt has been made to analyze this data. For the 44 remaining examples, the procedures discussed above can be used to obtain "best practice" values for ε , λ and then to derive the corresponding SE yield curve to provide $\delta(E_{PE})$ values at energies for which no experimental data is available.

The Al data of Figure 3-2 and the Ti data of Figure 3-4 exemplify the problems discussed above. The multiple data sets show significant differences in $\delta(E_{PE})$ and δ^m values. However for both elements the E_{PE}^{m} values are in good agreement, and in both cases the variations of $\delta(E_{PE})$ with E_{PE} at high energies are similar. From these observations we can here deduce the most probable values for λ and λ/ε . Inserting these parameters into equation (3-5) or into the MC model then generates yield curves which are clearly in good agreement with the overall shape and magnitude of the yield profile and which provide a quality estimate of δ at any energy.

The same procedure has been applied to all 44 of the useful data sheets to produce ε and λ values, and the corresponding yield profiles. The yield curves can then be

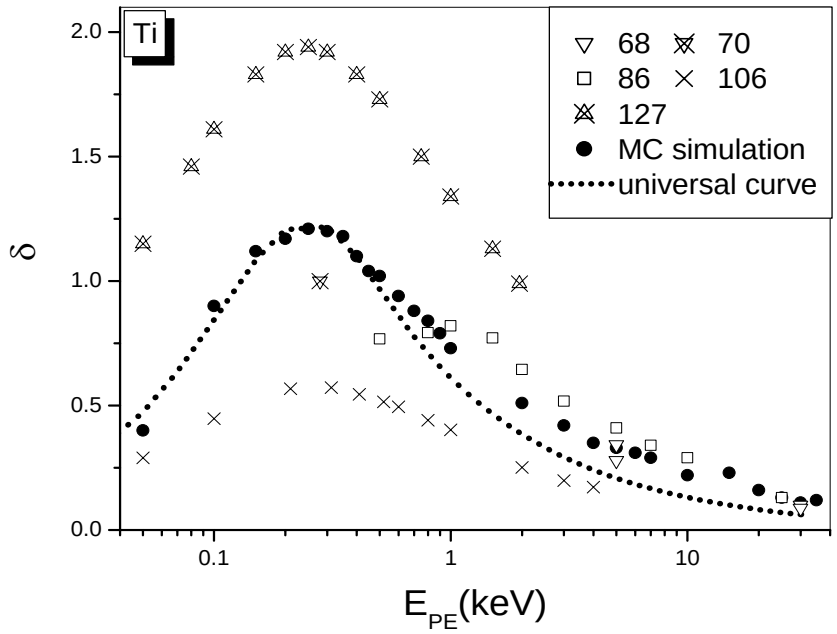

Figure 3-4: Plot of the measurements and calculations on the SE yield δ as a function of primary beam energy E_{PE} for Ti.

The universal curve is calculated according to equation (3-12) with E_{PE}^{m}=0.25 keV and δ^{m}=1.21; the Monte Carlo (MC) simulation is calculated with λ=0.5 nm and ε=25 eV inserted; other symbols represent measurements with numbers followed corresponding to the references cited in the database [80].

generated by downloading the Monte Carlo program from http://pciserver.bio.utk.edu/metrology and inserting the appropriate values, or by applying equation (3-5) and using a suitable range equation.

3.4 Results and discussion

The optimized SE yields for the 44 elements in the database are listed in Table 3-1 and plotted in Figure 3-5. The optimum values of ε, λ for each element are tabulated in Table 3-2. We believe that these values and the yield curves generated by using them represent the most reliable estimate of SE emission data that is presently available for modeling and interpretive purposes. Table 3-2 also lists δ^{m}, E_{PE}^{m} and the optimized yield δ at 2 and 20keV for each of the 44 elements analyzed together with their work function ϕ [86] and mass density ρ [87, 88]. The variations of these parameters with the

Table 3-1: Optimized SE yields for the 44 elements under various primary energies.

PE(keV)	*0.02*	*0.04*	*0.05*	*0.06*	*0.08*	*0.1*	*0.15*	*0.2*	*0.25*	*0.3*	*0.4*	*0.5*	*0.6*	*0.7*
Li (3)	0.37	0.27	0.24	0.33	0.46	0.52	0.59	0.55	0.49	0.43	0.36	0.31	0.27	0.24
Be(4)	0.27	0.22	0.2	0.24	0.35	0.41	0.52	0.54	0.52	0.49	0.42	0.36	0.31	0.27
B(5)	0.49	0.4	0.37	0.46	0.64	0.78	1.02	1.13	1.13	1.11	0.95	0.83	0.7	0.64
C(6)	0.27	0.23	0.21	0.25	0.37	0.46	0.67	0.83	0.93	1	1.05	1.03	0.97	0.89
Mg(12)	0.36	0.29	0.24	0.31	0.44	0.55	0.71	0.78	0.78	0.76	0.7	0.64	0.59	0.53
Al(13)	0.63	0.5	0.45	0.56	0.81	1.02	1.43	1.7	1.84	1.96	1.99	1.91	1.78	1.65
Si(14)	0.23	0.17	0.16	0.2	0.29	0.38	0.54	0.67	0.75	0.82	0.88	0.89	0.84	0.82
K(19)	0.15	0.1	0.09	0.12	0.18	0.21	0.25	0.27	0.26	0.26	0.23	0.21	0.19	0.18
Ca(20)	0.24	0.15	0.12	0.21	0.29	0.33	0.34	0.32	0.29	0.29	0.26	0.24	0.22	0.2
Sc(21)	0.46	0.3	0.28	0.38	0.53	0.63	0.72	0.72	0.72	0.69	0.64	0.58	0.54	0.5
Ti(22)	0.63	0.46	0.39	0.52	0.75	0.9	1.1	1.21	1.17	1.19	1.13	1.03	0.95	0.87
Cr(24)	0.43	0.33	0.28	0.38	0.55	0.69	0.98	1.24	1.4	1.55	1.74	1.79	1.77	1.75
Fe(26)	0.41	0.29	0.26	0.34	0.5	0.62	0.84	1	1.08	1.11	1.13	1.1	1.08	1
Ni(28)	0.31	0.23	0.2	0.26	0.38	0.48	0.71	0.87	1.01	1.09	1.21	1.25	1.24	1.22
Cu(29)	0.53	0.39	0.32	0.46	0.65	0.79	1.12	1.29	1.46	1.47	1.54	1.48	1.46	1.37
Zn(30)	0.17	0.13	0.11	0.15	0.21	0.28	0.42	0.54	0.63	0.74	0.86	0.98	1.04	1.05
Ga(31)	0.21	0.15	0.14	0.17	0.26	0.34	0.49	0.6	0.69	0.74	0.8	0.81	0.83	0.81
Ge(32)	0.36	0.26	0.24	0.29	0.43	0.54	0.71	0.85	0.94	0.97	1.02	0.99	0.9	0.9
Se(34)	0.49	0.32	0.26	0.4	0.57	0.69	0.81	0.88	0.89	0.85	0.79	0.72	0.7	0.67
Sr(38)	0.27	0.18	0.14	0.22	0.31	0.38	0.45	0.48	0.5	0.48	0.46	0.43	0.42	0.38
Y(39)	0.27	0.18	0.16	0.22	0.32	0.4	0.51	0.59	0.62	0.63	0.63	0.62	0.59	0.56
Zr(40)	0.42	0.29	0.24	0.34	0.48	0.6	0.74	0.81	0.83	0.82	0.79	0.77	0.72	0.67
Nb(41)	0.65	0.43	0.34	0.55	0.76	0.9	1.08	1.19	1.17	1.14	1.09	1.05	1.01	0.92
Mo(42)	0.32	0.22	0.21	0.27	0.38	0.48	0.69	0.84	0.98	1.06	1.16	1.19	1.18	1.21
Pd(46)	0.35	0.26	0.22	0.27	0.42	0.54	0.78	0.95	1.09	1.23	1.36	1.45	1.41	1.38
Ag(47)	0.37	0.27	0.24	0.31	0.47	0.58	0.81	0.98	1.13	1.21	1.35	1.39	1.39	1.36
Cd(48)	0.27	0.2	0.17	0.23	0.33	0.44	0.6	0.75	0.86	0.95	1.06	1.15	1.17	1.18
In(49)	0.44	0.31	0.26	0.35	0.54	0.66	0.9	1.03	1.16	1.18	1.28	1.26	1.22	1.2
Sn(50)	0.41	0.28	0.24	0.33	0.49	0.59	0.8	0.93	1.03	1.1	1.14	1.13	1.11	1.1
Sb(51)	0.24	0.18	0.16	0.21	0.3	0.38	0.54	0.69	0.81	0.9	1.04	1.12	1.15	1.19
Te(52)	0.33	0.22	0.19	0.26	0.38	0.47	0.64	0.72	0.79	0.81	0.82	0.83	0.77	0.75
Cs(55)	0.27	0.19	0.16	0.22	0.33	0.4	0.54	0.62	0.67	0.69	0.7	0.71	0.65	0.65
Ba(56)	0.31	0.21	0.19	0.25	0.37	0.46	0.61	0.7	0.76	0.81	0.82	0.81	0.8	0.78
La(57)	0.3	0.2	0.17	0.24	0.35	0.42	0.56	0.64	0.69	0.71	0.71	0.71	0.67	0.64
Hf(72)	0.4	0.27	0.25	0.32	0.48	0.61	0.83	1	1.15	1.24	1.32	1.39	1.33	1.37
Ta(73)	0.29	0.21	0.18	0.24	0.34	0.43	0.59	0.7	0.8	0.84	0.93	0.94	0.93	0.93
W(74)	0.58	0.36	0.28	0.47	0.67	0.81	0.98	1.01	1.02	1.04	1.02	0.99	0.97	0.96
Re(75)	0.36	0.26	0.22	0.29	0.42	0.54	0.73	0.87	0.98	1.08	1.14	1.14	1.15	1.17
Pt(78)	0.57	0.39	0.33	0.45	0.64	0.83	1.13	1.32	1.46	1.53	1.65	1.65	1.7	1.68
Au(79)	0.48	0.32	0.26	0.37	0.57	0.67	0.9	1.04	1.15	1.22	1.3	1.31	1.31	1.22
Hg(80)	0.37	0.26	0.24	0.31	0.44	0.56	0.76	0.9	1.03	1.12	1.24	1.23	1.24	1.24
Tl(81)	0.41	0.28	0.23	0.32	0.48	0.59	0.78	0.9	0.99	1.04	1.08	1.07	1.07	1.07
Pb(82)	0.4	0.27	0.23	0.31	0.46	0.58	0.75	0.86	0.94	1.01	1.03	1.04	0.99	1
Bi(83)	0.23	0.17	0.14	0.19	0.28	0.35	0.51	0.63	0.72	0.79	0.89	0.92	0.97	0.99

Table 3-1 continued

PE(keV)	*0.8*	*1*	*1.5*	*2.5*	*3*	*4*	*5*	*6*	*8*	*10*	*15*	*25*	*30*
Li (3)	0.21	0.19	0.14	0.1	0.09	0.07	0.06	0.05	0.04	0.03	0.03	0.02	0.02
Be(4)	0.24	0.21	0.16	0.11	0.1	0.08	0.07	0.06	0.05	0.04	0.03	0.02	0.02
B(5)	0.57	0.48	0.38	0.26	0.25	0.21	0.16	0.15	0.11	0.11	0.07	0.05	0.05
C(6)	0.79	0.68	0.51	0.33	0.3	0.25	0.21	0.19	0.14	0.12	0.09	0.07	0.05
Mg(12)	0.47	0.43	0.33	0.25	0.22	0.2	0.15	0.14	0.12	0.09	0.07	0.05	0.06
Al(13)	1.55	1.38	1.05	0.77	0.67	0.56	0.51	0.46	0.34	0.33	0.24	0.19	0.16
Si(14)	0.77	0.68	0.51	0.34	0.34	0.28	0.26	0.21	0.17	0.16	0.12	0.1	0.08
K(19)	0.17	0.15	0.12	0.09	0.08	0.07	0.06	0.05	0.05	0.04	0.03	0.03	0.03
Ca(20)	0.2	0.18	0.15	0.12	0.1	0.09	0.09	0.07	0.07	0.05	0.04	0.04	0.04
Sc(21)	0.46	0.41	0.36	0.26	0.24	0.21	0.19	0.18	0.14	0.13	0.13	0.09	0.08
Ti(22)	0.82	0.76	0.6	0.47	0.42	0.37	0.33	0.29	0.26	0.21	0.19	0.13	0.14
Cr(24)	1.68	1.5	1.23	0.92	0.81	0.7	0.61	0.56	0.47	0.41	0.34	0.22	0.24
Fe(26)	0.91	0.83	0.68	0.53	0.46	0.4	0.34	0.3	0.29	0.24	0.19	0.14	0.16
Ni(28)	1.23	1.12	0.91	0.69	0.6	0.51	0.47	0.42	0.36	0.27	0.23	0.17	0.16
Cu(29)	1.28	1.18	0.96	0.76	0.7	0.53	0.5	0.46	0.41	0.35	0.28	0.21	0.2
Zn(30)	1.05	1.08	0.95	0.71	0.62	0.53	0.46	0.41	0.36	0.3	0.24	0.17	0.15
Ga(31)	0.78	0.72	0.57	0.44	0.4	0.33	0.3	0.28	0.25	0.2	0.16	0.13	0.11
Ge(32)	0.81	0.75	0.61	0.49	0.45	0.37	0.32	0.33	0.26	0.23	0.19	0.15	0.13
Se(34)	0.64	0.58	0.49	0.41	0.36	0.32	0.29	0.29	0.22	0.21	0.17	0.12	0.11
Sr(38)	0.37	0.34	0.29	0.23	0.21	0.19	0.17	0.15	0.14	0.12	0.09	0.07	0.07
Y(39)	0.54	0.5	0.41	0.33	0.31	0.27	0.23	0.2	0.18	0.16	0.13	0.11	0.08
Zr(40)	0.64	0.61	0.5	0.43	0.4	0.34	0.31	0.26	0.25	0.22	0.18	0.15	0.12
Nb(41)	0.91	0.82	0.71	0.55	0.55	0.47	0.43	0.37	0.32	0.34	0.27	0.21	0.18
Mo(42)	1.18	1.09	0.9	0.67	0.65	0.55	0.5	0.46	0.38	0.35	0.29	0.22	0.19
Pd(46)	1.38	1.28	1.07	0.9	0.79	0.69	0.63	0.54	0.47	0.42	0.34	0.26	0.25
Ag(47)	1.33	1.27	1.06	0.85	0.78	0.68	0.59	0.53	0.48	0.44	0.34	0.26	0.27
Cd(48)	1.11	1.06	0.94	0.74	0.64	0.56	0.51	0.46	0.41	0.35	0.29	0.21	0.23
In(49)	1.17	1.06	0.93	0.74	0.65	0.59	0.53	0.5	0.4	0.37	0.31	0.26	0.22
Sn(50)	1.04	0.96	0.85	0.67	0.6	0.53	0.49	0.42	0.39	0.35	0.28	0.24	0.19
Sb(51)	1.17	1.11	1	0.75	0.73	0.6	0.54	0.5	0.42	0.36	0.3	0.25	0.23
Te(52)	0.71	0.67	0.57	0.47	0.41	0.38	0.34	0.31	0.27	0.25	0.2	0.18	0.14
Cs(55)	0.63	0.57	0.51	0.41	0.37	0.33	0.31	0.29	0.26	0.21	0.19	0.13	0.12
Ba(56)	0.73	0.66	0.59	0.48	0.44	0.39	0.36	0.32	0.29	0.26	0.23	0.16	0.17
La(57)	0.62	0.59	0.52	0.42	0.4	0.34	0.32	0.3	0.25	0.22	0.2	0.15	0.14
Hf(72)	1.39	1.27	1.16	0.89	0.88	0.79	0.69	0.64	0.57	0.54	0.48	0.34	0.32
Ta(73)	0.91	0.85	0.76	0.64	0.57	0.53	0.45	0.4	0.37	0.34	0.3	0.24	0.18
W(74)	0.9	0.85	0.77	0.68	0.63	0.55	0.55	0.48	0.43	0.39	0.32	0.26	0.24
Re(75)	1.11	1.1	0.97	0.81	0.75	0.65	0.59	0.55	0.49	0.46	0.36	0.28	0.23
Pt(78)	1.59	1.52	1.34	1.13	1.06	0.92	0.83	0.8	0.7	0.64	0.57	0.45	0.37
Au(79)	1.19	1.14	1.05	0.88	0.82	0.73	0.66	0.62	0.53	0.47	0.42	0.34	0.33
Hg(80)	1.23	1.16	1.04	0.87	0.82	0.71	0.65	0.63	0.57	0.52	0.41	0.33	0.28
Tl(81)	0.99	0.95	0.84	0.76	0.7	0.62	0.57	0.51	0.44	0.44	0.34	0.26	0.23
Pb(82)	0.95	0.93	0.82	0.68	0.67	0.59	0.53	0.48	0.43	0.39	0.33	0.27	0.26
Bi(83)	0.99	0.99	0.83	0.74	0.67	0.61	0.55	0.5	0.44	0.41	0.35	0.25	0.24

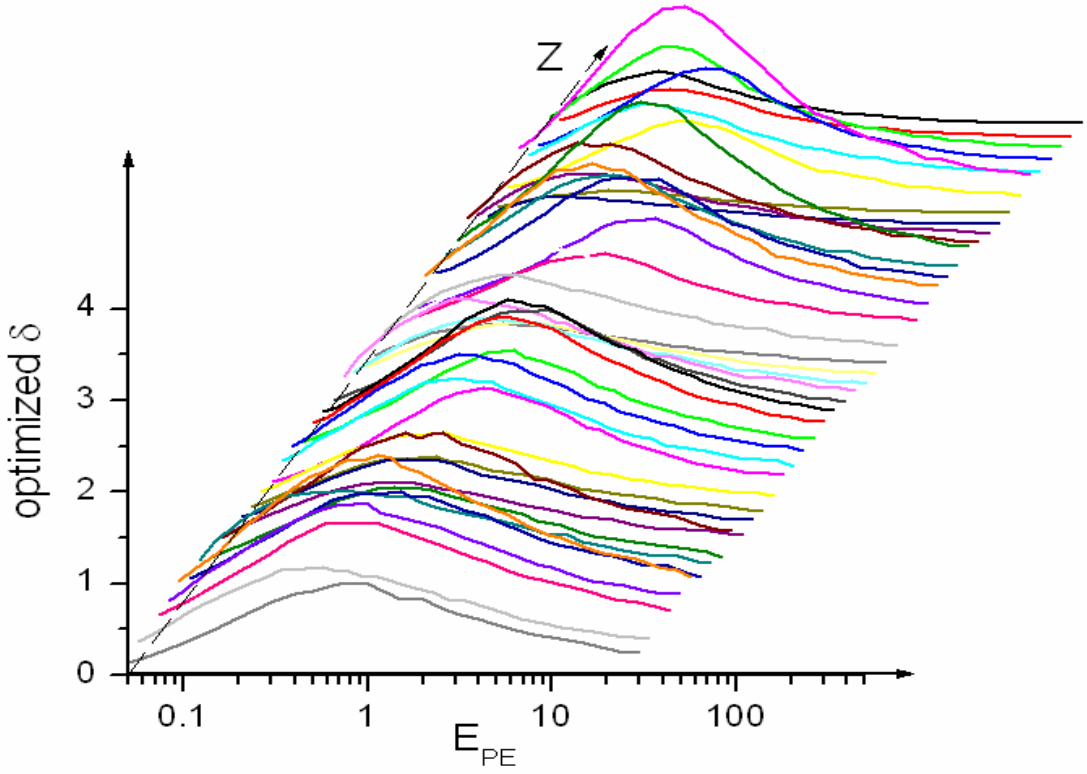

Figure 3-5: A plot of data in table 3-1 for the optimized SE yield for the 44 elements under various primary energies.

Table 3-2: A list of the optimization results for the elements in the database [80].

Atom	*Z*	ε	λ	$\frac{\varepsilon}{\lambda}$	*R (nm)*	$\frac{R}{\lambda}$	δ^m	E_{PE}^m *(keV)*	$\frac{\delta^m}{E_{PE}^m}$	δ *at 20keV*	δ *at 2keV*	ϕ + *(eV)*	ρ ++ *(g/cm3)*
Li	3	45	2.0	2.25	8	4.00	0.59	0.15	3.93	0.03	0.14	2.9	0.533
Be	4	70	1.0	7.0	3	3.00	0.55	0.20	2.75	0.02	0.11	4.98	1.85
B	5	40	1.0	4.0	3	3.00	1.05	0.24	4.38	0.06	0.32	4.45	2.34
C	6	80	2.5	3.2	7	2.80	1.06	0.40	2.65	0.08	0.37	5	2.27
Mg	12	50	1.3	3.85	6	4.62	0.80	0.24	3.33	0.07	0.32	3.66	1.74
Al	13	32	1.7	1.88	10	4.71	2.00	0.40	5.00	0.19	0.84	4.28	2.7
Si*	14	90	2.7	3.33	12	4.44	0.89	0.45	1.98	0.08	0.44	4.85	2.33
K	19	100	2.0	5.0	16	8.00	0.27	0.22	1.23	0.02	0.12	2.3	0.862
Ca	20	40	0.5	8.0	5	10.0	0.33	0.15	2.20	0.05	0.14	2.87	1.53
Sc	21	30	0.5	6.0	4	8.00	0.76	0.20	3.80	0.11	0.3	3.5	2.99
Ti	22	25	0.5	5.0	4	8.00	1.21	0.25	4.84	0.16	0.51	4.33	4.51
Cr	24	47	1.2	3.92	6	6.67	1.80	0.60	3.00	0.27	1.01	4.5	7.13
Fe	26	45	0.6	7.5	4	6.67	1.15	0.35	3.29	0.15	0.58	4.5	7.86
Ni	28	65	1.0	6.5	5	5.00	1.19	0.50	2.38	0.20	0.7	5.15	8.91
Cu	29	35	0.6	5.83	4	6.67	1.53	0.40	3.83	0.24	0.83	4.65	8.96
Zn	30	120	2.5	4.80	11	4.40	1.03	0.70	1.47	0.19	0.72	4.33	7.13
Ga	31	90	1.5	6.00	8	5.33	0.78	0.45	1.73	0.13	0.48	4.2	5.91
Ge	32	50	1.0	5.00	8	8.00	1.00	0.40	2.50	0.15	0.53	5	5.32
Se	34	28	0.5	5.60	5	10.0	0.86	0.25	3.44	0.13	0.44	5.9	4.81
Sr	38	50	1.0	5.00	11	11.0	0.49	0.25	1.96	0.09	0.27	2.59	2.58
Y	39	60	1.0	6.00	11	11.0	0.65	0.40	1.63	0.12	0.35	3.1	4.48
Zr	40	35	0.5	7.00	5	10.0	0.83	0.30	2.77	0.14	0.51	4.05	6.51
Nb	41	20	0.3	6.67	3	10.0	1.16	0.25	4.64	0.25	0.65	4.3	8.58
Mo	42	60	1.0	6.00	7	7.00	1.14	0.50	2.28	0.25	0.74	4.6	10.22
Pd	46	55	1.0	5.50	7	7.00	1.41	0.55	2.56	0.32	0.94	5.12	12
Ag	47	50	1.0	5.00	9	9.00	1.43	0.60	2.38	0.31	0.96	4.26	10.5
Cd	48	70	1.5	4.67	13	8.67	1.16	0.65	1.78	0.26	0.82	4.22	8.65
In	49	40	1.0	4.00	11	11.0	1.29	0.50	2.58	0.27	0.81	4.12	7.29
Sn	50	43	1.0	4.30	10	11.0	1.12	0.50	2.24	0.27	0.77	4.42	7.29
Sb	51	80	2.5	3.20	16	7.60	1.16	0.70	1.66	0.25	0.89	4.7	6.69
Te	52	50	1.0	5.00	9	9.00	0.84	0.35	2.40	0.19	0.5	4.95	6.25
Cs	55	60	3.5	1.71	38	10.9	0.72	0.40	1.80	0.16	0.46	2.14	1.9
Ba	56	53	2.0	2.65	24	12.0	0.83	0.45	1.84	0.19	0.53	2.7	3.59
La	57	54	1.0	5.40	15	15.0	0.72	0.50	1.44	0.15	0.44	3.5	6.17
Hf	72	45	1.0	4.50	11	11.0	1.39	0.60	2.32	0.37	1.07	3.9	13.1
Ta	73	60	0.7	8.57	9	12.9	0.93	0.65	1.43	0.37	0.66	4.25	16.67
W	74	20	0.2	10.0	3	15.0	1.06	0.25	4.24	0.31	0.71	4.55	19.25
Re	75	50	0.6	8.33	7	11.7	1.20	0.60	2.00	0.34	0.88	4.96	21.02
Pt	78	30	0.5	6.00	6	12.0	1.69	0.55	3.07	0.47	1.22	5.65	21.4
Au	79	35	0.5	7.00	7	12.0	1.28	0.50	2.56	0.37	0.94	5.1	19.29
Hg	80	48	1.0	4.80	14	14.0	1.23	0.70	1.76	0.36	0.98	4.49	13.6
Tl	81	40	0.8	5.00	11	13.8	1.09	0.50	2.18	0.3	0.76	3.84	11.9
Pb	82	40	0.8	5.00	12	15.0	1.06	0.50	2.12	0.28	0.72	4.25	11.4
Bi	83	80	2.0	4.00	20	10.0	0.98	0.70	1.40	0.31	0.79	4.22	9.8

*** Silicon crystal**

+ data reference [86]

++ data reference [87, 88]

atomic number Z will be analyzed below.

3.4.1 Optimized yield, δ^m and E_{PE}^m

Figure 3-6 shows the optimized SE yield for the 44 elements at 2 keV and 20 keV respectively varying with atomic number Z. The yields vary in the range between less than 0.1 to 1.2, and generally increase with atomic number. The most obvious characteristic of the profile is that at the place when an atomic shell is filled and another new shell begins e.g. Z=3 (Li), Z=11(Na), Z=19 (K), Z=37 (Rb), Z=55 (Cs), the yields are lowest in the valley, while in about the middle of each period e.g. Z=13 (Al), Z=27 (Ni), Z=47 (Ag) the yields peak (especially for E_{PE}=2 keV), showing a shell filling effect. The trend has a similar profile to that of the mass density (Figure 3-7); C, Al, and Ni are the peak elements for the 2nd, 3rd, 4th periods respectively on both profiles. There is a lack of data for the 5th period, but a similar increase is observed for the first half of this period. Since density enters into the electron range R in equation (3-6), the proportionality between the yields and the density means that the primary penetration depth plays a predominant role in secondary electron emission.

The variation of E_{PE}^m and δ^m with atomic number Z (Figure 3-8) has the same trends suggesting the shell filling effect. The similarity between E_{PE}^m and ρ is reasonable according to equation (3-9) given that the attenuation length λ has less effect on E_{PE}^m as compared to ρ. It is interesting to notice that E_{PE}^m and δ^m have very similar profiles (Figure 3-8 (c)), indicating that the SE excitation energy ε is a relatively constant value for all 44 metal elements examined, according to equation (3-11).

Copeland [89] and Sternglass [90] have investigated the relationship of δ^m or some related quantity of the δ curve with the atomic number Z and concluded that δ^m could be a physical parameter revealing atomic shell information. Similar effect has been found on ion-induced SE yields [91]. Our results show a similar response with respect to atomic shell structure and reveal that the magnitude of E_{PE}^m, δ^m and related δ value are determined primarily by the mass density ρ and only slightly adjusted by the SE

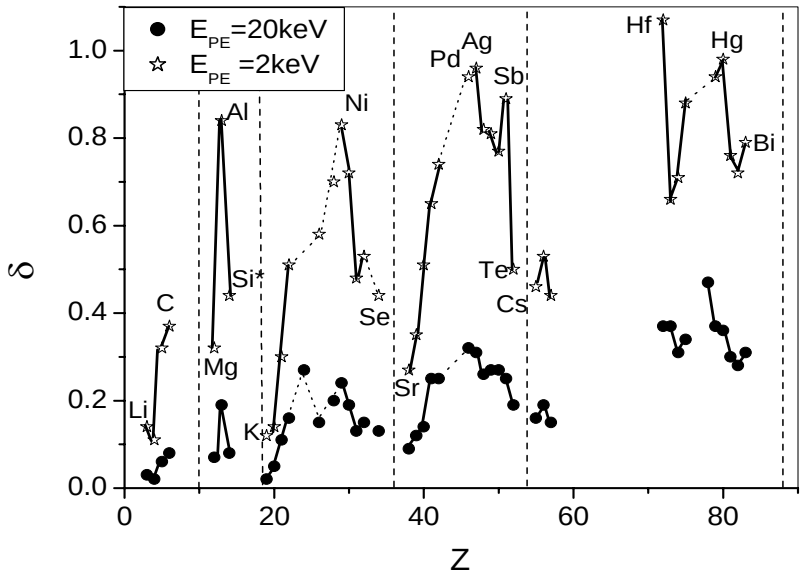

Figure 3-6: SE yield δ as a function of atomic number Z has similar trends for beam energy E_{PE} at 2 keV and 20 keV. Solid lines connect neighboring elements; dashed lines connect elements with uncontinuous atomic number.

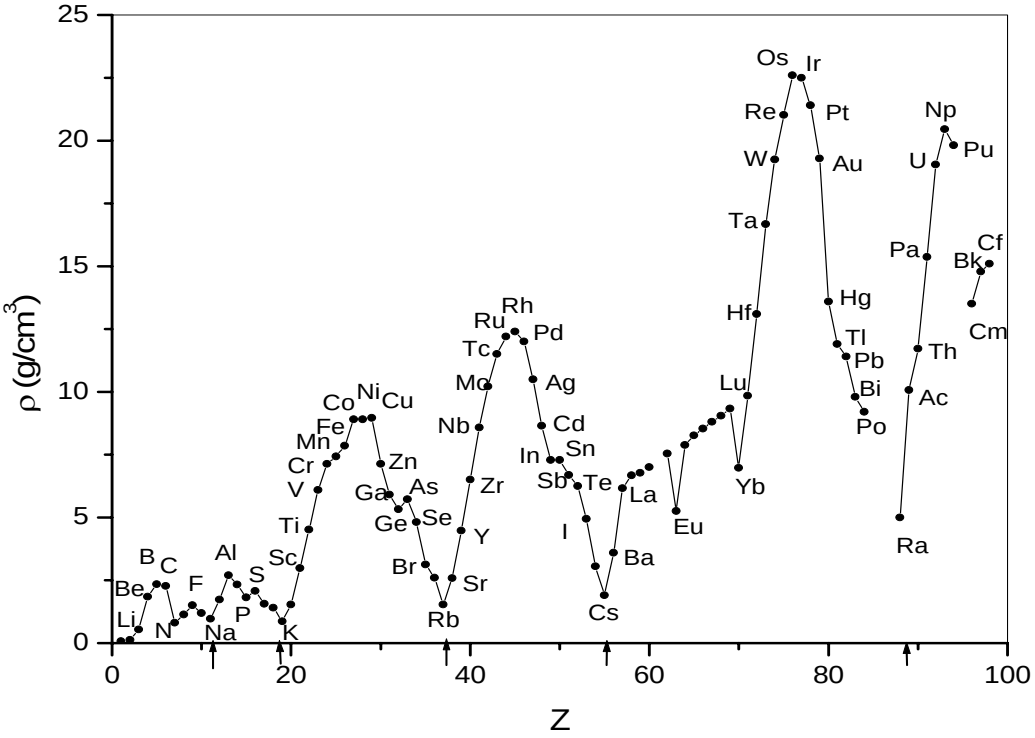

Figure 3-7: Variation of mass density ρ with atomic number Z has strong shell filling effect.

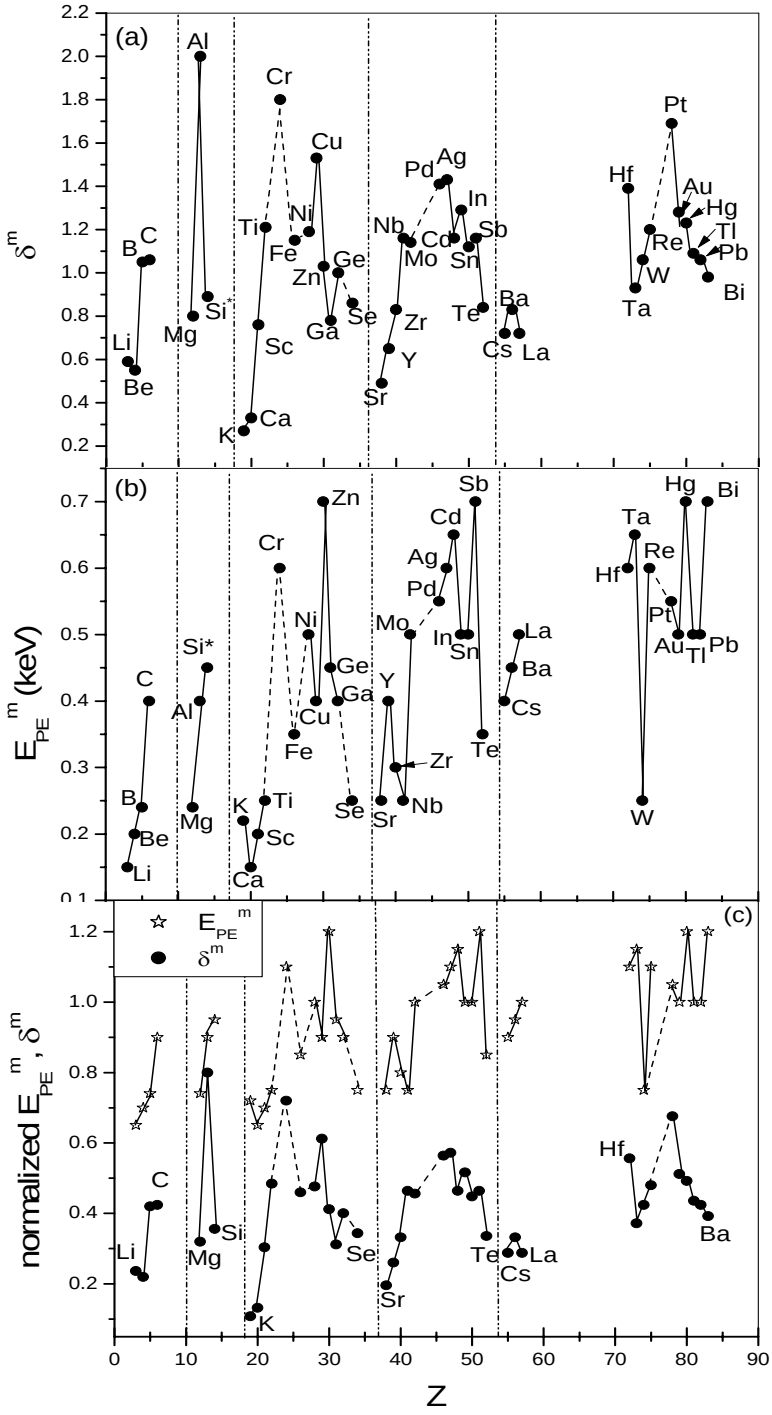

Figure 3-8: Maximum SE yield δ^m (a) and corresponding primary energy E_{PE}^m (b) as functions of atomic number Z. (c) E_{PE}^m normalized to 1keV and δ^m normalized to 2.5 show recognizable similar shape and shell filling effect. Solid lines connect neighboring elements, dashed lines connect non-consecutive atomic number. Normalized E_{PE}^m are shifted 0.5 up to make plot clear.

excitation energy ε and the mean attenuation length λ. No simple relationship between δ^m and ρ as stated by Barut [92] or between δ^m and work function ϕ as stated by Baroody [33] is observed in our results, and as shown in Figure 3-9.

3.4.2 ε, λ and R

The SE excitation energy ε varies in the range of 20~120 eV with mean value of about 50 eV, which is several times the first ionization energies (varying in the range of 5~25 eV [88]) and about one tenth of the mean ionization potential (varying the range of 20~900 eV [18]) in calculating the stopping power. Since ε is the average effect for each of the individual SE excitation process, it is hard to assert that it has any simple relationship with any of these single ionization potentials. The mean attenuation length λ is in the range of 0.2~3.6 nm with most values clustered around 1 nm, which is reasonable because this value is close to the inelastic MFP for the secondaries with energies around 10 eV for most metals. Variations around this value are acceptable by taking into account the adjustment by possible elastic scattering during the escape of the SE. By examining Figure 3-10 it is clear that our simulation results indicate that ε and λ are scattered along the atomic number Z. No shell filling property seems to be owned by these two parameters, but their varying trends with Z show strikingly similarity (Figure 3-10 (c)).

A plot of the work function ϕ and the SE excitation energy ε (Figure 3-11) as a function of Z also shows that there is no simple relation between these two parameters, indicating that the SE yield variation with Z is not solely due to changes in the work function. It is interesting to show that, contrary to equation (3-8) or the well believed semi empirical theory, the beam range at the primary energy E_{PE}^m is not a constant time of the SE attenuation length λ, but increases almost linearly with atomic number Z (Figure 3-12). A proper explanation to this phenomenon is yet to be found.

3.5 Conclusions

The semi empirical calculation and Monte Carlo simulation based on the available

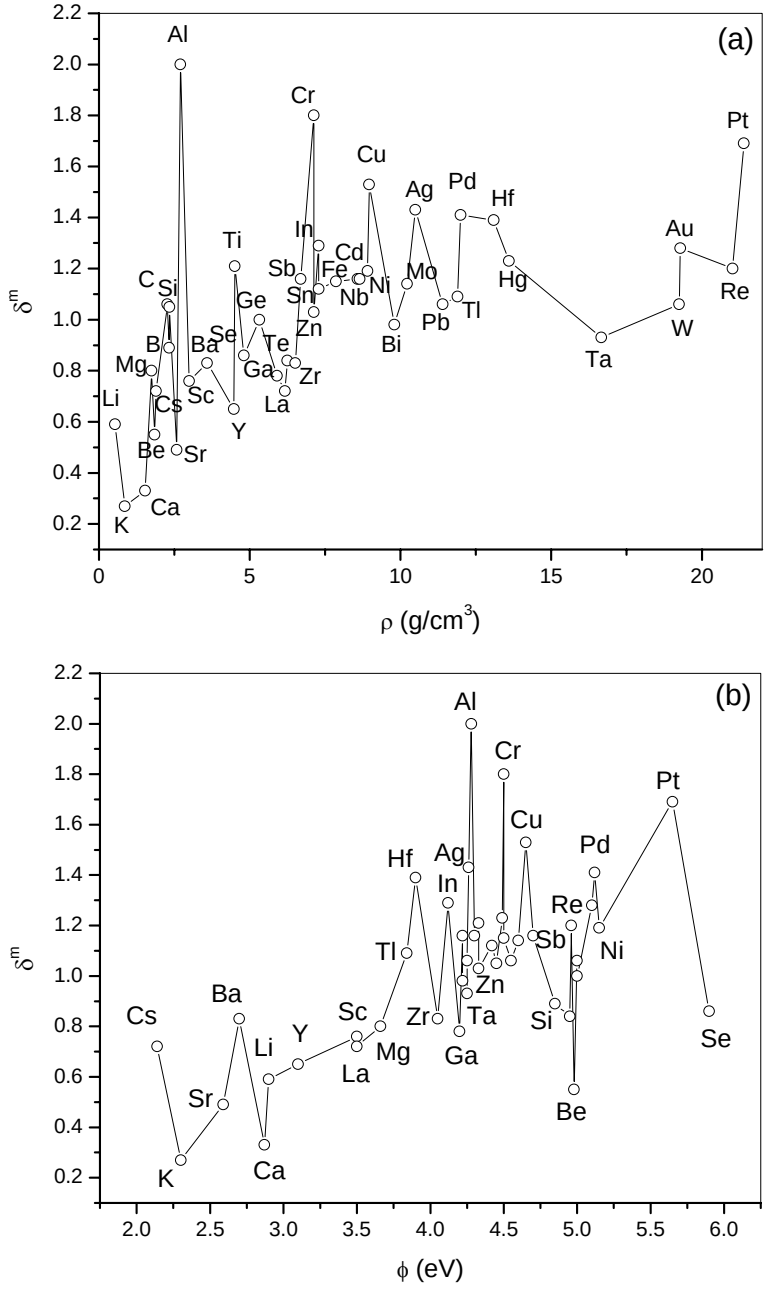

Figure 3-9: Variation of maximum SE yields δ^m with (a) mass density ρ and (b) work function ϕ. There are no simple relations between them.

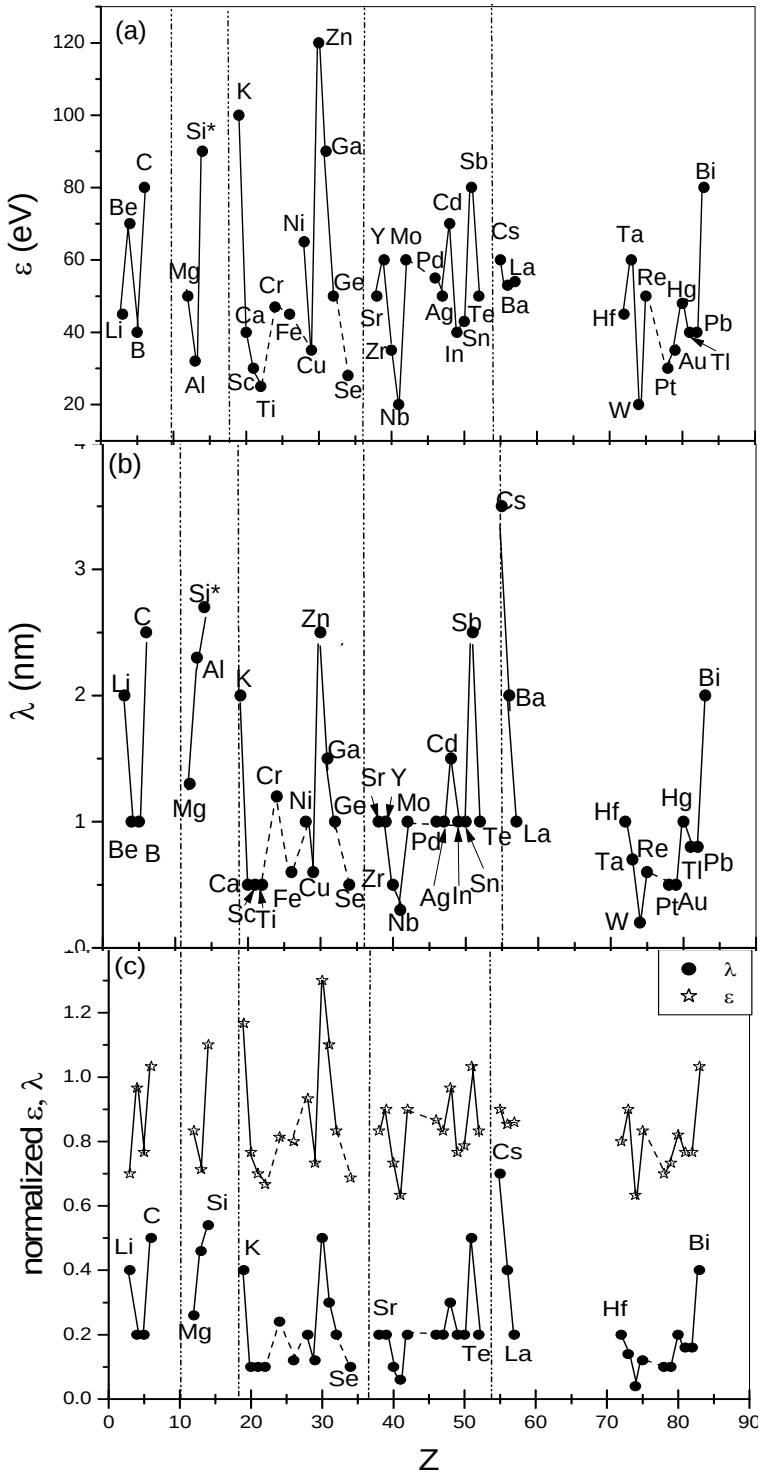

Figure 3-10: SE excitation energy ε (a) and effective escape depth λ (b) as functions of atomic number Z. (c) ε normalized to 150eV and λ normalized to 5nm show extremely similar shape. Solid lines connect neighboring elements, dashed lines connect non-consecutive atomic number. Normalized ε are shifted 0.5 up to make plot clear.

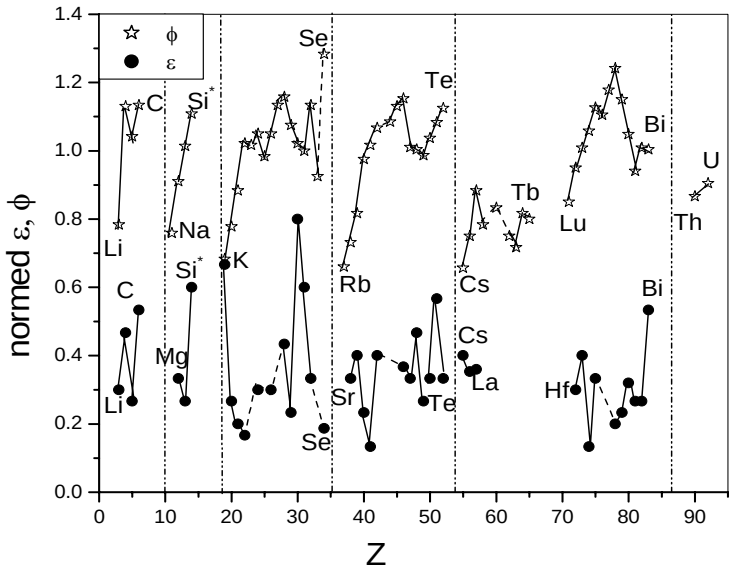

Figure 3-11: Work function ϕ normalized to 6eV and SE excitation energy ε normalized to 150eV as functions of atomic number Z. Normalized work functions are shifted 0.2 up to make plot clear. Solid lines connect consecutive atomic number, dashed lines connect non-consecutive atomic number.

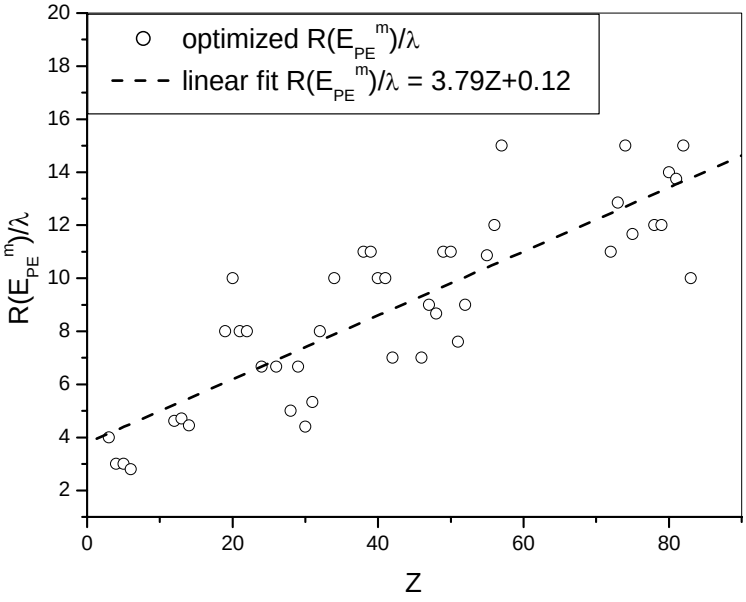

Figure 3-12: The ratios of beam range R at energy E_{PE}^{m} over SE attenuation length λ scatters around the line linearly increase with atomic number Z

database provide an effective method for predicting optimized SE yields and parameters related to the SE emission. Our calculation shows that the maximum SE yield δ^m and the corresponding primary beam energy E_{PE}^m vary with the atomic number Z in the same form as that of mass density ρ, indicating atomic shell filling effect. Simple trends are not found for the complex mean SE excitation energy ε and attenuation length λ. However, because the sequence of Z values is broken in many places and only metal and semi-conductor elements are included in our simulation, it is not possible to confirm this hypothesis, neither is there an obvious physical reason to explain this behavior. Additional experimental results are needed to fill the conspicuous gaps that currently exist in the data. It is also necessary to look at the behavior of the SE yield from compounds to identify the important factors governing electron emission from mixtures of atoms.

4. Chapter Ⅳ: Absolute Spectrum Intensity Calibration of AES

4.1 Introduction

Because of their low kinetic energy and shallow escape depth, secondary electrons are easily affected by sample surface conditions and weak magnetic and electrostatic fields. Historically, the measurement of secondary electron yield is not easy, as indicated by the scattering of the current database [80, 93]. Further, most recent measurements are focused on single elements and a few oxides or complex compounds, rather than systematic studies that cover a range of atomic numbers or carefully graded compositions. This lack of systemic investigation make it difficult to test models of the dependence of electron emission on the sample composition, to predict the SE emission behavior for unknown materials, and to verify the conjectures made in the previous chapter on the physical properties of parameters such as the SE excitation energy ε, mean attenuation length λ, maximum yield δ^m and corresponding primary energy E_{PE}^m. To address this concern it was necessary to design a systematic and accurate method to measure SE yield under uniform and reproducible conditions. It is hoped that this methodology will provide insight into electron-solid interactions. We are particularly interested in establishing the relationship between SE emission and target material composition, especially for binary alloys $A_xB_{(1-x)}$ for which the behavior of each component A and B is well known. To the best of our knowledge, this is the first investigation of its kind.

Historically the SE yield has been measured by the methods as described by Seiler [94] and are illustrated in Figure 4-1.

1. **Retarding Field Analyzer (RFA)** measures the energy distribution of emitted electrons including secondary (SE) and reflected electrons (RE) in all emission directions. RFAs are easy to build, but suffer from large errors resulting from charge build-up on the grid.

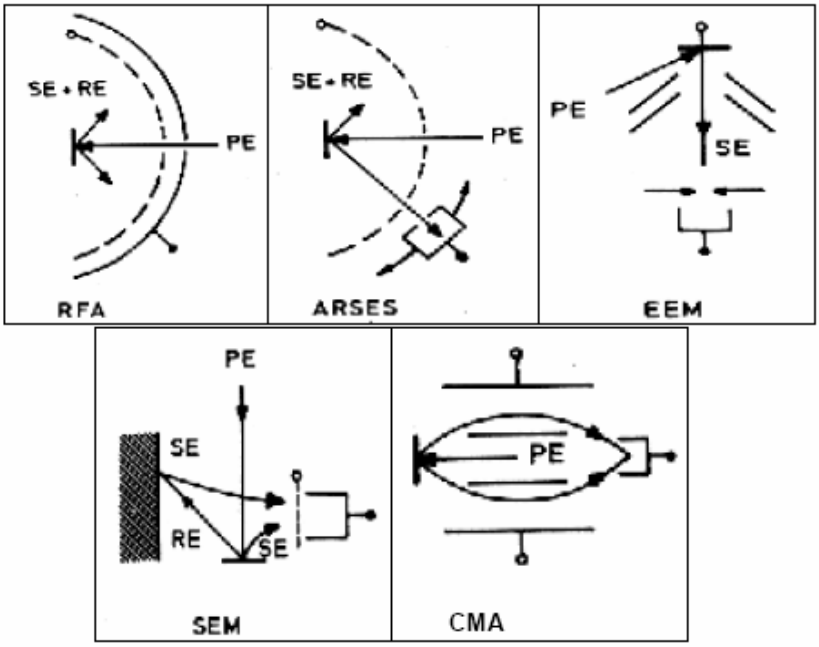

Figure 4-1: Various schematic instrument settings for SE yield measurement. Figures courtesy of Seiler [94].

2. **Angle Resolved-SE-Spectrometer (ARSES)** measures the energy-angle-distribution of SE with a resolving Faraday cup combined with a retarding field. Charge build-up is also a serious problem with this configuration.

3. **Emission Electron Microscope (EEM)** accelerates the SE by an electric field and focuses the SE by a cathode lens. SE is separated from the reflected electrons by using an aperture in the focal plane of the cathode lens. EEMs are rather rare, because they allow only imaging of planer surfaces.

4. **Scanning Electron Microscopy (SEM)** is the most widely available instrument for monitoring and measuring SE. SE yield is achieved by measuring three current: beam current I_b by a Faraday cup, normal specimen current I_{sc} and specimen current I_{scb} when specimen is biased +50V. When there is no bias on the sample the specimen current is the difference between the incident part I_b and the emitted part $I_b(\delta+\eta)$, and

$$I_{sc} = I_b(1-(\delta+\eta)) \tag{4-1}$$

By adding a bias voltage +50 eV all SE with low energies are attracted back to the specimen and add to the specimen current, thus

$$I_{scb} = I_b(1-\eta) \tag{4-2}$$

and SE yield is evaluated as:

$$\delta = (I_{scb} - I_{sc})/I_b \tag{4-3}$$

SE yield evaluated this way is affected by the accuracy of the electron beam current. The bias voltage can attract not only SE (SEI+SEII) generated from the sample, which is the desired part, but also undesired secondary electrons generated from the specimen chamber and pole pieces of the lens by irradiation of high energy BSE, referred as SE3. The second problem is the unavoidable effect of sample surface contamination deposited from residual gasses in the vacuum system. Another possible source of error that is not noticed by most operators is the leakage current. For an SEM equipped with a field emission electron gun, the beam current I_b is usually less than 1 nA. In this case, any material used to insulate the sample from ground under the +50 V bias will induce a high leakage current of the order of I_b as long as its resistance is lower than $5\times10^9\,\Omega$. Experimental data measured when high leakage currents are present can be difficult to interpret.

5. **Cylindrical Mirror Analyzer (CMA)** is the energy analyzer of choice for most Auger electron spectrometers (AES). By sweeping the potential of the cylinder, electrons of specific energy can be separated, counted and recorded to form an energy distribution spectrum as shown in Figure 4-2. SE and BSE yield are determined by measuring their respective areas in the distribution. These yields are normalized to the incident electron count which can be measured by a biased Faraday cup.

Electron energy distributions measured with a CMA are superior to the four methods described above. One advantage of CMA is that it is operated in a field-free chamber preventing disturbance of the trajectory of the SE after its escaping from the sample surface, and thus SEs are collected directly without any suppression or distortion. Another advantage of using an AES equipped with a CMA is that most instruments are operated under UHV conditions ($10^{-7} \sim 10^{-8}$ Pascal) and have in situ argon ion sputtering for cleaning the sample surface. The distinct advantage of using an AES instrument for SE measurements is that surface cleanliness and sample compositions can be directly

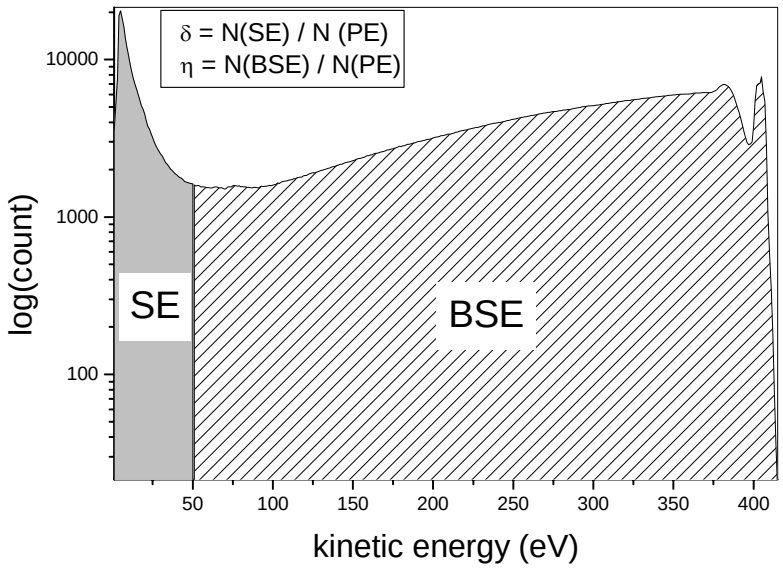

Figure 4-2: Schematic illustration on how to calculate the SE yield δ and BSE yield η from an electron spectrum recorded on a CMA typed AES. The total count of SE, N(SE), and of BSE, N(BSE), are represented by their respective areas on the spectrum. The number of primary electrons is evaluated from the beam current.

determined by analyzing the Auger signals that occur simultaneously when measuring the total electron distribution curve. Finally, the ease of collecting all electrons over a range from 0 to 3200 eV is another benefit of using an AES system for measuring SE emission.

A hidden problem with this method is that detection efficiencies are limited by the transmission of the CMA and modified by the subsequent electron counting systems, forming a function that varies with electron energies and from instrument to instrument. A round robin for AES intensity measurements sponsored by ASTM E-42 committee in 1982 showed that the standard deviation scatter factor for the same Auger peak was as high 356% [95]. This means that quantitative results from different laboratories, using a single database for the AES sensitivity factors, could have an uncertainty of 356% [96-98]. The work carried out by the Japanese VAMAS (Versailles Project on Advanced Materials and Standards) group[99] also showed similar results but with a smaller scattering factor ranging from 1.03 to 1.65. In fact, most AES instruments in service are

still collecting data with uncorrected efficiencies, which makes any quantitative analysis based on the as-received data suspect.

Most of the past and current theoretical work for simulating AES intensities [100, 101] are focused on the high energy part of the spectrum. These efforts are concerned with calibrating the Auger peak height or correcting the inelastic scattering background above 100 eV and almost no effort has been directed toward correcting the spectrum for the secondary electrons with kinetic energies less than 50 eV. In order to obtain the "true" SE spectrum and thus the real yield data, a study on the measurement instrument characteristics must first be performed to identify and quantify sources of efficiency losses. It was our intent to "absolutely" calibrate the PHI 680 scanning Auger nanoprobe (SAN) at the Oak Ridge National Laboratory (ORNL) prior to using it for producing and measuring the "true" electron spectrum for both the SE and BSE.

4.2 Device physics and system integrity of PHI 680 SAN

Most AES systems are composed of three parts: an energy analyzer (such as a cylindrical mirror analyzer (CMA) or a concentric sector analyzer (CSA)), a signal multiplier or detector, such as a micro channel plate (MCP) or channel electron multiplier (CEM), and an electronic circuit to process and record the spectrum. Electrons with various kinetic energies will emit in all directions as a result of e-beam irradiation on the focal point of the energy analyzer. The Physical Electronics Inc. (PHI) model 680 Scanning Auger Nanoprobe (SAN) contains a CMA electron energy analyzer (Figure 4-3) which accepts electrons within a fixed solid angle and specific range of kinetic energies E at each analyzing cycle. Electrons of the specified energy are subsequently multiplied by a MCP and counted by an electronic counting circuit. Since each part, from the CMA through the counting circuit, has its own specific efficiency response to the energy of the electron analyzed, the total efficiency of the PHI 680 SAN system is the product of the CMA transmission efficiency $T(E)$, the MCP detection efficiency $D(E)$ and the transfer efficiency F of the electronic counting circuit. These terms turn the true spectrum $N_0(E)$, which represents the emitted electron energy distribution, into the measured spectrum N(E):

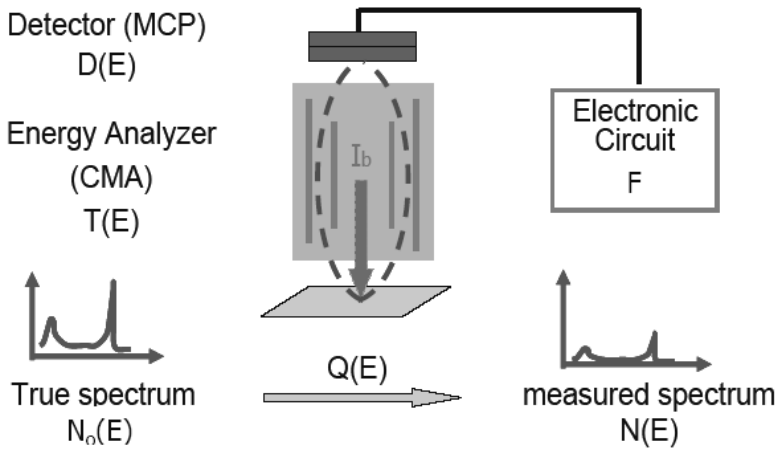

Figure 4-3: Schematic illustration of the signal analyzing and collection system of the PHI 680 SAN. A true electron spectrum $N_0(E)$ turns out to be the measured spectrum N(E) by experiencing intensity loss in CMA with efficiency of T(E), MCP with efficiency of D(E) and electronic circuit with transfer efficiency of F.

$$N(E) = N_0(E) \cdot T(E) \cdot D(E) \cdot F \tag{4-4}$$

if we name a function Q(E) as:

$$Q(E) = T(E) \cdot D(E) \cdot F \tag{4-5}$$

Q(E) is also called the system response function. In the following parts of this section we will discuss the individual efficiencies of the CMA, MCP and the electronic system, and how they are affected by operation parameters and instrument integrity.

4.2.1 Energy analyzer cylindrical mirror analyzer (CMA)

CMA is mainly composed of two cylinders that are coaxial with the electron beam gun (Figure 4-4). The inner cylinder is grounded and has two open slits functioning as the electron acceptance and exit windows. Usually there are meshes made of fine metal wires covered on the energy windows to avoid the field penetration. The outer cylinder is connected to a potential E_p (pass energy) so that in operation, only electrons within a small spread of kinetic energies can be on the right trajectory and find their way through the exit window. Those electrons whose energies are higher or lower will arrive at the inner surface of the outer cylinder or the outer surface of the inner cylinder. Electrons of

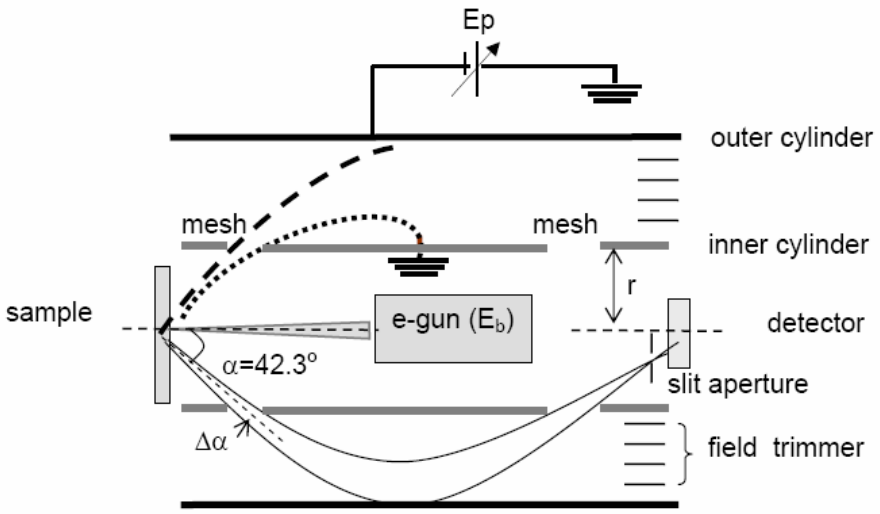

Figure 4-4: Schematic illustration on the mechanism of CMA as energy analyzer.

the energy $E \approx E_p$ thus are separated from the others and are counted in the subsequent devices. By sweeping the potential of the outer cylinder from 0 to a value E_p that is equal to the beam energy E_b, an electron spectrum in the full range from 0 to E_b can be collected. The outer cylinder potential is often swept repeatedly to get good counting statistics, yielding an average count number as the output for most commercial instruments. A ring silt aperture is usually put in front of the detector to improve the energy resolution. The use of field trimmers of different shapes and positions with respect to the exit window at the inner cylinder is an accepted practice in CMA designs to correct for field penetration at the inner cylinder aperture.

4.2.1.1 Accepted energy width ΔE and measured peak FWHM

It has been theoretically and experimentally proved that when the potential of the outer cylinder is set to a certain value in proportion to the CMA geometry, the CMA can form a second order focus [102-104]. This means that, assuming α is the polar angle from the CMA axis, electrons emitted in a wide range of semi angle $\Delta\alpha$ (up to more than 10^o, on both sides of α) around $\alpha = 42.3^o$ can be forced to be focused on the same spot

where the detector is usually located. A CMA can accept a very high solid angle of emission from the sample, giving it a high sensitivity.

It was shown by Seah [104] that the shift ΔL in the distance L between the source and the focusing point is:

$$\Delta L = 5.6r(\Delta E/E) - 15.4(\Delta\alpha)^3 + 10.3r(\Delta E/E)\Delta\alpha \quad (4\text{-}6)$$

where r is the radius of the inner cylinder. Thus for a small $\Delta\alpha$ and a very small ΔL the base energy width ΔE that is accepted is proportional to the electron energy E:

$$\Delta E/E = 5.5(\Delta\alpha)^3 \quad (4\text{-}7)$$

This calculated $\Delta E/E$ is also called the base or theoretical energy resolution $R\%$. It is determined only by the geometry of the entrance window and is a fixed value for each built CMA. Compared to the normal X-ray photoelectron spectrometer (XPS) whose energy analyzer is usually operated in constant ΔE mode, or fixed analyzer transmission (FAT) mode, the constant $\Delta E/E$ mode for normal AES operation is called fixed retard ratio (FRR) or constant retard ratio (CRR) mode. For FRR, the accepted energy width ΔE is proportional to the electron energy E, and the output spectrum intensity of the AES is always noted as $N(E)\cdot E$.

It should be noted that the accepted energy width ΔE is not the peak width (FWHM) of the measured spectrum. From equation (4-6) it is clear that the trajectory of electrons will form an image with classical spherical aberration, and a circle of least confusion will be formed in front of it. The exit slit aperture is usually set in this place for the purpose of improving energy resolution, i.e., making the measured energy width narrower.

The base resolution for the PHI 680 SAN is 0.68% giving the semi angle $\Delta\alpha$ of the acceptance window to be 0.1047 radian or 6 degree. To compare the agreement of the actual FWHM with the theoretical energy resolution $\Delta E = 0.68\%E_b$, the FWHM of the elastic peaks for the $Au_{80}Cu_{20}$ sample were measured. Since the elastic peak is located on the nearly linear background of the direct $N(E)\cdot E$ spectrum and is asymmetrical, it is more precise and reproducible to count the FWHM by hand rather than to fit portion of the peak with a Gaussian or Lorentzian line shape. First, a horizontal line is drawn at a height defined by the energy plateau on the low energy side of the peak shown in Figure

4-5 and is defined as the bottom. Peak height is defined as the distance from that horizontal line to the apex of the peak. This method for measuring FWHM will not have a large error, since neither the linear background nor the tail of a peak will change much in such a narrow energy range.

Table 4-1 and Figure 4-6 show our measurements for $Au_{80}Cu_{20}$ at several primary beam energies. Comparing FWHM to ΔE for the same peak from the PHI 680 SAN shows that, the FWHM is equal to ΔE at electron energies of about 300eV. For higher energies the measured FWHMs are narrower than ΔE, and especially, $FWHM \approx \Delta E/2$ when E is larger than about 1 keV. In the lower energy region, FWHMs are larger than ΔE and have an almost constant value of about 2 eV. Broadening of the elastic peak is a combination of the intrinsic thermal distribution of the e-beam source, the limitation of the ring slit aperture to the electron angular dispersion, and the width of the entrance window $\Delta\alpha$ that determines the theoretical ΔE. The constant large FWHM at low energy range could mean that peak width is determined only by the electron thermal and angular dispersion and the machining tolerance. The slit aperture starts to deduce the peaks when they are wider than about 2.7 eV. It should be noted here that the PHI 680 SAN system is purposely designed to have high sensitivity at the expense of energy resolution.

4.2.1.2 Transmission function T(E)

CMA transmission efficiency is defined as the fraction of the electrons that pass through the CMA. It includes both the constant spatial transmission T and the linearly increased energy acceptance width ΔE, thus is a function of electron energy.

$$T(E) = \Delta E \cdot T \tag{4-8}$$

In some literature, only the spatial transmission T is named as the transmission efficiency. In precise calculations, ΔE should be replaced by the FWHM of the peak formed at each pass energy E_p.

Assuming that the spatial distribution $f(\alpha,\phi)$ for the emitted electron follows a cosine law (α is the polar angle and ϕ is the azimuth angle), T would be the product of the effective fraction of the solid angle $\overline{\Omega}$ subtended by the CMA entrance window,

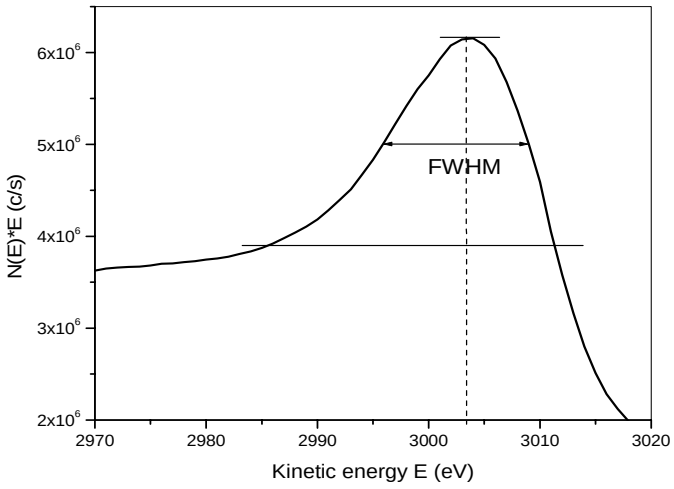

Figure 4-5: An illustration on how to measure the FWHM of an elastic peak on a direct AES spectrum collected on the PHI 680.

Table 4-1: A list of the measured FWHM of the elastic peak for $Au_{80}Cu_{20}$ on the PHI 680 SAN and the designed accepted energy width $\Delta E = 0.68\% E_b$ under various beam energies

Eb(keV)	*3*	*2.5*	*2*	*1.5*	*1*	*0.8*	*0.7*	*0.6*	*0.5*	*0.4*	*0.3*	*0.25*	*0.2*	*0.15*	*0.11*
FWHM(eV)	13	10.7	8.4	6.3	4.7	4.1	3.9	3.7	3.4	3.0	2.7	2.3	2.3	2.1	1.9
ΔE (eV)	25.8	21.5	17.2	12.9	8.6	6.9	6.0	5.2	4.3	3.4	2.6	2.2	1.7	1.3	0.95

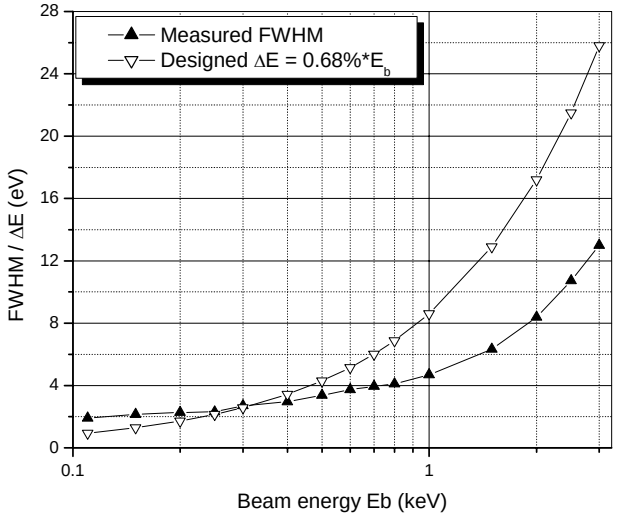

Figure 4-6: A plot of the data in Table 4-1. The measurement equals to ΔE at energy of about 300eV; FWHM are lower than ΔE at higher electron energies and are higher at lower energies.

and the optical transparency W of the entrance and exit windows that are usually covered with meshes and blocked by supporting bars.

$$T = W \cdot \overline{\Omega} \tag{4-9}$$

$W \approx 0.6885$ for a Varian CMA according to Seah and Hunt [105], and

$$\overline{\Omega} = \frac{\int_{\Omega} f(\alpha,\phi)d\Omega}{\int_{2\pi} f(\alpha,\phi)d\Omega}$$

$$= \frac{\int_0^{2\pi} d\phi \int_{42.3-\Delta\alpha}^{42.3+\Delta\alpha} I_0 \cos(\alpha)\sin(\alpha)d\alpha}{\int_0^{2\pi} d\phi \int_0^{\pi/2} I_0 \cos(\alpha)\sin(\alpha)d\alpha}$$

$$\approx 2\Delta\alpha \sin(84.6^o) = 1.99\Delta\alpha \tag{4-10}$$

Assuming $\Delta\alpha = 6^o$, spatial transmission T for the PHI 680 SAN is 14.3%. Assuming $FWHM \approx \Delta E = 0.68\%E$ then $T(E) = 9.75\times10^{-4}E$. In such a condition, $T(E)$ increases from about 0.1% at $E = 1eV$ to about 1 at $E = 1keV$ by broadening of the energy width. Only when the peak area is counted $T(E)$ increases linearly with electron energy.

4.2.1.3 Sample position sensitivity

Since a CMA collects electrons at $\alpha = 42.3^o \pm \Delta\alpha$, it is important to locate the sample at the origin of the coordinate system, otherwise the electrons entering the electrostatic field between the two cylinders will not have correct trajectories for passing through the exit window and to the correct focus. For this reason the CMA has a focus volume of limited dimensions for the electron signal to be analyzed with tolerable error. Deviation of the sample away from the CMA focus volume will cause serious spectral distortion, including peak position shifts and the reduction of peak intensity. In the following we will discuss the sensitivity of the CMA only in the axial or z direction, with positive z pointing to the CMA. Correspondingly the directions normal to z are called x and y direction.

The PHI 680 SAN has its own built-in standard process called “z-alignment” in the instrument control software package (called “PC-Access”) to help locate the sample to the proper axial position. In this process the spectrum of the 1000 eV elastic peak is

dynamically monitored so that the operator can make small adjustments on the sample position to maximize the peak intensity. For the PHI 680 system the elastic peaks are the most intense when their output energy are brought to 1004 eV. The extra 4 eV is added by assuming that the samples have constant work function of about 4 eV, so that the output electron kinetic energies are referred to the Fermi energies of the samples. In the discussions below the sample deviation Δz will be referred to the arbitrary standard position calibrated by this "z-alignment".

Table 4-2 lists the data collected on the PHI 680 SAN and demonstrates the effect of sample position shift Δz on the energy deviation ΔE of the observed energies from the arbitrary values, and the corresponding maximum spectrum intensity I for the 300 eV, 750 eV, 1500 eV, 3000 eV elastic peak, and two other Auger peaks: Cu MVV at 64eV and LMM at 920 eV.

Figure 4-7 plots the energy shift and spectrum intensity reduction for 750, 1500 and 3000 eV peaks. It is obvious that the measured peak energy increases linearly with the decrease of z (Δz change from negative to positive) and with different slopes for different peaks (Figure 4-7 (a)). At around the CMA focus position the peak intensities I_{peak} have the highest values; deviations of sample positions on both sides cause asymmetrical reductions of intensities. From Figure 4-7 (b) we can see that the maxima of the peak intensities for different energies do not correspond to the same sample position, caused by the relativistic effect [106] due to the velocity and the spread of the incident angle to the CMA [107]. The discrepancy of the focus position between the 750eV peak and 3000eV peaks is ~1mm. A positional variation of this value will cause an energy shift as big as 10eV for peaks around 1500eV (Table 4-2), an energy range often used in AES analysis. Since no effort has been made to correct this relativity effect, the 1000 eV elastic peak will be used to calibrate the sample position because peaks of this energy usually have relatively high signal-to-noise ratio and are close to the range of SE.

The relative peak shift to sample position, $\Delta E/\Delta z$, has a constant slope with respect to peak energy E. According to equation (4-6)

Table 4-2: Variation of the energy shift ΔE and normalized peak height I with deviations of sample position a distance ΔZ away from the CMA focus in PHI 680 SAN for elastic peaks with various energies. Iis normalized to the maximum values in the series peak heights for the same energy.

ΔZ	E = 300 eV		E = 750 eV		E = 1500 eV		E = 3000 eV	
(mm)	ΔE (eV)	I	ΔE (eV)	I	ΔE (eV)	I	ΔE (eV)	I
-2	-3.5	0.83	-10	0.9	-20	0.81	-38	0.77
-1.8	-3	0.88	-9	0.92	-18	0.84	-35	0.79
-1.6	-2.5	0.88	-8	0.93	-16	0.87	-31	0.81
-1.4	-2.5	0.92	-7	0.94	-14	0.87	-27	0.84
-1.2	-2	0.96	-6	0.95	-12	0.9	-23	0.86
-1	-1.5	0.95	-5	0.97	-10	0.92	-19	0.88
-0.8	-1.5	0.96	-4	0.98	-8	0.93	-15	0.9
-0.6	-1	1	-3	1	-6	0.96	-12	0.93
-0.4	-0.5	0.98	-2	1	-4	0.97	-8	0.95
-0.2	-0.5	0.96	-1	1	-2	1	-4	0.98
0	0	0.98	0	0.98	0	1	0	0.99
0.2	0.5	0.97	1	0.97	2	0.99	3	1
0.4	1	0.95	2	0.95	3	0.98	7	1
0.6	1	0.95	3	0.95	5	0.98	11	0.99
0.8	1.5	0.94	3	0.95	7	0.97	14	0.99
1	2	0.91	5	0.91	9	0.96	18	0.98
1.2	2	0.9	6	0.89	11	0.94	22	0.97
1.4	2.5	0.89	7	0.87	13	0.93	26	0.97
1.6	3	0.88	8	0.84	15	0.92	29	0.96
1.8	3.5	0.85	9	0.83	17	0.9	34	0.94

Tables 4-2 continue: for Cu MVV 64 eV and LMM 920 eV

ΔZ	E = 64 eV		E = 920 eV	
(mm)	ΔE (eV)	I	ΔE (eV)	I
-3	-1	1.14	-17	0.94
-2.4	-1	1.09	-14	0.94
-1.8	-1	0.97	-10	0.91
-1.2	-1	0.99	-7	0.94
-0.6	-1	1	-3	0.96
0	0	1	0	0.98
0.6	0	0.98	3	0.98
1.2	0	0.97	7	0.99
1.8	0	0.95	10	0.99
2.4	0	0.95	13	1
3	1	0.89	17	0.99

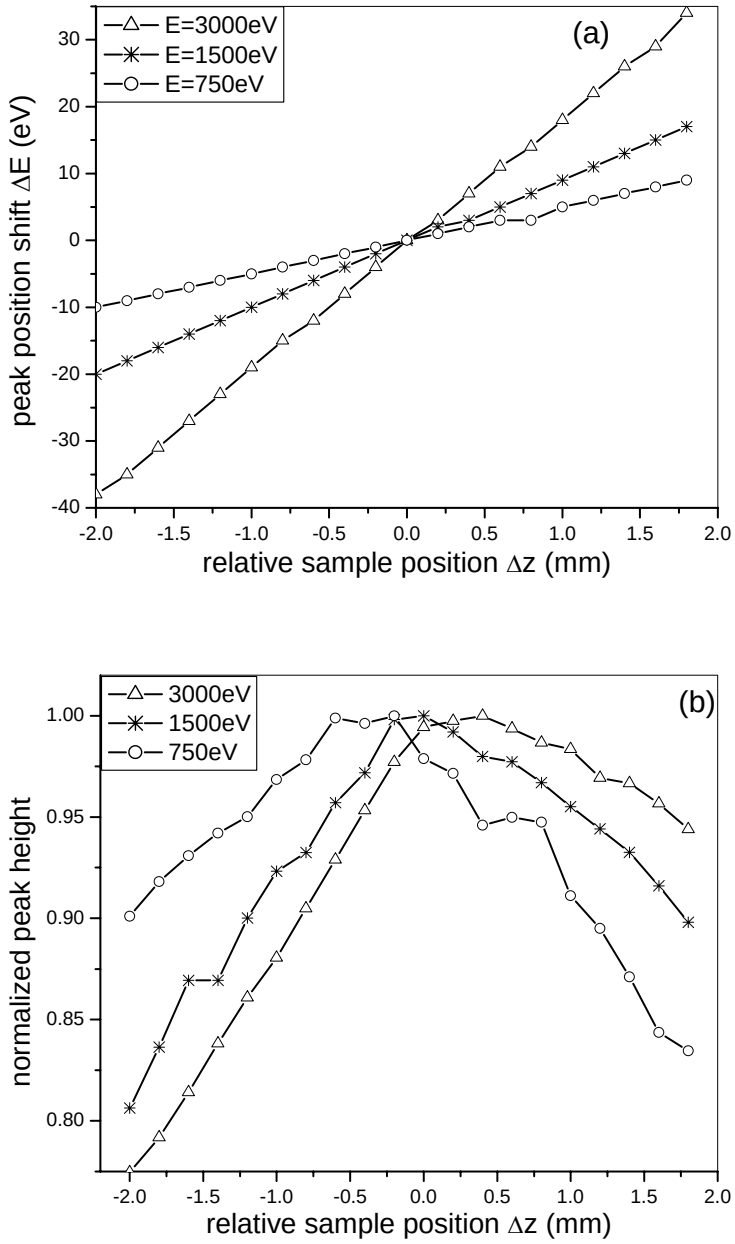

Figure 4-7: Deviation of sample position from CMA focus point in the axis direction in PHI 680 SAN cause spectrum distortion. Legends note the energy of the electrons forming the peak. The sample position is relative to the one calibrated with the 1000 eV elastic peak, (a) Peak position shift ΔE with sample position Δz. (b) Peak intensity reduction with Δz. Noted that electrons with different energies show different CMA focus positions.

$$\frac{\Delta E}{\Delta z} = \frac{1}{5.6r} E \tag{4-11}$$

so the value of the slope is determined by the radius of the inner cylinder. Following the definition of Sickafus and Holloway [108], we call the reverse of the slope the CMA energy dispersion constant D, and

$$D \frac{E}{\Delta E / \Delta z} = 5.6r \tag{4-12}$$

D for the PHI 680 has an average value around 143.81mm for energies ranging from 60eV to 3000eV (Table 4-3).

A linear fit shows that the slope of $\Delta E/\Delta z$ with respect to E is $0.0063\,E$ (Figure 4-8), which means that the sample would need to be located within ± 0.12mm around the CMA focal point in the axial direction to limit the error of peak position within $\pm 2\%$. The reliability of the process for aligning the sample by locating the 1keV peak maximum at 1004eV is called into question by these results. For a resolution of R=0.68%, the width for the 1keV peak would be 6.2eV. To locate a sample within ± 0.12mm, a peak shift of only ± 0.72eV would be allowed. It is extremely difficult to locate a peak maximum within such a narrow range when the peak is broad and asymmetrical. Locating the cross point of a differentiated peak at the incident beam energy would be a more accurate mode and has been applied in some cases [95], however, this mode is not available on the PHI 680 SAN.

The roughness of the sample surface increases the difficulty of sample alignment. In the standard z-alignment process the PHI 680 SAN applies electron beam (with diameter of tens of nanometers) on one position of the sample. A limitation of ± 0.12mm requires that the sample surface be extremely smooth and flat. This is difficult for most "real world" samples routinely analyzed using AES. Even polished samples can be roughened when Ar-ion sputtering is used to clean surface contamination or for depth profiling. In a preliminary experiment, we observed that Ar ion sputtering on pure gold for 4 minutes with a beam energy of 3.5 keV and beam current of 3 mA sputtering over an area of $0.5 \times 0.5 mm^2$ produced two optimum sample positions that varied by 0.2 mm using the

Table 4-3: CMA sensitivity factor D for PHI 680 SAN.

E(eV)	*ΔE/Δz(eV/mm)*	*D= E/(ΔE/Δz) (mm)*	*Average D (mm)*
3000	18.835	159.278	
1500	9.639	155.618	
920	5.636	163.236	143.810
750	4.966	151.027	
300	1.769	169.587	
63	0.303	207.921	

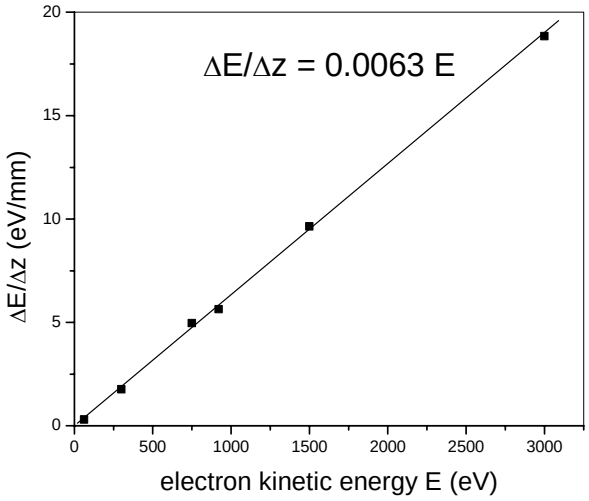

Figure 4-8: Peak shifting velocities $\Delta E/\Delta z$ linearly increase with electron energies E .

standard sample alignment procedure.

To align real-world samples with imperfect surfaces, two methods were attempted--The first one was to apply a reference surface by attaching a smooth silicon wafer to the sample, locating the proper focus point using the Z-align process on the perfect silicon wafer, then moving the sample of interest under the electron beam and adjusting the Z position by making the image as sharp as possible. This did not prove to be a good method, since the sharpness of the image does not change greatly within $z = \pm 0.12$mm for the large depth of focus of the field emission e-beam. The second method used was to acquire a survey spectrum on a large area, approximately $50 \times 50 \mu m^2$. A scanning area of $250 \times 250 \mu m^2$ has been widely applied in the literature in order to average over many grains and hence eliminate angular anisotropy effect [95-98, 109, 110], but collection of electrons much away from the CMA axis may cause insufficient signal collection efficiency according to Geller [111]. In our experiments, abnormal high background was found on spectra collected on an area of this size, which we thought to be caused by internal scattering in the CMA. For this reason, a scanning area of $50 \times 50 \mu m^2$ is applied in our experiments for both sample alignment and spectrum collection, and been proven to produce stable results.

4.2.1.4 Internal scattering effect

Internal scattering refers to the scattering of electrons from various positions inside the CMA analyzer generating an unwanted contribution to the spectral background in an AES experiment. It is suggested by Gomati and Bakush [112, 113] that the exit slit aperture and the field trimmer (Figure 4-4) are the main sources of scattering electrons. According to them, scattering from the field trimmer may contribute 18~20%, while the one from the exit aperture may contribute 5~6% of the total collected electron counts in a single-pass Varian CMA. Scattering from the exit slit aperture happens when electrons with non-optimized energies and trajectories hit the surface of the aperture and liberate SE. The larger part of scattering comes when high energy electrons hit the field trimmers and generate SE. These generated SEs then may be sucked in the detector and add to the

signal background. Contrary to what we first thought, secondary electrons generated on the inner wall of the outer cylinder by the irradiation of high energy electrons is not a significant contribution since most of the SE are blocked by the slit aperture.

Attempts to correct the internal scattering by subtraction of a background which is assumed [114] to be either constant or proportional to the electron energy has been made by Yoshitake and Yoshinara [115]. They found that the field trimmer may not produce as much scattering as predicted by Gomati and Bakush [113]. Because of the uncertainty of this background subtraction method, internal scattering is not treated in our later calculations.

4.2.2 Electron detector microchannel plate (MCP)

The negatively charged electrons passing through the CMA will hit on a detector, a device comprised of a single or multiple channels which also functions as a signal amplifier. The channels are made from glass or ceramic with a low conductivity surface layer possessing a high secondary electron emission coefficient. By adding a high voltage across the channels, the secondary electrons generated by the initial irradiation of the incoming particles can be accelerated. This process of electron generation and acceleration is repeated several times, producing more and mote SEs. One incident electron can produce $10^4 \sim 10^8$ electrons at the output of the detector (Figure 4-9). The signal magnification power of the detector is called the gain. This type of detector can amplify very weak signal sources and can be used to detect a wide range of particles including protons, ultra violet photons, and very low energy X-rays.

Depending on the number of channels, electron multipliers are classified in two types: single or multi-channel electron multipliers. The structure of a typical single channel electron multiplier (CEM) consists of a horn with a cone semi-angle in the range of 20-45^o for increased collection efficiency connected to a 1~2.5 mm diameter channel. Multi-channel electron multipliers are typically configured as an array of small glass channel forming a micro-channel plate (MCP). The channels are typically 10~12 um in diameters and 40:1 in length to diameter ratio. The PHI 680 SAN uses a chevron style MCP that is composed of two MCPs held back-to-back. The channels in the two plates are orientated

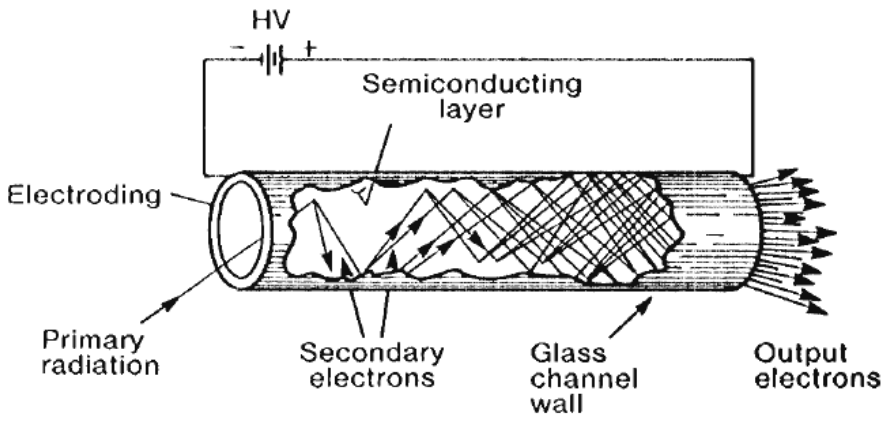

Figure 4-9: Schematic illustration on the principle of signal magnification for a channel on a single or multi channel electron multiplier.

Figure by courtesy of Wiza [116].

with an angle of around 10^{o} to prevent positive ions produced at the output of the rear plate from reaching the input of the front plate and producing extra SE ---- a phenomenon called ion feed back [116]. MCPs are used in other applications than electron detectors and are commonly found in various night vision goggles and scopes for imaging due to their high spatial resolution.

When used as a signal multiplier, CEM or MCP are operated in either analogue or pulse counting mode. In pulse counting mode the electron multipliers operate in a space charge saturation condition. This means that near the channel output, at high gains ($\sim 10^{8}$), the space charge density electrostatic repulsion reduces the kinetic energy of the electrons that hit the channel walls, producing less secondary electrons. In turn, less secondary electron at the rear of the channel decreases the space charge allowing the electrons to produce more secondaries and set up a dynamic equilibrium. When operated under dynamic space charge saturation conditions, pulse counting MCPs produce pulse with characteristic amplitude in contrast to analogue MCPs which have a wide distribution of output pulse amplitudes. The high, saturated gain of pulse counting multipliers allow one to set a discriminator level to reject low-level noise, resulting in improved signal-to-noise performance. In pulse counting mode, each incident electron is amplified to produce an output pulse which is processed by the electronic counting system. In analogue mode, the

multiplier works only as a current amplifier with a gain of 10^3~10^4. The amplified current is usually detected by a current-to-frequency converter or some form of analogue amplifiers.

It should be noted that MCPs are intrinsically fast detectors and have very high temporal resolution. The pulse transit time through the intense electric field is of order 10^{-10} seconds [117], meaning that as long as the input count is no higher than 10^{10} count per second, the MCP counting process will not be disturbed. The incident beam current in an AES system equipped with a field emission gun is on the order of nano-amperes, or 10^{10} in electron counts per second. Since the maximum transmission efficiency is about 1 as deduced in section 4.2.1.2, and the Auger electron yield is much less than 1, the MCP input count rate will be less than 10^{10}, making it feasible for MCP to work in pulse counting mode by counting electrons one at a time.

4.2.2.1 MCP detection efficiency D(E)

A MCP multiplies electron signal through many steps of a cascading SE emission process. Most generated SEs have kinetic energies of 5~10 eV produced by a uniform electric field gradient E from the multiplier voltage V applied across the channel. These 5~10 eV SEs will ultimately be accelerated to about 200 eV generating further SEs with almost the same yield δ in each step. The yield δ_1 for the first step though, depends on the energies of the electrons coming out of CMA. Therefore, total multiplication G of the MCP varies with electron energy following the "SE yield universal law" [118].

$$G = \delta_1 \delta^m \tag{4-13}$$

where m is the step number. For $m = 25$ which is a reasonable number and $\delta = 2$, G is $10^7 \sim 10^8$ and follows the profile of δ_1.

For analogue mode, since the product of the number of incident electrons and the total gain G is directly detected, the MCP detection efficiency $D(E)$ has exactly the same shape as $\delta_1(E)$. In pulsing counting mode, the emission of secondary electrons has a Poisson probability distribution for each single stage of multiplication. At each stage of multiplication, there is a probability that the cascade will die. This probability rapidly

reduces as the multiplication develops down the channel. All events that are not lost are then sufficiently amplified and counted as an event. The efficiency $D(E)$ is a calculated statistic result and has a shape similar to the SE yield universal curve but with a flatter peak [118].

4.2.2.2 Multiplier voltage V effect

The chevron-type MCP in the PHI 680 SAN works in pulse counting mode operated under space charge saturation. The produced pulses should have almost the same amplitude, so that by properly setting the discriminator noise with low amplitude can be rejected.

Figure 4-10 is a measurement on the effect of the multiplier voltage V on the detection efficiency of the MCP in the PHI 680. The measurement was taken by recording the normal electron spectra and determining the counts at energy points ranging from 3 eV to 3000 eV at various multiplier voltages. Intensities of the spectra are normalized to the maximum values measured under specific energies, which was for the highest allowable multiplier voltage (2400 V for the PHI 680 SAN). By removing the intrinsic spectral intensity variation with electron energy, the normalized intensity can be defined as the MCP detection efficiency, assuming the efficiency under V =2400 V is 100%.

Figure 4-10 (a) shows the improvement of detection efficiency with increasing multiplier voltage$V$. Below V =1900 V, the detection efficiency is almost zero but increases rapidly above that voltage. Electrons with higher kinetic energies start to respond to multiplier voltage at lower V but increase less rapidly. However, we do not observe a plateau on the high V end as predicted by Seah et al [119] in any case, meaning that either the multiplier can be operated with higher gain or the pulse counting MCP in PHI 680 is not working under space charge saturation. This implies that the efficiency at V =2400 V is actually less than 1 and all other actual efficiencies are lower than what is noted on Figure 4-10, because part of the signal is rejected by the discriminator.

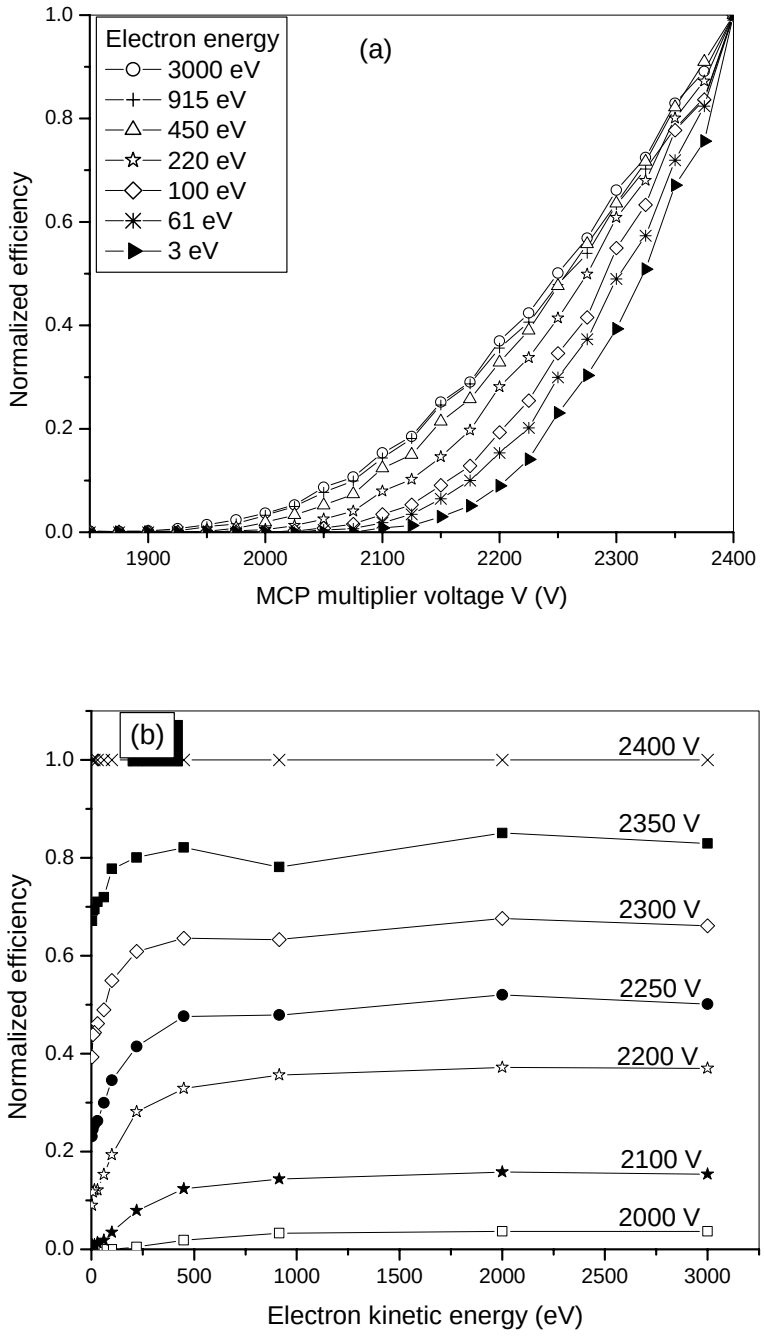

Figure 4-10: Responses of the detection efficiency for MCP in PHI 680 SAN to the multiplier voltage V and the electron energy. (a) Detection efficiency as a function of multiplier voltage V. The increasing tendency at high V indicates that the MCP is operated below saturation point. (b) Detection efficiency as a function of electron kinetic energy increase with multiplier voltage.

Figure 4-10 (b) shows the non uniformity of the detection efficiency for electrons of various energies and how an increase in the voltage can improve detection efficiency, especially for low energy electrons. Under the recommended voltage of 2100 V, the detection efficiency for SEs with energies smaller than 50 eV is lower than 2%, while for BSE the efficiency is 5 times higher, up to 10%. By increasing the multiplier voltage to 2300 V, the difference decreases to about 1.5 since the efficiency for BSE is increased to 60%, and the SE efficiency is increased to 40%. Unfortunately on the PHI 680 SAN there is no way to adjust the discriminator setting to make the MCP detection efficiency more uniform. 2300 V was chosen as the multiplier voltage for the measurement discussed in this work, since it optimizes the MCP efficiency. For some measurements, 2100 V will be used for comparison.

Figure 4-11 is an illustration of the enhancement that is observed when the multiplier voltage increases from 2100 V to 2300 V. The peak at 2~5 eV is much more prominent. Spectral intensity on the low energy end increases more than the high energy end.

4.2.2.3 MCP dark noise

The MCP on the PHI 680 SAN has dark count noise around 500 counts per second in the 1000~3000 eV energy range even when the incident beam is blanked and no electrons are arriving at the detector (Figure 4-12). This phenomenon is caused by the secondary emission on the two focusing electrodes in front of the MCP [120]. The dark count could be reduced 40 times when both of the electrodes are grounded, but is not allowed by the proper operation of the MCP in this configuration. This part of noise count should be subtracted when determining the absolute spectral intensity. The data sheet for Figure 4-12 is given in Table A-1 in Appendix 1.

4.2.3 Transfer efficiency F of the electronic system – dead time τ

For a MCP at high output count rate when working under space charge saturation, proper setting of the multiplier voltage and proper discriminator threshold, the theoretical output count rate N at a specific energy point should have a linear relationship with the input signal intensity. (Note that the input signal should be proportional to the beam

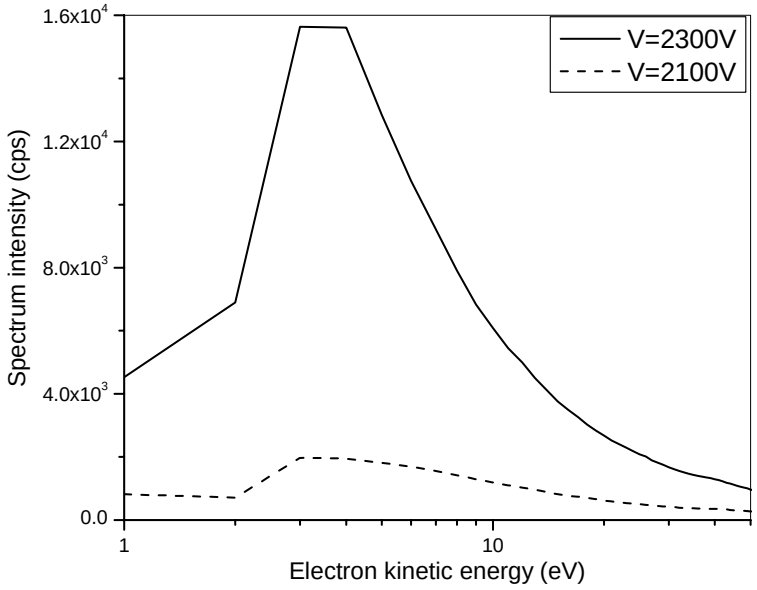

Figure 4-11: Comparison of a SE spectrum under 2300 V and 2100 V MCP voltage shows that increasing the multiplier voltage produces a much higher output count rate for weak electron signal in PHI 680.

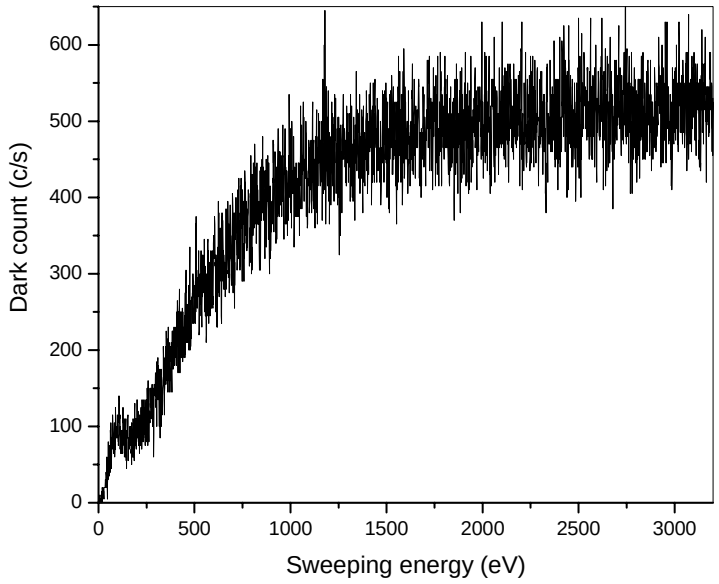

Figure 4-12: Dark count spectrum collected on PHI 680 with electron beam blanked.

current I_b). In real situations, the dead time τ in the subsequent electronic counting system causes the actual output rate N' to be less than N, thus the electronic system has a dead time induced transfer efficiency F. Figure 4-13 (a) shows how the intensities for three different peaks deviate from a linear relationship with beam current I_b. The figure also illustrates that when the MCP multiplier voltage is increased from 2.1 kV to 2.3 kV the deviation starts at higher output count rate in PHI 680 SAN.

Dead time τ is a specific characteristic of each electronic counting system. During the dead time the system is busy shaping the received pulse, and any further events are not recognized. If the system detects pulses on a non-extended basis [121, 122], for a measured count rate of $N'(s^{-1})$, the total dead time per second will be $N'\tau$ and the true count rate N is given by the N' counts occurring in $1-N'\tau$ seconds. Thus [118, 122]

$$N = \frac{N'}{1-N'\tau} \tag{4-14}$$

and

$$\frac{N'}{N} = 1-N'\tau \tag{4-15}$$

Since the true count rate N is proportional to beam current I_b, by assuming a constant C gives $N = CI_b$, we have

$$\frac{N'}{I_b} = A-(A\tau)N' \tag{4-16}$$

If the linear relationship of N'/I_b with N' is drawn as in Figure 4-13 (b), system dead time τ would be the absolute slope of the line divided by its interception with the axis of N'/I_b. The expressions for the linear fit of the datasets are listed in Table 4-4. The evaluation for the dead time shows that in the current instrument, the dead time τ varies with the setting of the MCP voltage V. $\tau \approx 35ns$ for $V = 2.3kV$ and $\tau \approx 110ns$ for $V = 2.1kV$. $\tau \approx 110ns$ is reasonable given that it is based on measurements on a wider energy range. The larger dead time for lower multiplier voltage also explains why the peak intensities deviate from linear earlier. To limit the measurement error caused by the

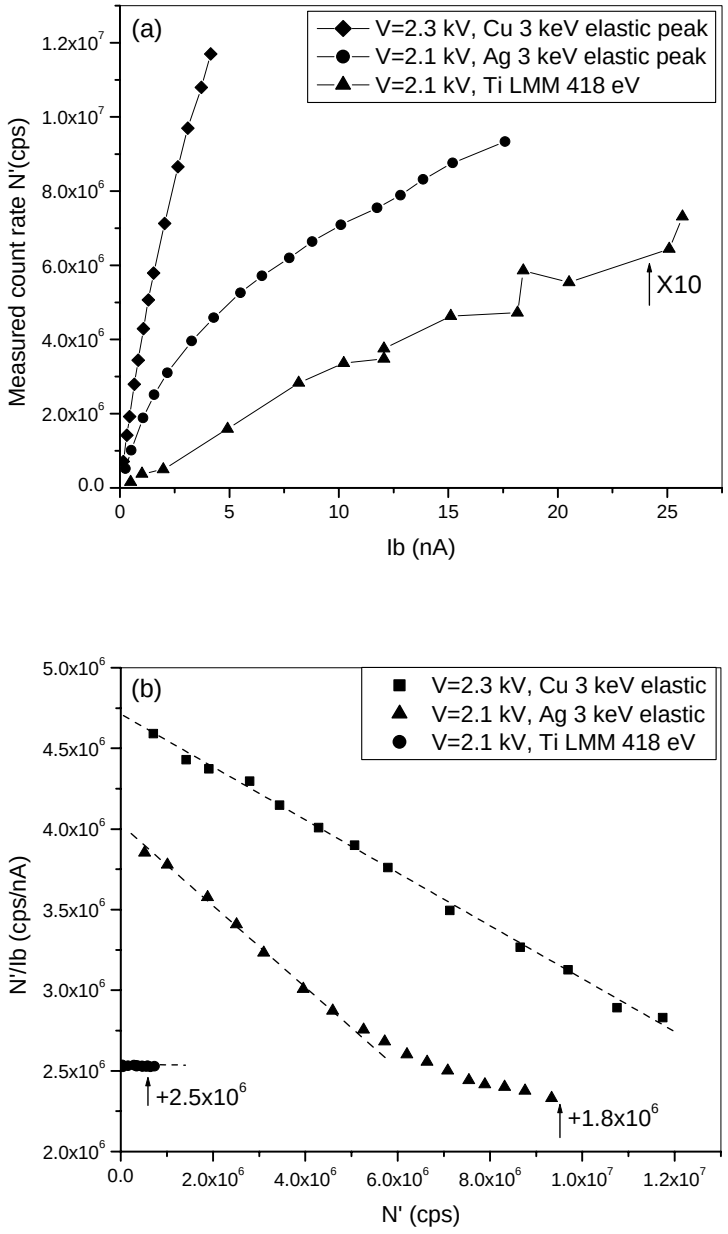

Figure 4-13: Non-linearity of the signal intensity in PHI 680 SAN caused by dead time of the electronic counting system and the MCP saturation. Some data sets are modified to be fitted into one graph (a) Measured output count rate N' for 3 peaks at 2 multiplier voltages V deviate from the linear relationship at high beam current I_b end. (b) Expression of the same sets of data in the form of $N'/I_b \sim N'$. Dead time can be evaluated from the linear fit of the data points. The off-linearity of the V =2.1 kV, Ag 3keV peak could be caused by the ion feed back in MCP.

Table 4-4: Linear fit for the three datasets N'/I_b as a function of N' in Figure 4-13 (b) and the evaluation of dead time for the electronic counting system.

Peak	*MCP voltage V(kV)*	*Linear fit parameters*		*Dead time τ (ns)*
		slope	interception	*=-slope/interception*
Cu 3keV elastic	2.3	-0.1638	4.70×10^6	34.8
Ag 3keV elastic	2.1	-0.2436	2.20×10^6	110.7
Ti LMM 418 eV	2.1	-0.0065	3.23×10^4	201.2

dead time within 2%, say for $\tau \approx 35ns$, the input count rate should not be higher than about 3×10^6 count per second. Signal non-linearity caused by dead time effects can be corrected after measurement according to equation (4-14) or (4-15). N'/I_b at $V = 2.1kV$ for the Ag 3 keV elastic peak is still not linear at the high end as shown in Figure 4-13 (b), indicating the existence of effects other than the dead time. Seah [121] explained the non-linearity in this relationship as the saturation of MCP, a phenomenon that happens when the high output count starts to deplete the wall current of the channels, resulting in N'/I_b decreasing below the fitted line. The upward bend of N'/I_b for the Ag peak is obviously not caused by the MCP saturation. The actual increase of the measured signal intensity N' could be caused by ion feed back. To limit the possible error caused by this effect, in further measurement, we limited the maximum output count rate to within 2×10^6 counts per second for $V = 2.1kV$ and 1.2×10^7 counts per second for $V = 2.3kV$, according to Figure 4-13 (b).

4.2.4 A summary on the optimized operation parameters

For the convenience of further reference, the optimized operation parameters for the PHI 680 SAN are summarized in Table 4-5.

4.3 Calibrate the spectrum intensity

4.3.1 Calibration methodology

Determining the absolute intensity of an AES spectrum is essential not only for SE

Table 4-5: A summary on the optimized operation parameters for PHI 680 SAN.

Device	*Parameter*	*Value/method*	
CMA	Energy acceptance width	Elastic FWHM ≠ ΔE (0.68%E)	
	Focus volume $(x \cdot y \cdot z)^3$ mm^3	$0.05 \times 0.05 \times (\pm 0.12)$	
	Energy dispersion rate D=E/(ΔE/Δz) (mm)	143	
	Sample alignment method	Locate 1 keV elastic peak on 1004 eV by scanning beam on an area of 0.05×0.05mm2 other than spot mode automatic alignment	
MCP	Multiplier voltage (kV)	2.3	2.1
	Allowed max count (c/s)	1.2×10^7	2×10^6
Counting circuit	Dead time (ns)	34	100~200

yield measurements and quantitative chemical analysis, but also for testing models of the electron-solid interactions. There are six AES databases currently available. The 4 commonly used ones [123-126] list spectra only for the interested energy ranges and are mostly in differential form to facilitate chemical identification and traditional quantitative analysis. Comparisons of these databases show a relative scatter of the spectral intensities as high as 1.5 [127]. For these 4 databases, none of the intensity-energy responses for their data collecting instruments are known. Two other databases provided by National Physical Lab (NPL) [128] in the United Kingdom and Surface Analysis Society of Japan (SASJ) have removed the effect of instrument efficiency loss, but the former has limited energy range (20~2500 eV) and is only available for beam energies of 5 and 10 keV; while the latter is only available for limited materials. For these reasons, to obtain a systematic AES spectrum in full energy range, and for a variety of beam energies and atomic numbers, including alloys of complex compositions, we need to obtain absolute AES spectra by calibrating the intensity-energy response of the PHI 680 SAN.

To calibrate the spectrum intensity, we need to reverse the data collection sequence, correcting first the dead time effect F of the electronic counting system, then the multiplier detection efficiency $D(E)$, and finally the CMA transmission efficiency $T(E)$. As discussed in section 4.2 we know that calculating or measuring efficiencies of the CMA and MCP on the PHI 680 SAN system is not easy, since both parts are not operated in their predicted conditions. Theoretically any spectrum intensity $N(E)$ can be

expressed as the product of the incident beam current I_b, the characteristic instrument response $Q(E)$, and the secondary yield $n(E)$, which is determined by the physical signal generation mechanism as a function of electron kinetic energy E,

$$N(E) = I_b \cdot n(E) \cdot Q(E) \tag{4-17}$$

If a spectrum $N(E)$ exists for which the response function is precisely known, then it can be used as a reference for calculating $Q(E)$ of any other instrument of interest by comparing spectra of the same material collected on both instruments. The calculated $Q(E)$ in turn can be used to transform any as-received spectrum into an absolute intensity spectrum which includes only the term $I_b \cdot n(E)$. This method was initiated by Seah and his colleagues in NPL [100] and has greatly simplified the intensity calibration process. The result of a round-robin AES measurement indicates that $\pm 2\%$ spectral reproducibility can be achieved readily [96-98] on instruments calibrated this way. A tremendous amount of work has been done by NPL to calibrate their AES instrument and generate standard reference spectra on their spectrometer [110, 128]. Following their work, SASJ also built a database collected on a home-built novel AES system[101, 107, 129]. The intensity calibration for our PHI 680 SAN is based on these two sources.

4.3.2 Comparing two calibration sources

Both NPL and SASJ have built software packages incorporating the reference spectra and made them available at http://www.npl.co.uk and http://www.sasj.gr.jp respectively. Comparisons of the experimental conditions for the reference spectra collected at NPL and SASJ and operation parameters for the PHI 680 SAN are in Table 4-6. Both the metrology spectrometer of NPL and the novel Auger spectrometer of SASJ have been modified to reduce internal scattering of the energy analyzer and to avoid uneven electron detection efficiency. In both instruments, a Faraday cup has been applied instead of an electron multiplier and the subsequent counting circuit for the purpose of electron detection.

The metrology spectrometer of NPL is equipped with a concentric hemi-spherical analyzer (CSA) with constant energy acceptance width ΔE, for which the transmission

Table 4-6: Comparisons on the experiment conditions for the standard reference spectra provided by NPL and SASJ and our experimental conditions (ORNL).

Institute	*NPL*	*SASJ*	*ORNL*
References	[110, 128, 130, 131]	[101, 107, 115, 129, 133, 134]	
SPECIMEN			
Material	Cu, Ag, Ag	Cu, Ag, Ag	Cu, Ag, Ag
Source	SCAA 87 set		Alpha Aesar®
Preparation	Ar ion sputter	Ar ion sputter	Ar ion sputter
Tilt angle	30o	0	0
Analysis area	6mm*9mm	0.05mm*0.05mm	0.05mm*0.05mm
Instrument Name	Metrology Spectrometer	Novel CMA	PHI 680 SAN
ENERGY ANALYZER			
Type	CSA	CMA	CMA
Woke mode	FRR (constant ΔE)	FAT(constant ΔE/E)	FAT
Internal scattering	<0.5%	<0.1%	
Energy resolution	1 eV	0.25%	0.68%
Transmission efficiency		5.6%	6.3%
Electron detector	CEM	Faraday cup	MCP
Counting mode	Pulse counting / analogue	analogue	Pulse counting
Beam current		1000 nA	
Beam energy	5 keV	5 keV	
REFERENCE SPECTRA			
Unit of intensity	sr-1eV-1	nA	count/s
Energy range	20-2500 eV	0-5000 eV	0-3200 eV
Energy refer to	Fermi level	Fermi level	Fermi level
Factor incorporated		Ib, T(E)	Ib, T(E), D(E), F

efficiency is scaled in solid angle. After data processing, the reference spectrum intensity is in the unit of $sr^{-1} \cdot eV^{-1}$ [110, 128, 130, 131], as will the calibrated spectra. An integration of the calibrated spectrum over emission space and energy range produces a unit-less secondary emission yield. Unfortunately the reference energy range is limited to 20~2500 eV, insufficient for the purpose of calculation SE yields.

The reference spectra of SASJ are in units of nA. They are collected by Goto and are the direct output data from the Faraday cup and thus incorporate the effect of CMA transmission and the incident beam current (1000 nA). Both of these two effects should be corrected before carrying out the calibration. The energy range of the SASJ reference is 0~5000 eV including the full range of slow secondaries. For this reason Goto's absolute spectra [107] which are available in the SASJ data bank are used as our main reference, while the data of NPL will be used for comparison.

The energy resolution of the novel CMA of SASJ is R% = 0.25% [101, 107, 129]. The CMA transmission efficiency $T(E)$ can be deduced from here. As stated in section 4.2.1.2, the transmission function of a CMA working in the constant $\Delta E/E$ mode is

$$T(E) = \Delta E \cdot (W \cdot 1.99\Delta\alpha) \tag{4-18}$$

According to equation (4-7) $\Delta\alpha$ equals 0.077 radians for $\Delta E/E = 0.25\%$. Thus the effective solid angle fraction is $\overline{\Omega} = 1.99\Delta\alpha = 0.153$, In Goto's novel CMA system, two wire mesh screens with a transparency of 67% cover both the entrance and exit windows, and the entrance window has supporting bars occupying about $1/3$ of the area [132], giving the optical transparency as

$$W = 0.67 \times 0.67 \times (1 - 0.333) = 0.3 \tag{4-19}$$

The spatial transmission efficiency $T = W \cdot \overline{\Omega}$ (equation 4-20)of this CMA is thus about 4.5%, close to their published value 5.6% [134]. We will use their value of 5.6% in later calculations. Measurement of the $FWHM$ for Goto's absolute spectra agrees well with the predicted value $\Delta E = 0.25\%E$ as shown in Figure 4-14. Thus the transmission function for this CMA is

$$T(E) = 5.6\% \times 0.25\%E = 1.4 \times 10^{-4} E \ \ (eV) \tag{4-21}$$

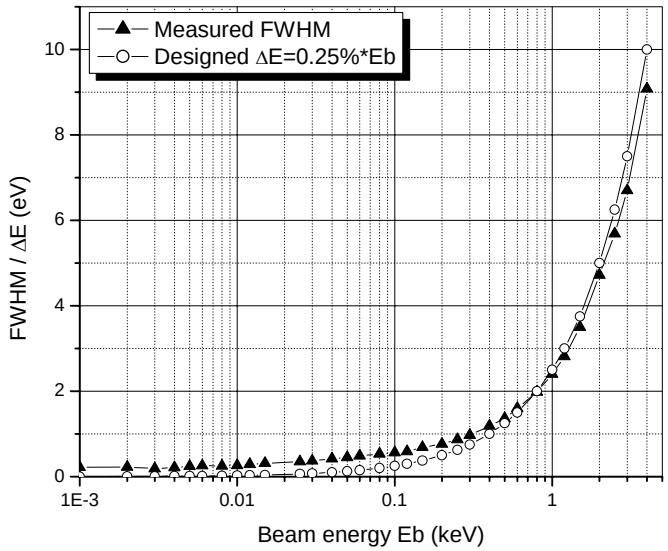

Figure 4-14: A comparison between the measured FWHM of the elastic peak for Au on Goto's absolute spectra in the data bank of SASJ and the theoretical energy resolution $\Delta E = 0.25\% E$

4.4.3 Experiment set up and calibration steps

The spectra collected on the PHI 680 SAN are for samples of Ag, Au and Cu foil ordered from Alpha Aesar® with purity higher than 99.9%. Since the foils are oil-free and the surfaces are flat, no additional polishing was done before inserting the foils into the UHV chamber. The foils are attached to the sample holder with metal screws to insure good electric conductivity. Once in the analysis chamber, samples were sputter-cleaned with an Argon ion beam of $3.5\,kV$, beam current of $3\ mA$ on an area of $0.5mm \times 0.5mm$. These ion beam conditions have been calibrated to give a sputtering rate of 310 Å per minute on a standard tantalum oxide film. After 10~20 minutes of sputtering nearly all of the C and O surface contamination can be removed. This low sputtering rate was chosen to reduce the surface roughening that can be induced by the selective etching of the ion beam on an inhomogeneous poly-crystal surface. To further reduce sputtering-induced roughness, the "Zalar rotation" mode was chosen whereby samples are rotated about the surface normal during sputtering while keeping the ion incidence at 30^o polar

angle. Electron beam currents were measured by focusing the beam into a hole 0.5 mm in diameter and 5 mm deep drilled into the aluminum sample holder. No bias voltage is applied during current measurement to reduce any leakage that could be induced. The spectra are collected with step size of 1 eV/step and dwell time of 20ms/step. To achieve good counting statistics, 5 cycles of scans across the kinetic energy range 0-3200 eV were obtained. Repeated measurements were made with samples normal and tilted 30^o to the e-beam incidence for input into the SASJ and NPL calibration software respectively. Other important experimental parameters used are listed in Table 4-5 and Table 4-6.

Even when electron kinetic energies are referenced to the Fermi energy, the output energy for the same Auger transition may vary in different instruments since they may have different work functions, as shown in Table 4-7. Electron kinetic energies will be automatically aligned in the software of NPL. The energies of the SASJ reference spectra need to be shifted +2 eV before the spectra are referenced to calibrate the PHI 680 SAN.

The steps taken to calculate the response function Q(E) of the PHI 680 SAN and to use Q(E) to transform the as-received spectrum into the true spectrum are shown in the flow chart of Figure 4-15. The dead time and dark count should be corrected for the as-collected spectra from the PHI 680 SAN prior to any calculation. The CMA transmission efficiency in units of eV needs to be corrected for the SASJ spectra before they can be used as references to calculate $Q(E)$.

Since the reference spectra of SASJ and NPL have different intensity units, so will the response functions. Conversion between the two units is deduced as follows in order to make comparisons between them possible. As the spectral unit for the PHI 680 SAN is count per second (cps), and all the incident beam currents have unit of nA, $Q(E)$ based on the SASJ reference following the flow chart in Figure 4-15 will have unit of:

$$\frac{cps/nA}{nA/(nA\cdot eV)} = \frac{cps\cdot eV}{nA}$$
$$= \frac{6\times10^{-19}A\cdot eV}{1\times10^{-9}A} = 1.6\times10^{-10}eV \qquad (4\text{-}22)$$

While the output $Q(E)$ from the NPL calibration software [136] has unit of A_o [100],

Table 4-7: Comparisons on the energies of several intense AES transitions on the E*N(E) spectra collected for pure Cu, Au, and Ag.

Transition	*Kinetic energy, eV*		
	NPL [135]	SASJ*	ORNL
Cu $M_{2,3}VV$	61.16	57	59
	63.4	59	61
Au $N_{6,7}VV$	70.1	66	68
	72.2	68	70
Ag M_4NN	357.81	353	355
Cu L_3VV	918.62	914	917
Au $M_5N_{6,7}N_{6,7}$	2015.57	2018	2018

*** Data from the Goto's absolute direct AES database incorporated in the software package available on http://www.sasj.gr.jp respectively.**

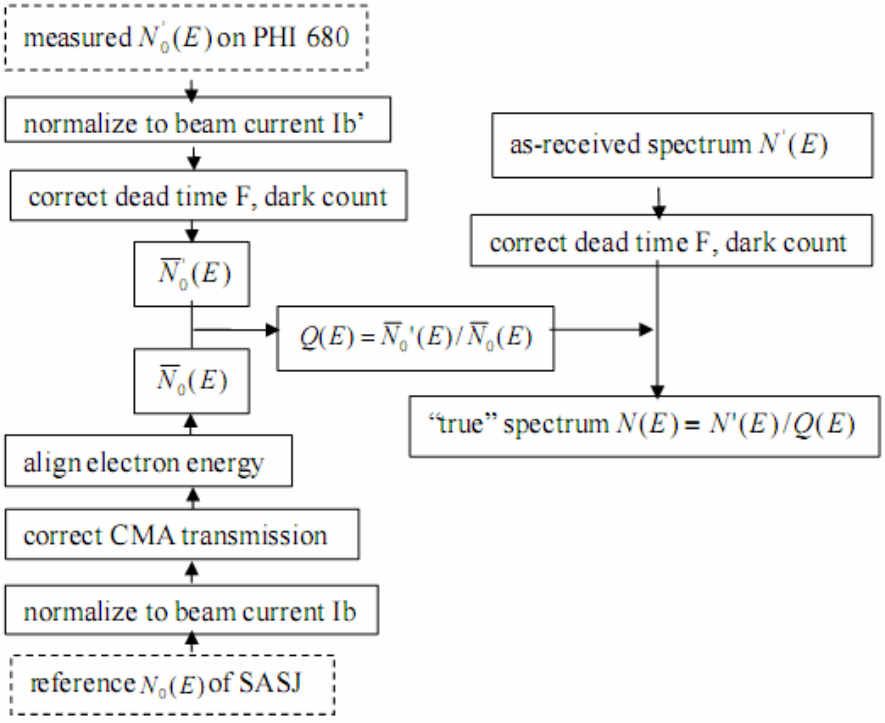

Figure 4-15: Flow chart to calibrate the spectrum intensity for PHI 680 SAN based on the reference spectra of SASJ.

and

$$A_0 = (3.14 \pm 0.19) \times 10^{-4} \quad sr \cdot eV \tag{4-23}$$

The solid angle unit sr originates from the normalization over the electron emission space that has been done by NPL on the reference spectra. Assuming electron emission distribution follows a cosine law, the effective solid angle of the emission space is

$$\Omega = \frac{\int_0^{\pi/2} 2\pi R^2 \sin\alpha \cdot \cos\alpha d\alpha}{R^2} = \pi \quad (sr) \tag{4-24}$$

Thus conversion between the scales of these two response functions is:

$$Q(E)_{SASJ} \times 1.6 \times 10^{-10}(eV) = Q(E)_{NPL} \times 3.14 \times 10^{-4} \times {}^{1}\!/\!_{\pi}(eV) \tag{4-25}$$

4.4.4 Response function Q(E) of PHI 680 SAN

Figure 4-16 is the calibration results for the PHI 680 SAN based on the NPL and SASJ references and serves as a check on the agreement between them. To emphasize the effect of non-linearity, the response functions are presented as the unitless $Q(E)/E$ with E. Figure 4-16 (a) is the result based on the SASJ references for repeated measurements on pure Ag, Au, and Cu. A saw-tooth-shaped wave can be observed on the otherwise smooth $Q(E)/E$ lines. These waves are located on the intense Auger transition regions, around 350 eV for Ag MNN, 60 eV for Cu MVV and 920 eV for Cu LVV, indicating a non-negligible inner scattering for the CMA in the PHI 680 [114, 115]. The response function profiles for E>10 eV take the shape of the SE yield universal curve, indicating the strong $D(E)$ effect of the MCP in PHI 680. The values for E<7 eV are extraordinarily high, meaning that the SE spectral intensity collected on the PHI 680 is much higher than that of the reference.

The high values on the low energy range may be caused by one or more of the follow reasons. First, the energy acceptance widths of the CMA in the PHI 680 for low energy electrons are wider than the theoretical values as indicated in Figure 4-6, causing an increase in the collected electron count. Second, the high output SE intensity in the PHI

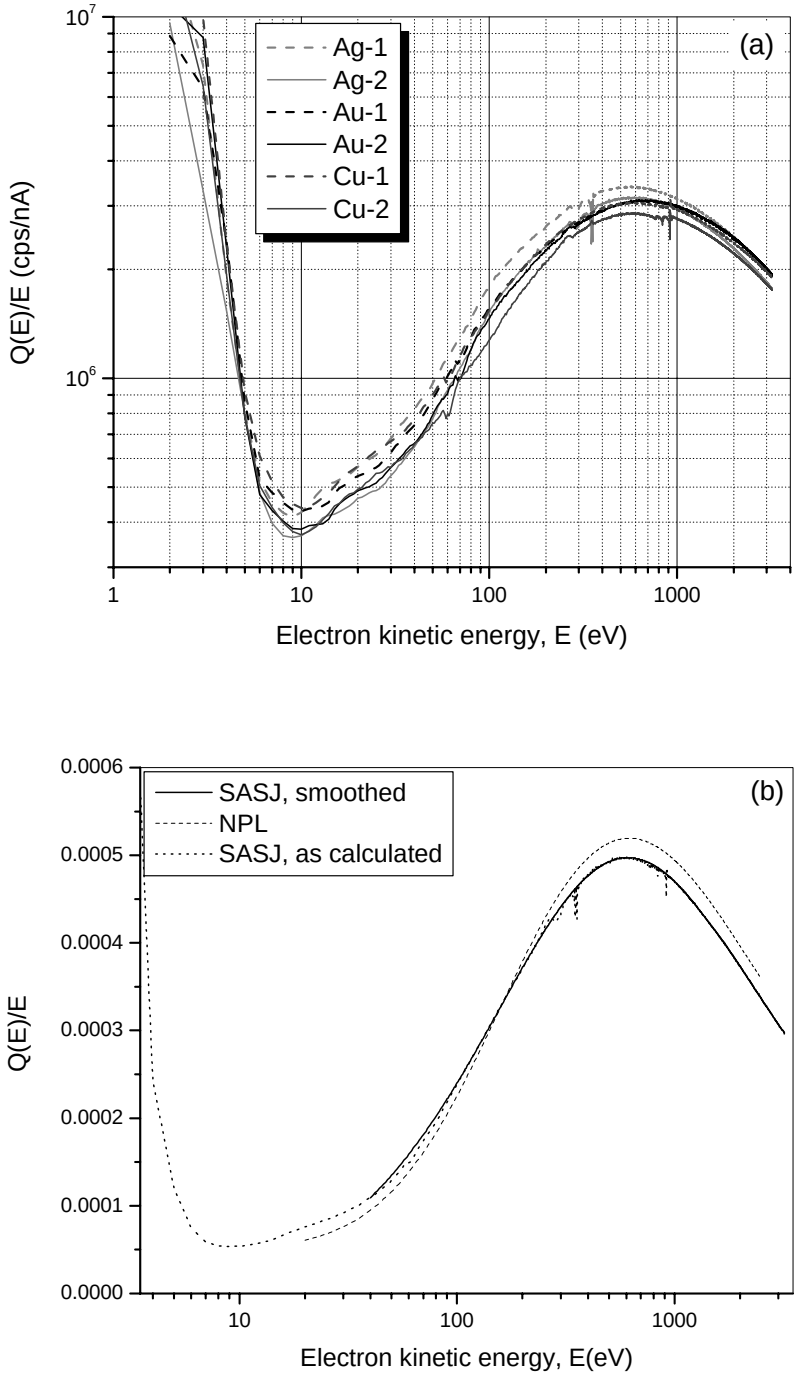

Figure 4-16: The Q(E)/E for PHI 680 SAN. (a) Calibration based on Goto's absolute spectra on the SASJ data bank. The Q(E)/E lines are for two sets of measurement on Ag, Au and Cu. (b) Q(E)/E produced by the two institutes agree well with each other. The Q(E)/E are converted to be unitless. The smoothed SASJ data are presented in the range of 40~3200 eV.

680 could be contributed by the noise from the MCP. For unknown reason, when the output signals from the 8 separate channels of the MCP were compared, 2 of them showed extraordinarily high intensities in the low energy range. Finally, the SASJ system may simply have lower collection efficiency in this energy range determined by their instrument setting. Before any further confirmation can be made, no modulation was made on the as calculated intensity-energy response function. The obvious result, however, is that the "true spectrum" calibrated with this response will have decreased intensities for SE.

The response functions $Q(E)/E$ from the NPL calibration package [136] are in appendix 2. NPL uses the rational function shown below to smooth the average curve:

$$Q(E)/E = \frac{a_0 + a_1\varepsilon + a_2\varepsilon^2 + a_3\varepsilon^3 + a_4\varepsilon^4}{1 + b\varepsilon_1 + b_2\varepsilon^2 + b_3\varepsilon^3 + b_4\varepsilon^4} \tag{4-26}$$

where

$$\varepsilon = (E - 1000eV)/1000\,eV \tag{4-27}$$

To smooth the as calculated average response function for the PHI 680 SAN we use the same rational function (4-26) to construct the curve in Figure 4-16 (a). Using MS Excel, the 9 factors in the unit of cps/nA are listed below:

$$a_0 = 2.937592\times10^6$$

$$a_1 = -5.054422\times10^6, b_1 = -1.497807$$

$$a_2 = -0.360523\times10^6, b_2 = -0.38407$$

$$a_3 = 8.253046\times10^6, b_3 = 2.430646$$

$$a_4 = 0.562111\times10^6, b_4 = 1.168022$$

The smoothed SASJ response function smears the spikes caused by the CMA internal scatterings on the as-calculated curve and agrees well within the range of E>40eV (Figure 4-16 (b)). In the range E<40 eV the fitted curve deviates from the abnormally high values of the as-calculated response function. For our calibration, the response function is composed of two parts: smoothed data in the range E>40eV and the as-calculated average data for E<40eV.

Comparison of the response functions based on SASJ and NPL references is also shown in Figure 4-16 (b). The two $Q(E)/E$ lines cross at about 200 eV; at lower energies, the SASJ calibration has higher values but is opposite in the high energy region, which means that the SASJ calibration has higher estimation on the collection efficiency for the low energy electrons on the PHI 680 SAN. The discrepancy between these two sets of values in the overlapping energy region (20-2500 eV) is small, no bigger than the absolute uncertainty evaluated by NPL (14%). This justifies using the SASJ-based response function for calibration.

Figure 4-17 shows how this calibration reconstructs the real spectrum. In Figure 4-17(a) the calibrated Si spectrum has much higher intensity for both the low energy SE and the high energy BSE compared to the as-received spectrum. The calibrated spectrum after being corrected for the CMA transmission efficiency is shown in Figure 4-17(b). The importance of the SE contribution to the electron spectrum is obvious. SE is the most intense signal with a narrow energy distribution.

A comparison is shown in Figure 4-18 of the reference SE spectrum, the as-measured data and the calibrated spectrum for Au (Figure 4-18 (a)), the reference material, and for Cr (Figure 4-18 (b)). To emphasize the SE peak profiles, the spectra are presented in the form of N(E)*E and are normalized to their respective maxima. The SASJ and the calibrated SE spectra are all started from 2 eV because of the energy alignment applied. The calibrated spectrum for Au (Figure 4-18 (a)) agrees well with that of the reference. Comparing to the as-received spectra, the calibrated SE spectra have a more obvious peak at around $10\,eV$. The SE spectra as received from the PHI 680 SAN are generally flat due to its lower energy resolution and internal scattering of CMA, etc. A study of the SASJ SE spectra for the three reference materials (Au, Cu and Ag) shows that they have almost overlapping profile, peaking at around $10\,eV$, probably because these materials are belonging to the same group in the periodical table. The response function based on these references, when applied to other materials, tends to force a SE peak at approximately the same energy ($10\,eV$), which ultimately causes small disagreement of the calibrated spectra with that of the SASJ reference. For example, the Cr MVV peak at $32\,eV$ is weakened (Figure 4-18 (b)) after the calibration.

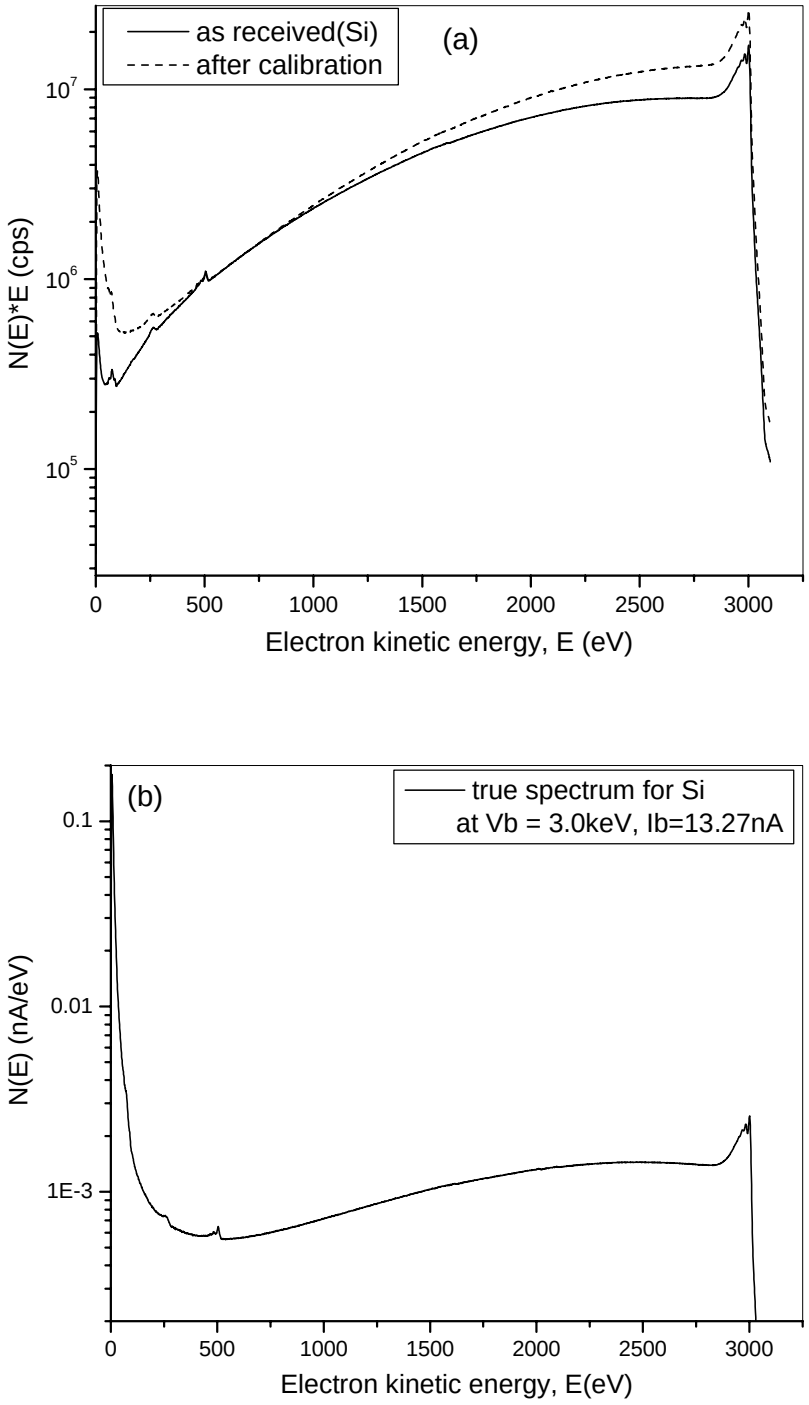

Figure 4-17: (a) Comparison of spectra for Si collected on PHI 680 SAN before and after intensity calibration. The calibrated spectrum has much higher intensity at low and high energies. (b) The calibrated Si spectrum corrected for the CMA transmission efficiency.

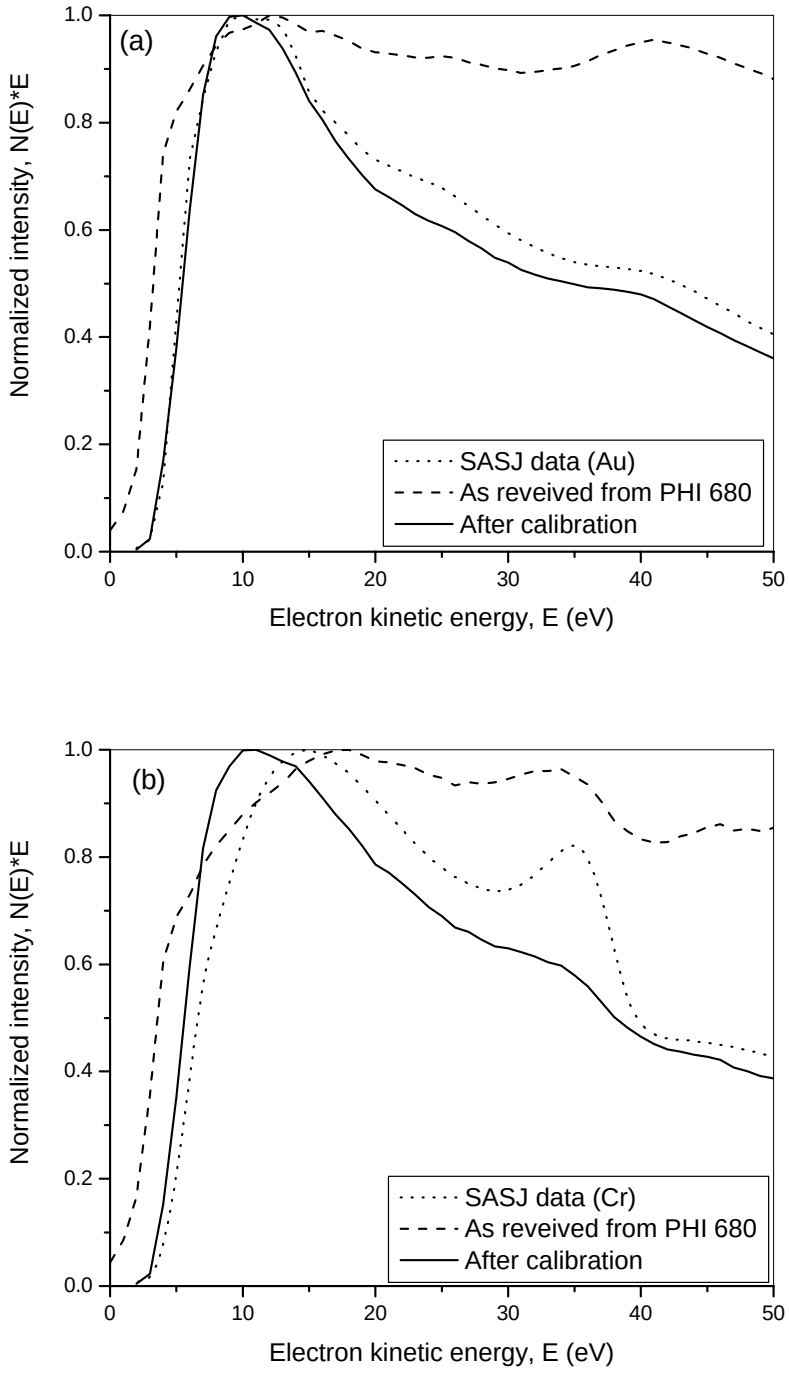

Figure 4-18 Comparison of the SE spectra of the reference, the as received measurement from PHI 680 SAN and after calibration for material of (a) Au and (b)Cr .

A template in the form of an MS Excel data sheet for converting the as received spectra collected on PHI 680 SAN to the real ones is given in Appendix 1.

4.4 Conclusions

A novel method for measuring SE yields by integrating the electron emission spectrum is shown to be feasible. This method is superior to others because it gives the yield and the energy distribution at the same time, measures samples free of surface contamination, and is able to correlate the relationship of yield with sample composition. The AES spectrometer needs to be aligned carefully to get reproducible spectra. For the PHI 680 SAN at ORNL we used in our experiments, operation parameters need to be optimized for the three main parts: the electron energy analyzer (CMA), the electron multiplier (MCP) and the electronic counting circuit. Each of these parts contributes to loss of spectral intensity. It is also clear that each spectrometer has its own characteristic intensity-energy response function.

The spectral intensity needs to be absolutely calibrated before calculating SE and BSE yields. Calibration can be accomplished using the reference spectra provided by NPL and SASJ. Comparison of the response functions for the PHI 680 with these two references shows good agreement in the energy range between 20 to 2500 eV. The response function has a profile similar to the SE yield universal curve, indicating that the greatest contribution to efficiency loss comes from the MCP. The response function based on the SASJ reference has extraordinary high values for electron energy less than 7 eV, indicating either abnormally high intensity for the SE collected on the PHI 680 or low collection efficiency of the SASJ instrument. SE yield calculated based on this intensity-energy response function will have values lower than expected. A real spectrum constructed by this calibration will have much higher intensities for both the low and high energy electrons than the as-collected spectrum. Other than flatness as of the as-received SE spectra from the PH680 SAN, all calibrated SE spectra have an obvious intense peak. While the calibration strengthens the SE peak at approximately 10 eV, it also weakened the Auger peaks at higher energies.

5. Chapter Ⅴ: SE, BSE yields measurement based on the calibrated AES spectra

In this chapter we present the SE and BSE yields based on spectra collected on the PHI 680 SAN and calibrated by the method discussed in chapter 4. Our purpose is to systematically investigate variations of the yields with atomic number and with chemical gradient of binary alloys. We have measured a set of elements and two alloys, Au-Cu and Cr-W, and the results will be discussed in the groups accordingly. The yields calculated from the SASJ database will be discussed first so that the experimental results can be scaled. The method of calculating the secondary yields from the AES spectra will be discussed at the beginning of this chapter.

The experimental set up is almost the same as that for the pure Au, Ag, Cu spectra collected and discussed in chapter 4. The set of samples were attached to 6 cm diameter holder with metal screws for good electrical contact. Each sample was of the same height so that moving from sample to sample did not cause any misalignment. A hole 0.5 mm in diameter and 5 mm deep was drill into the aluminum sample holder to be used as a Faraday cup for measuring beam current. Ar ion beam was used to clean samples before data collection. The "Zalar rotation" sputter mode was not used to avoid cross-contamination by re-deposition. Instead, samples were tilted 30^{o} towards the ion beam to reduce surface roughening. In this configuration, long teeth and trenches that could greatly enhance the electron yield were not observed on the Au and Cu surface. Spectra were collected with a step size of 1 eV/step and dwell time of 20 ms/step. Repeated cycles of data collection over the energy range of interest were made to increase the counting statistics. All spectra were collected with the electron beam axis normal to the sample surface.

5.1 Calculating secondary yield from AES spectra

Secondary electron yield is the ratio of the emitted SE count divided by the total count of incident electrons. To calculate the SE yield from a calibrated AES spectrum

with known incident beam current, one also needs to know the number of SE emitted in unit time. We have mentioned before that the area under the spectrum is the total number of emitted electron. Here we show why this claim is reasonable from two aspects.

First we show agreement of the units. Since the as-received spectrum from the PHI 680 SAN has intensity expressed in units of count per second (cps), and $Q(E)$ has units of $sr \cdot eV$ for the NPL references and eV for the SASJ references, the calibrated spectrum will have intensity units expressed in $cps \cdot sr^{-1} \cdot eV^{-1}$ (NPL) or $cps \cdot eV^{-1}$ (SASJ). Thus an integration of the spectra over the energy range (and additionally over the effective solid angle for NPL), which is the area under the spectrum, will produce a quantity with the same units of the incident beam current. This area normalized to the incident beam current is the unitless secondary yield.

Second we will prove it from analyzing as-received spectra that incorporate the response function $Q(E)$ for CMA-typed instruments. The output spectrum intensity $N(E)$ (normally expressed as $N(E) \cdot E$) is an array of electron counts for which the indexes are the electron kinetic energy E . Since the CMA accepts electrons with kinetic energies E in the range $(E - \Delta E/2) \le E \le (E + \Delta E/2)$, $N(E)$ are actually the areas of the electron pulses following certain distributions. Assuming for energy index E_0 the collected electrons have a Gaussian distribution with $FWHM = \Delta E_0$ (Figure 5-1), and

$$I(E) = \frac{N(E_0)}{\sqrt{2\pi}\sigma} \exp\left(-\frac{(E - E_0)^2}{2\sigma^2} \right) \qquad (5\text{-}1)$$

then

$$FWHM = \Delta E_0 = 2\sqrt{2\ln(2)} \cdot \sigma \qquad (5\text{-}2)$$

$$\sigma = 0.4247 \cdot \Delta E_0 \qquad (5\text{-}3)$$

the most probable count number $I(E_0)$ at E_0 will be

$$I(E_0) = \frac{N(E_0)}{\sqrt{2\pi} \times 0.4247 \Delta E_0} \approx 0.94 \frac{N(E_0)}{\Delta E_0} \qquad (5\text{-}4)$$

So the Gaussian distribution as expressed in equation (5-1) will have approximately

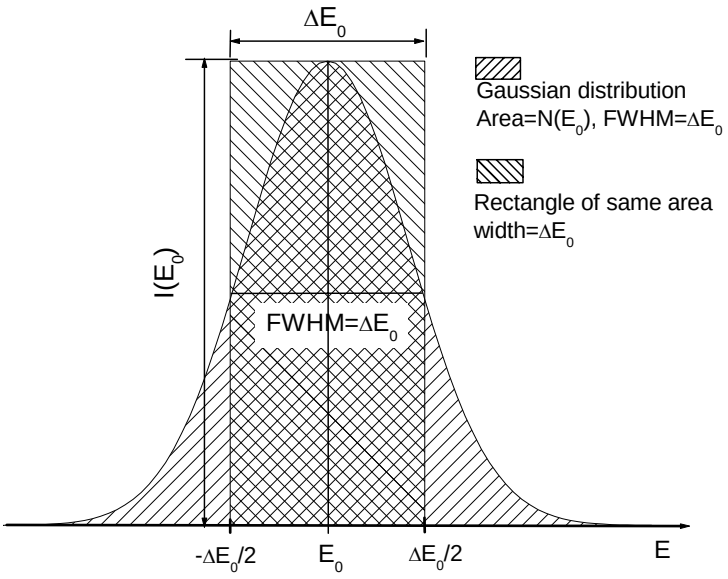

Figure 5-1: Deconvolution of the electron count of energy E_0 from the total spectrum.

the same area as a rectangular one of width ΔE_0 and height $I(E_0)$, as in Figure 5-1:. $I(E_0)$ can be considered the mean electron count for every infinitesimal energy increase in the range $[E_0 - \Delta E_0/2, E_0 + \Delta E_0/2]$. As a result, an integration of $I(E)$ over E is the total electron number. Since ΔE has linear relationship with E as determined by the CMA transmission function $T(E)$, $I(E)$ is actually the spectrum intensity corrected for instrument response function $Q(E)$. Again, this shows that the area under a calibrated spectrum is the total electron number. To be consistent with claims we made in chapter 4, later in this chapter we express the intensity of the as received spectrum from the CMA as $N(E) \cdot E$ instead of $N(E)$ and the intensity corrected for the instrument response function as $N(E)$ instead of $I(E)$. The unit for $N(E) \cdot E$ is cps and for $N(E)$, $cps \cdot eV^{-1}$.

For the spectrum collected at Δ eV/step the area A under the spectrum is:

$$A = \sum N(E) \cdot \Delta \qquad (5\text{-}5)$$

Similarly, the SE yield δ and BSE yield η are:

$$\delta = \frac{\sum_{0}^{50eV} N(E) \cdot \Delta}{I_b} \quad (5\text{-}6)$$

$$\eta = \frac{\sum_{50eV}^{E_b} N(E) \cdot \Delta}{I_b} \quad (5\text{-}7)$$

5.2 Analyzing the SASJ database

Goto's absolute AES spectra in the SASJ database include data for 14 elements and for beam energies ranging from 1eV to 5000 eV. The yields for these elements can be calculated by the process discussed above for the spectra after correcting for the instrument response function. Table 5-1 and Table 5-2 are the list of the BSE and SE yields respectively. It is hoped that this systematic measurement on the elements will provide evidence for the atomic shell filling effect. In addition, the results can be used to scale the signal collection efficiency of the SASJ instrument and to test the reliability of the PHI 680 SAN when used for measuring the electron emission yield. The calculated BSE yields η (Figure 5-2) increase rapidly in the low beam energy ranges ($E_b < 1keV$) to ~0.3-0.5 and are almost constant after that. Agreeing with most of experimental observations, for elements of atomic number $Z < 29$, BSE yield decreases as beam energy increases in the range of $E_b > 1keV$, and increases with E_b otherwise.

The SASJ SE yield variation with beam energy follows the profile of the universal curve as shown in Figure 5-3 (a). The maximum SE yields vary in the range 0.45-1 and corresponding beam energies vary in the range 0.2-0.6 keV . Comparison of the maximum SE yields and corresponding beam energies with the optimization from the SE yield database [80, 93] (Figure 5-3 (b)) shows that the SASJ SE yields are only half that of the optimized data in value but showing agreement on the varying trend with atomic number. The corresponding maximum beam energies of these two groups are in the same range. Since the values of the BSE yields are in the normal range, we believe that the experimental SASJ SE yields are lower than the actual values, otherwise for most of the

Table 5-1: Calculated BSE yield for the elements from Goto's absolute AES spectra in SASJ database under a list of beam energies Eb.

Eb (keV)	Al-13	Si-14	Cr-24	Fe-26	Ni-28	Cu-29	Zn-30	Ga-31	Mo-42	Ag-47	*Ta-73*	*W-74*	*Pt-78*	*Au-79*
0.06		0.09	0.07	0.07	0.05	0.03	0.04		0.05	0.07	0.03	0.02	0.05	
0.08		0.16	0.12	0.11	0.11	0.03	0.07		0.08	0.09	0.05	0.04	0.06	0.07
0.1	0.00	0.2	0.17	0.16	0.16	0.15	0.11	0.1	0.11	0.11	0.07	0.05	0.08	0.08
0.12		0.23	0.21	0.21	0.2		0.15		0.13	0.15	0.08	0.06	0.09	0.1
0.15		0.25	0.25	0.25	0.25	0.24	0.19		0.18	0.2	0.09	0.08	0.11	0.12
0.2		0.28	0.29	0.31	0.31	0.3	0.25	0.22	0.22	0.29	0.12	0.11	0.13	0.14
0.25	0.00	0.28	0.34	0.35	0.37	0.35	0.28		0.24	0.31	0.17	0.15	0.16	0.16
0.3		0.29	0.35	0.37	0.38	0.38	0.31		0.26	0.33	0.23	0.22	0.21	0.21
0.4		0.29	0.37	0.4	0.43	0.42	0.38		0.29	0.34	0.35	0.34		0.32
0.5	0.28	0.29	0.37	0.41	0.45	0.45	0.42	0.4	0.32	0.35	0.41	0.41	0.42	0.4
0.6		0.28	0.37	0.42	0.45	0.46	0.44		0.34	0.39	0.45	0.44	0.46	0.45
0.8		0.28	0.39	0.41	0.45	0.46	0.46		0.36	0.39	0.46	0.45	0.48	0.48
1	0.27	0.27	0.35	0.4	0.44	0.47	0.47	0.44	0.38	0.44	0.45	0.45	0.47	0.47
1.2		0.27	0.38	0.39	0.44	0.44	0.47		0.39	0.42	0.45	0.45	0.47	0.47
1.5		0.26	0.34	0.38	0.43	0.44	0.46		0.4	0.43	0.46	0.45		0.47
2		0.26	0.33	0.37	0.41	0.42	0.45	0.43	0.4	0.45	0.49	0.48	0.49	0.49
2.5		0.15	0.32	0.36	0.4	0.41	0.43		0.4	0.43	0.51	0.5	0.51	0.51
3	0.22	0.11	0.32	0.35	0.39	0.41	0.43		0.4	0.43	0.51	0.51	0.53	0.52
4		0.07	0.31	0.34	0.38	0.39	0.42		0.4	0.42	0.52	0.52	0.54	0.54
5	0.04	0.23	0.31	0.33	0.37	0.38	0.42	0.39	0.4	0.44	0.52	0.52	0.54	0.54

Table 5-2: Calculated SE yield for the elements from Goto's absolute AES spectra in SASJ database under a list of beam energies Eb.

Eb (keV)	*Al-13*	*Si-14*	*Cr-24*	*Fe-26*	*Ni-28*	*Cu-29*	*Zn-30*	*Ga-31*	*Mo-42*	*Ag-47*	*Ta-73*	*W-74*	*Pt-78*	*Au-79*
0.06		0.33	0.34	0.31	0.31	0.25	0.2		0.41	0.38	0.32	0.35	0.44	0.38
0.08		0.33	0.38	0.36	0.37	0.3	0.22		0.47	0.43	0.35	0.36	0.5	0.43
0.1	0.00	0.32	0.41	0.39	0.42	0.34	0.25	0.36	0.51	0.48	0.37	0.41	0.57	0.47
0.12		0.33	0.43	0.41	0.44		0.26		0.54	0.52	0.39	0.43	0.61	0.5
0.15		0.34	0.45	0.45	0.46	0.41	0.31		0.57	0.56	0.41	0.47	0.66	0.54
0.2		0.34	0.49	0.5	0.56	0.44	0.34	0.5	0.61	0.63	0.45	0.52	0.71	0.59
0.25	0.00	0.33	0.49	0.54	0.6	0.51	0.36		0.64	0.64	0.54	0.58	0.77	0.63
0.3		0.32	0.52	0.56	0.64	0.53	0.38		0.65	0.67	0.58	0.61	0.82	0.68
0.4		0.3	0.51	0.58	0.68	0.58	0.41		0.63	0.7	0.59	0.64		0.73
0.5	0.37	0.28	0.51	0.58	0.67	0.6	0.43	0.56	0.6	0.71	0.59	0.7	0.99	0.75
0.6		0.26	0.46	0.56	0.65	0.6	0.43		0.58	0.71	0.55	0.69	0.99	0.75
0.8		0.22	0.41	0.52	0.64	0.59	0.43		0.53	0.68	0.54	0.65	0.97	0.74
1	0.28	0.2	0.36	0.48	0.61	0.6	0.42	0.5	0.49	0.68	0.51	0.59	0.87	0.7
1.2		0.18	0.33	0.43	0.57	0.52	0.41		0.45	0.6	0.47	0.59	0.85	0.69
1.5		0.16	0.28	0.4	0.5	0.46	0.37		0.4	0.54	0.41	0.5		0.63
2		0.13	0.23	0.31	0.43	0.41	0.31	0.34	0.34	0.52	0.36	0.47	0.77	0.57
2.5		0.11	0.19	0.26	0.36	0.34	0.3		0.29	0.42	0.32	0.4	0.65	0.5
3	0.17	0.09	0.17	0.23	0.31	0.31	0.24		0.25	0.36	0.29	0.37	0.59	0.45
4		0.07	0.13	0.19	0.25	0.25	0.2		0.21	0.31	0.23	0.3	0.48	0.38
5	0.08	0.06	0.11	0.16	0.2	0.21	0.17	0.16	0.17	0.27	0.21	0.26	0.43	0.36

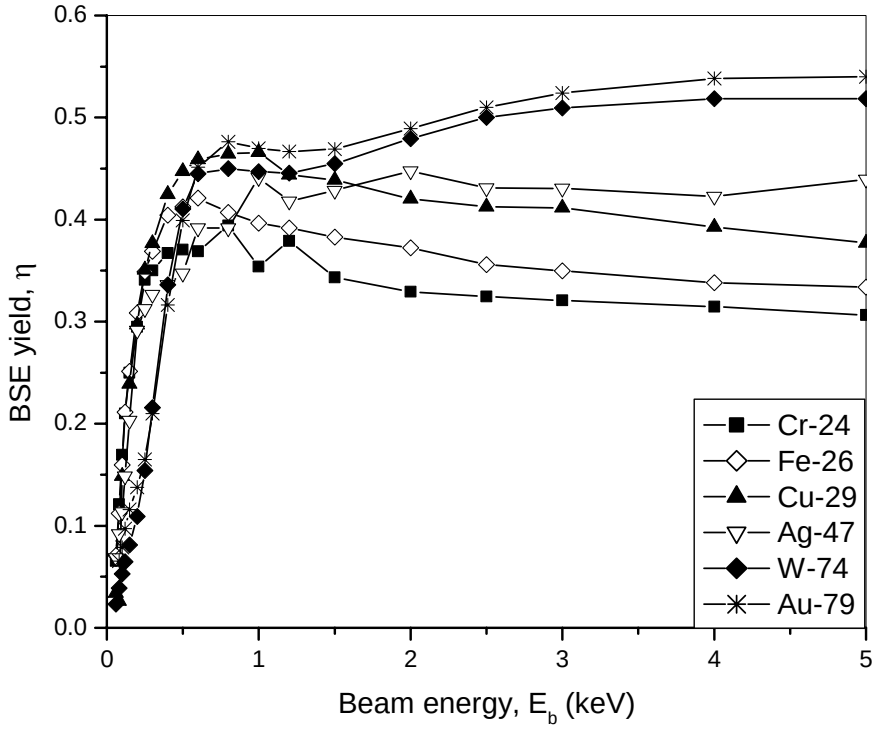

Figure 5-2: Calculated BSE yields varying with beam energy E_b for selected elements based on Goto's absolute AES spectra in the SASJ database.

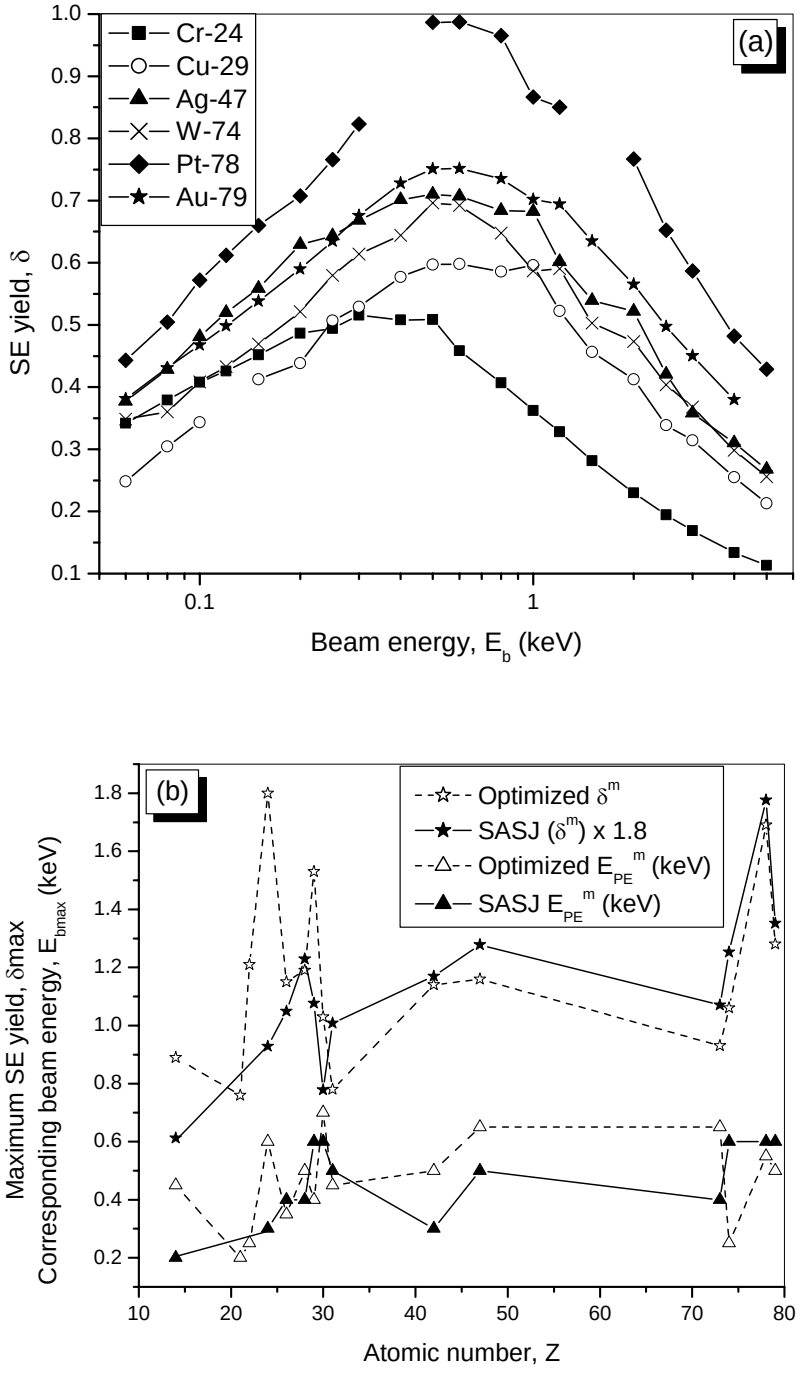

Figure 5-3: (a) SE yields δ calculated from the SASJ database varying with the beam energy E_b. (b) Comparison of the maximum SE yield δ^m and the corresponding beam energy E_{PE}^m varying with atomic number with the optimized data in chapter 3.

elements the total yield would be smaller than 1. In conclusion, the collection efficiency of the SASJ instrument for the low energy SE is only about 50%.

5.3 Experimental results for Elements

The elements used in this experiment are foils of Si(14), Sc(21), Ti(22), Cr(24), Cu(29), Ag(47), W(74), and Au(79) obtained from Alpha Aesar®. Each has purity higher than 99.9%. An experiment using a set of sample elements with wider and more continuous range of atomic numbers failed because of serious charging problems. No surface preparation was done on the sample foils before Ar ion sputter cleaning with beam voltage $3.5\,kV$ and beam current of $3\,mA$ over an area $1mm \times 1mm$ using a sputter rate of 2000 Å per minute. The sputtering lasted for 3-4 minutes, until little trace of C or O contamination could be found. Samples were re-aligned by locating the $1\,keV$ elastic peaks at $1004\,eV$ after the sputter clean. The x, y, z positions for each sample were recorded so that the stage could be accurately re-positioned.

The calibrated SE spectra are shown in Figure 5-4. To strengthen the difference, SE profiles for various elements are expressed as $N(E) \cdot E$ (Figure 5-4 (a)). It is shown that most of the SEs fall in the energy range 5-15 eV with a maximum peak at 8-10 eV. The SE spectra have almost the same profile on the small energy side of the peak, and differentiate from each other on the other side. As a result, different elements have their characteristic FWHM, which has been used for material classification [1]. For the elements measured, Sc has the narrowest energy distribution while Cr has the broadest. The elements observed belong to 3 categories: Sc and Si have smallest FWHM, Cu, Ag and Au in the middle and Cr, W, Ti have largest FWHM. Especially, the spectrum of Cu is almost coincident with that of Au. Another obvious characteristic of the SE spectra is that their profile does not change with incident beam energies, as seen in Figure 5-4 (b) for W. The spectra for W under various beam energies normalized to their respective maximum overlap almost exactly with each other.

Measured SE yields are compared with the SASJ data in Figure 5-5. As seen in Figure 5-5 (a), the SE yields decrease almost linearly with the beam energy from 1 keV to $10\,keV$. The peak yields are obviously less than 1. The data measured on the PHI 680

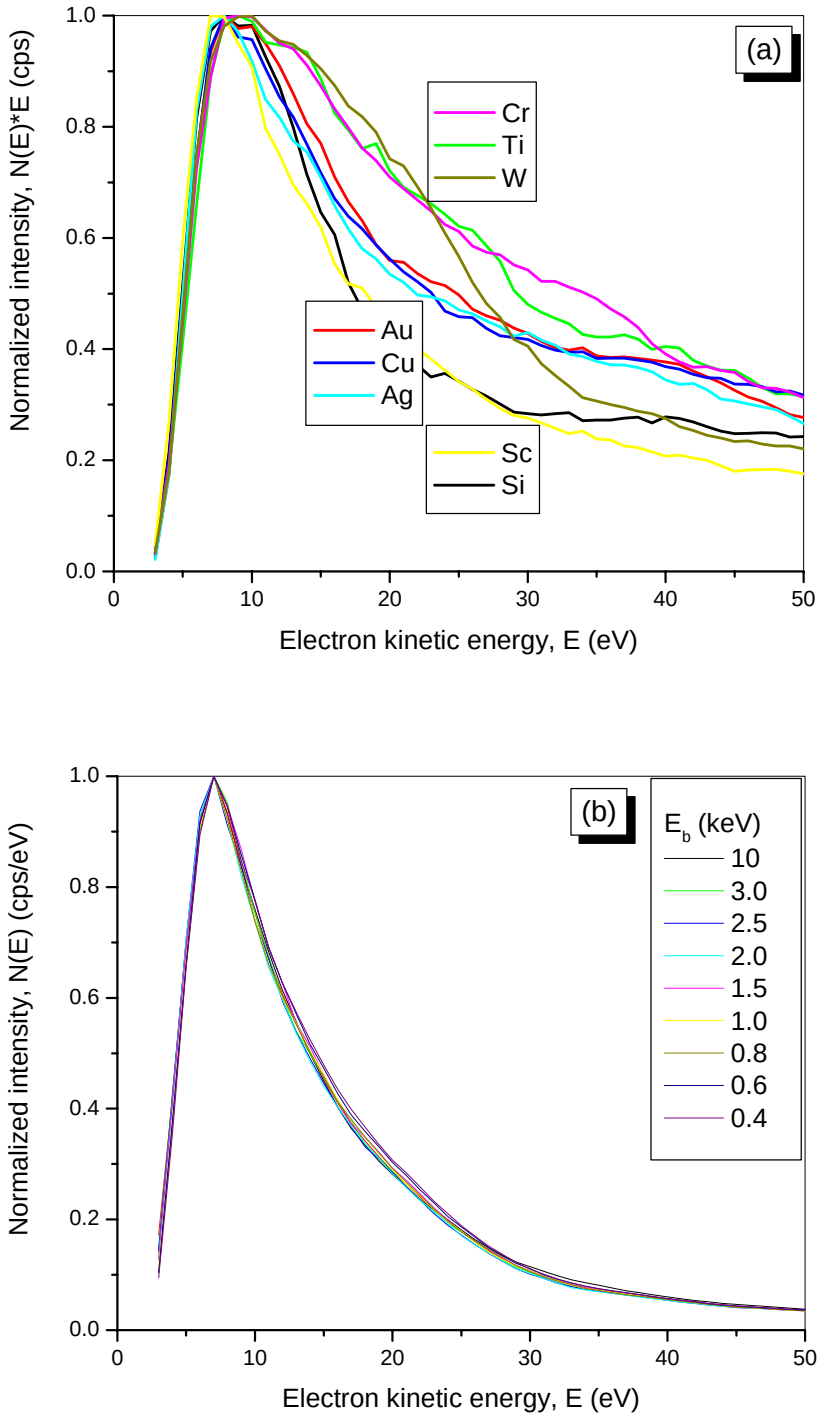

Figure 5-4: The normalized SE spectra collected on the PHI 680 SAN and after calibration. (a) SE spectra in form of N(E)*E for various elements under beam energy of 1 keV. (b) The SE spectra N(E) of W for different beam energies are consistent.

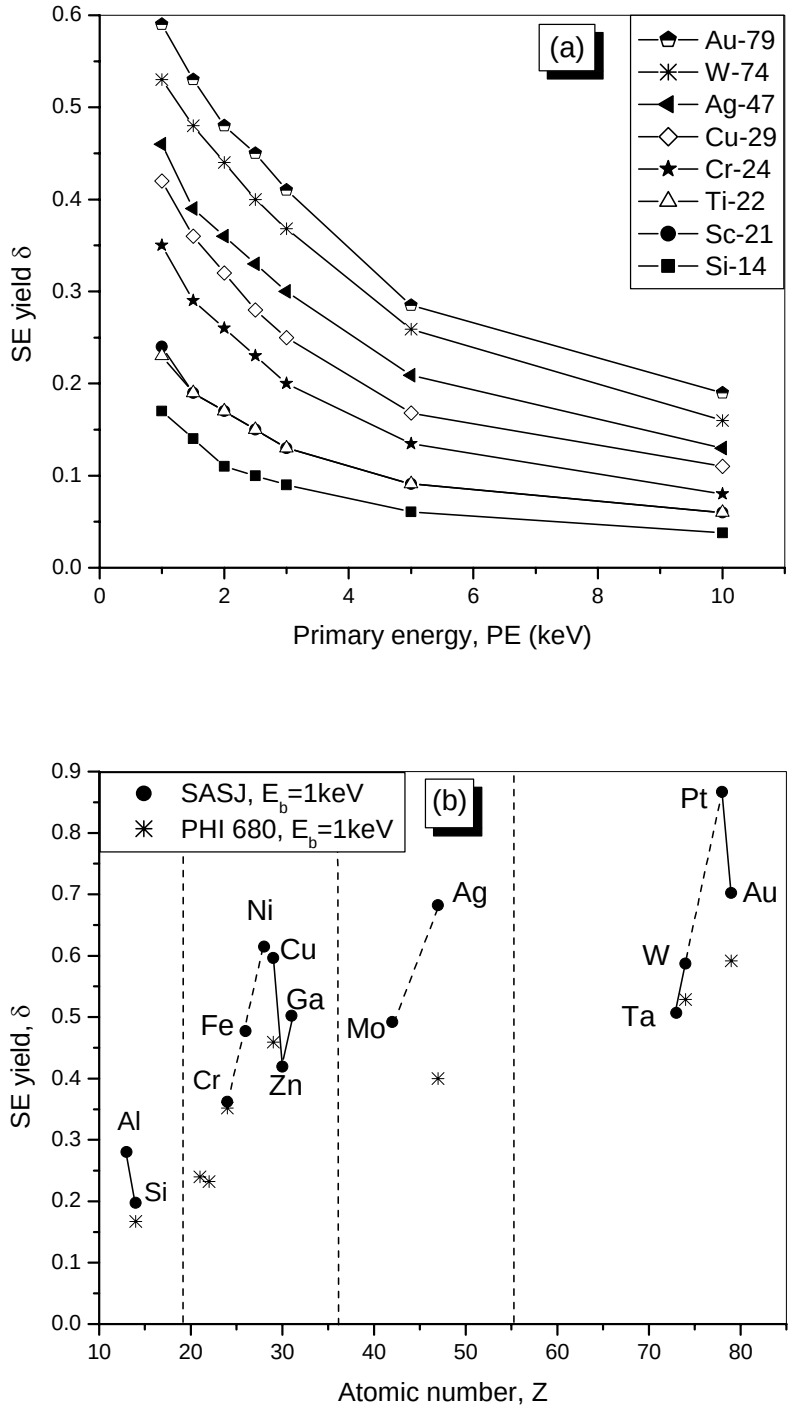

Figure 5-5: (a) The SE yields of elements measured on PHI 680 SAN vary with beam energy. (b) Comparison of the SE yields at beam energy of 1 keV measured on the PHI 680 SAN and that of SASJ as a function of atomic number demonstrates an atomic shell filling effect.

SAN are a little lower than that of the SASJ which in turn was 50% of the optimized database, but both sets of data show an atomic shell filling effect for the SE yield, as shown in Figure 5-5 (b). The SASJ data contains the elements (Al, Ni or Cu, Ag, Pt) showing peak SE yield for each atomic shell corresponding to the maximum mass densities (refer to Figure 3-7) for the elements observed. The SE yields measured on the PHI 680 SAN, though sparse, follow the same trend.

The BSE yields for these 8 elements vary with beam energy in the range 0.8-3 keV and are shown in Figure 5-6 (a). Following the same rules as the SASJ data, the BSE yields increase with beam energy for $Z > 29$, are constant around atomic number 20 and decrease for Si.

Since BSEs have relatively high energies and are therefore less sensitive to measuring conditions, the experimental BSE yields are consistent and well documented. Accordingly, several fitting formulas accurately predict the BSE yield η as a function of atomic number Z and beam energy E_b at normal incidence. According to Neubert and Rogaschewski [137] (best fit 1):

$$\eta(Z,E_b) = (-272.5 + 168.6Z - 1.925Z^2 + 0.008225Z^3) \times 10^{-4}\left[1 + (0.2043 - 0.6543Z^{-0.3})\ln(E_b/20)\right] \quad (5\text{-}8)$$

And the expression given by Hunger and Küchler [138] (best fit 2) is:

$$\eta(Z,E_b) = E_b{}^{m(Z)}C(Z) \quad (5\text{-}9)$$

where

$$m(Z) = 0.1382 - \frac{0.9211}{Z^{0.5}} \quad (5\text{-}10)$$

and

$$C(Z) = 0.1904 - 0.2236\ln Z + 0.1292(\ln Z)^2 - 0.01491(\ln Z)^3 \quad (5\text{-}11)$$

In the expressions above, E_b is expressed in keV.

The experimental BSE yield data under various beam energies are listed in Table 5-3.

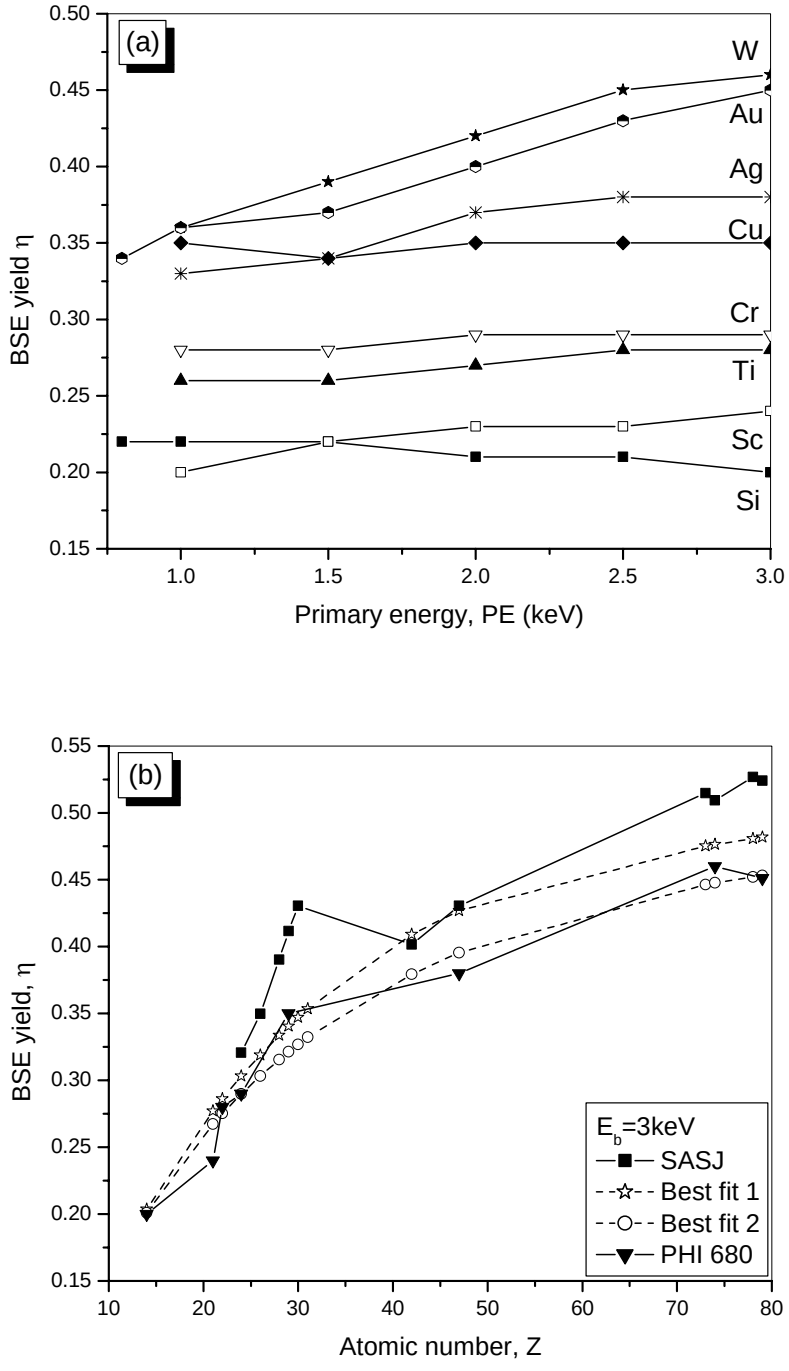

Figure 5-6: (a) Measured BSE yields on PHI 680 as a function of beam energy. (b) Comparison of BSE yields at beam energy of 3 keV of SASJ and measurement on PHI 680 with the data of best fit 1 by expression of Neubert and Rogaschewski [137] and best fit 2 of Hunger and Küchler [138].

Table 5-3: A list of the BSE yields measured on PHI 680 SAN under various beam energies, the SASJ yields, and two best fits [137, 138] for beam energy of 3keV.

Element	*Z*	*Measurements on PHI 680*					*SASJ*	*Fit 1*	*Fit 2*
Beam energy (keV)		*1.0*	*1.5*	*2.0*	*2.5*	*3.0*	*3.0*	*3.0*	*3.0*
Si	14	0.222	0.22	0.21	0.21	0.20	0.11	0.2	0.20
Sc	21	0.20	0.22	0.23	0.23	0.24		0.28	0.27
Ti	22	0.26	0.26	0.27	0.28	0.28		0.29	0.28
Cr	24	0.28	0.28	0.29	0.29	0.29	0.32	0.3	0.29
Fe	26						0.35	0.32	0.3
Ni	28						0.39	0.33	0.32
Cu	29	0.35	0.34	0.35	0.35	0.35	0.41	0.34	0.32
Zn	30						0.43	0.35	0.33
Ga	31							0.35	0.33
Mo	42						0.4	0.41	0.38
Ag	47	0.33	0.34	0.37	0.38	0.38	0.43	0.43	0.4
Ta	73						0.51	0.48	0.45
W	74	0.36	0.39	0.42	0.45	0.46	0.51	0.48	0.45
Pt	78						0.53	0.48	0.45
Au	79	0.358	0.366	0.398	0.4341	0.45	0.52	0.48	0.45

Two sets of the best-fits and the SASJ along with our measured BSE yields at 3 keV are plotted as a function of atomic number in Figure 5-6(b). Although the SASJ BSE yields do not exactly agree with the best fits, their values are the same scale as the larger set of the fits by Neubert and Rogaschewski [137]. Again, our measurements are smaller, and scatter evenly on both sides of the other best fitting trend curve. The descriptions above demonstrate that: (1) the yield calculation method developed and the CMA transmission efficiency estimated for the SASJ system are correct; (2) the SASJ AES instrument has full collection efficiency for the high energy BSE; and (3) the intensity-energy calibration applied to the PHI 680 SAN was successful.

5.4 Experimental results for binary alloys

Measurements on binary alloys were taken for Cr-W and Cu-Au alloys. Cr-W was chosen because the two components have the biggest discrepancy in both the peak SE yield δ^m and corresponding primary energy E_{PE}^m values in the optimized data ($\delta^m = 1.8$ and $E_{PE}^m = 0.6keV$ for Cr, $\delta^m = 1.06$ and $E_{PE}^m = 0.25keV$ for W). The elemental measurements above also showed that Cr and W have different SE spectra and yield profiles. In addition the big difference between the atomic numbers (Z=24 and Z=74) of

these two elements should result in a noticeable difference in the BSE yield. In a word, the Cr-W alloys should have the most obvious variance in electron emission in terms of chemical composition. The Au-Cu alloys were chosen as a test sample because Au and Cu are both royal metals that are not easily oxidized. In addition, the Au-Cu alloy is a very uniform solid solution so the sample will be chemically homogeneous. And the same as the Cr-W alloy, Cu (Z=29) and Au (Z=79) have very different atomic numbers.

The Cr-W and Cu-Au alloy samples were prepared by co-sputtering of the two elements starting from two ends of a piece of polished silicon wafer. Samples prepared this way have mirror-like smooth surfaces and therefore have little any topographical characteristic. The deposited alloys have smooth composition gradient from one end of the Si wafer to the other. The thickness for the Cr-W coating layer is 50 nm and for Cu-Au, 400 nm. Both of them are thicker than 1/3 of the beam ranges (the Bethe range for Cr, Cu, W and Au are 445 nm, 358 nm, 165 nm and 166 nm respectively at e-beam energy of $10\,keV$). This guaranteed that no electron signals from the Si substrate would emit contributing to the spectra collected.

No pretreatment was applied to the samples before inserting them into the UHV chamber. The samples were mounted and sputter cleaned using the same parameters that applied to the elemental samples. The analyzing points were considered on a line from one end of the wafer to the other and were at equal distance to each other. Sample compositions were automatically analyzed by the PHI 680 SAN by comparing the differentiate Auger signals to the sensitivity factor database of Physical Electronics [123].

5.4.1 Cr-W alloys

The compositions of the analyzed Cr-W alloys were $W_{96}Cr_4$, $W_{93}Cr_7$, $W_{88}Cr_{12}$, $W_{69}Cr_{31}$, $W_{56}Cr_{44}$, and $W_{93}Cr_7$. Almost pure W was obtained on one end of the wafer while pure Cr was unfortunately not available on the wafer. Measurements were done for beam energies of 0.4, 0.6, 0.8, 1.0, 1.5, 2.0, 2.5, 3.0, 5.0, and $10\,keV$. SE yields are calculated for all beam energies and BSE yields are available for $E_b < 3keV$. SE yields data for beam energies less than $1\,keV$ are noisy and thus are not presented. Data for pure Cr is borrowed from the elemental measurements in section 5.3 in the following analysis.

δ as a function of E_b for the Cr-W alloys have similar profile. They have almost the same maximum value $\delta^m = 0.4$ at about beam energy $E_b = 0.6keV$. No obvious variation with alloy composition is observed on the $\delta \sim E_b$ profiles. Both of the BSE and SE yields almost linearly increase with atomic percent of W as shown in Figure 5-7 (a) and (b). The linear increase of BSE yields with atomic percent of the heavy element in a binary alloy has been proved by the Monte Carlo simulations [18]. The SE yields, though scattered, have an obvious trend of linear increase with atomic percent of W in Cr-W alloys as illustrated by our experiment (Figure 5-7 (b)).

Figure 5-8 shows the calibrated SE spectra of Cr-W alloy for beam energy of 5 keV. To strengthen details of the spectral profile, the spectral intensity is expressed in the form of $N(E) \cdot E$ (cps). In Figure 5-8 (a) the spectra are normalized to their respective maximum for easier comparison on the spectral shape. W and Cr both have SE peaks at about 10 eV. Cr has much wider SE spectrum than W due to the MVV Auger peak (34 eV) superimposed on the cascading SE background. In all the alloys analyzed, only $Cr_{93}W_7$ resembles the Cr MVV peak. All the other alloys for which W is their main component have SE spectral profiles very similar to that of W. The Cr MVV Auger peaks are almost on the same energy ($34\,eV$) for alloy $Cr_{93}W_7$ and pure Cr. No obvious chemical shift is observed though their valence electron density should be different.

Similar linear relationship can be found between SE spectra and alloy compositions. Comparisons of the synthesized SE spectra of the alloys according to their atomic compositions in the form of:

$$N(E)_{Cr_xW_{1-x}} = xN(E)_{Cr} + (1-x)N(E)_W,\ (0 \le x \le 1) \qquad (5\text{-}12)$$

with the measurements are illustrated in Figure 5-8 (b) and (c). The synthesized spectra are represented in dashed curves and the measurements in solid lines.

As shown in Figure 5-8 (b) the synthesized spectra for Cr_7 W_{93} and $Cr_{31}W_{69}$ consistently agree with the measurements in terms of spectrum shape. Small discrepancies in the spectrum intensities (measured intensity for Cr_7W_{93} is 5% lower and $Cr_{31}W_{69}$ is 7% higher than the synthesized ones) are tolerable considering on the

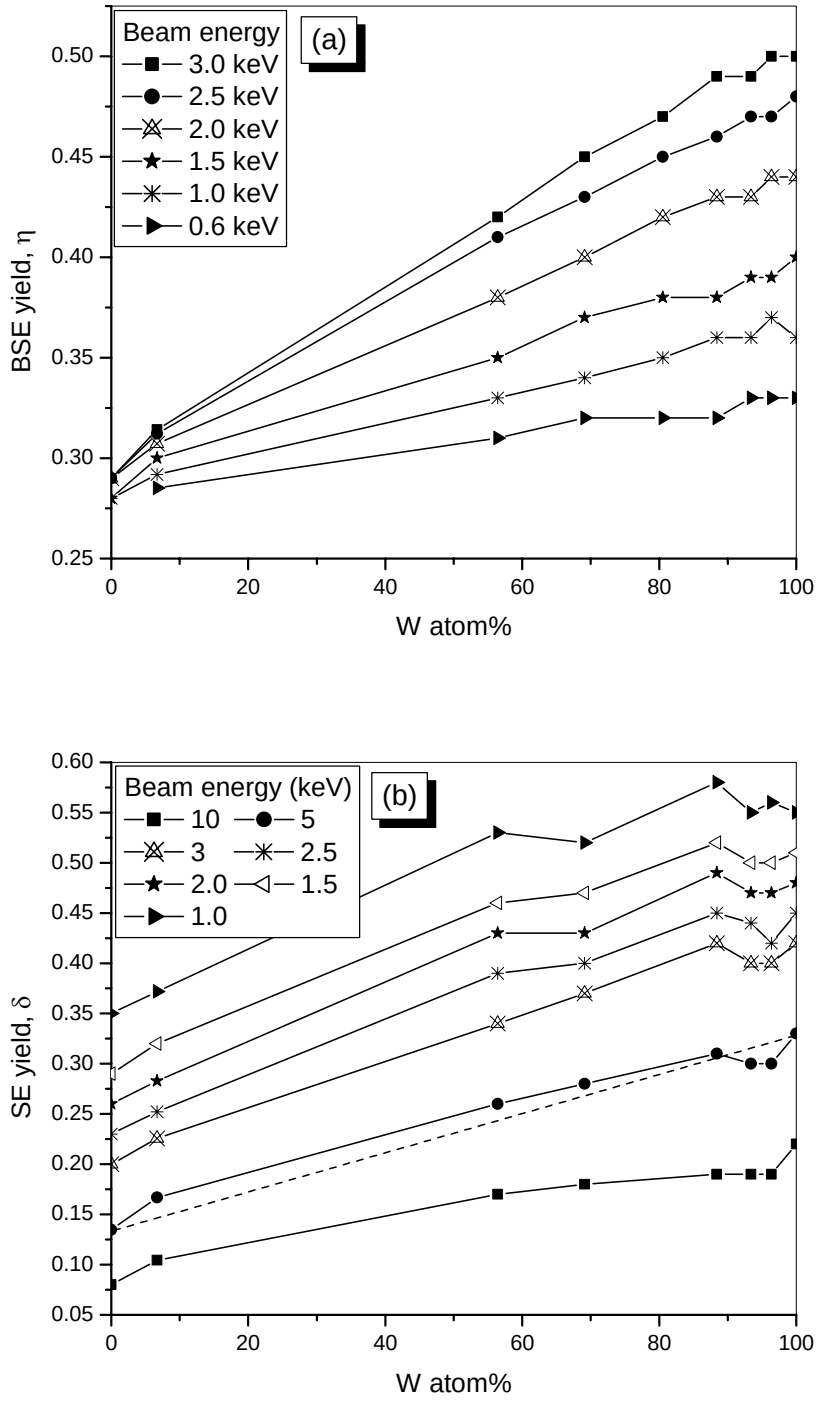

Figure 5-7: The variation of yields with element gradient in the Cr-W binary alloys. (a) BSE yields linearly increase with W atomic percent. (b) SE yields almost linearly increases with W atomic percent. Dashed line represents linear relationship.

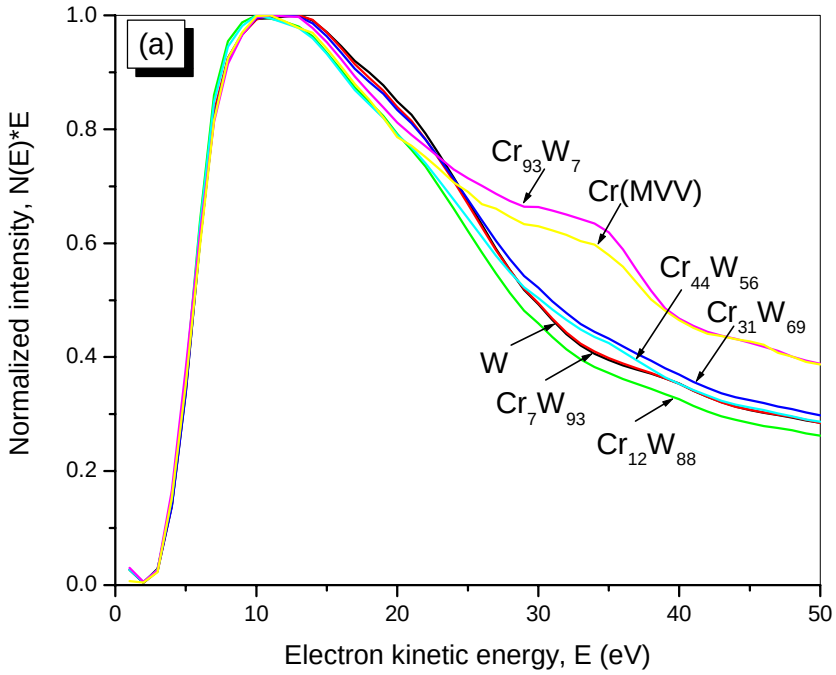
(a)
Normalized intensity, N(E)*E
Electron kinetic energy, E (eV)
Cr93W7
Cr(MVV)
Cr44W56
Cr31W69
W
Cr7W93
Cr12W88

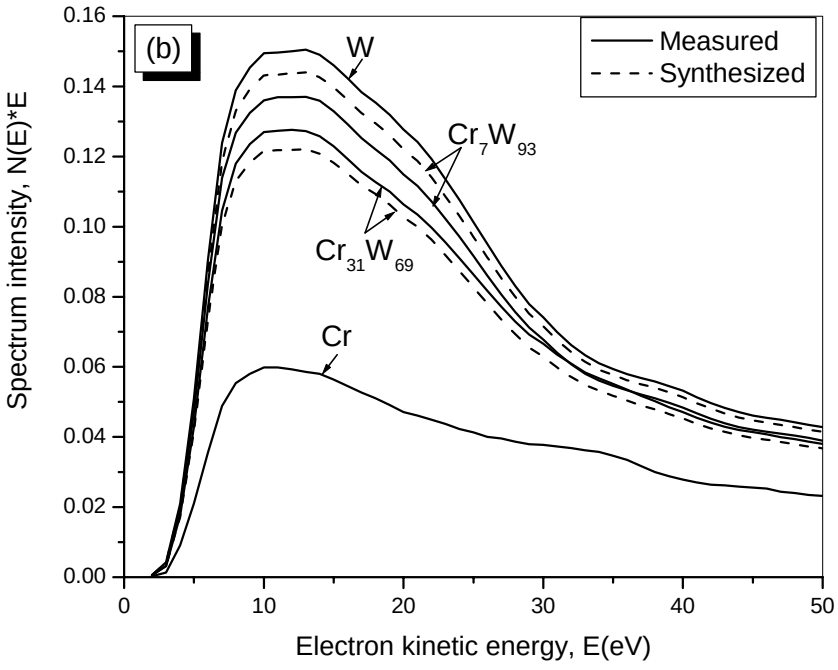
(b)
Measured
Synthesized
Spectrum intensity, N(E)*E
Electron kinetic energy, E(eV)
W
Cr7W93
Cr31W69
Cr

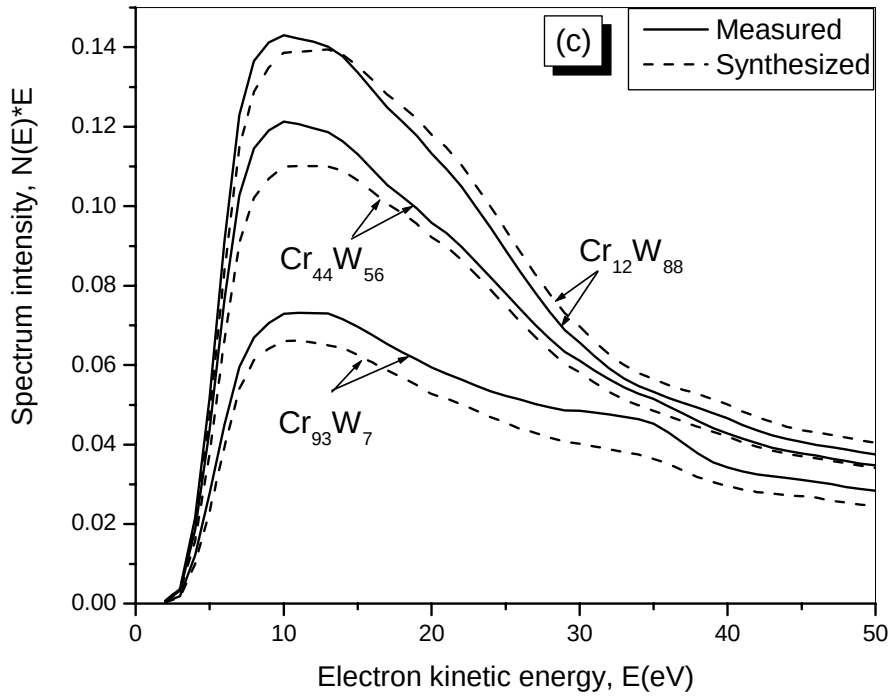

Figure 5-8: SE spectra of the Cr-W alloys under beam energy of 5 keV. (a) The spectra for all compositions analyzed normalized to their respective maximum. (b) Comparison of pure W, Cr and two composiitons in the middle demonstrates linear relationship with composition. Synthesized spectra consistently agree with the measurements. (c) The shapes of other 3 measurements agree with the synthesized spectra.

affectability of low energy secondaries to magnetic and electric fields and the difficulty existed in sample alignment. The measured spectra of Cr_7 W_{93} and $Cr_{31}W_{69}$ cross at about $31\,eV$, but they both have high energy tails parallel to that of the synthesized ones. The phenomenon that most of the alloy spectra resemble that of W thus can be explained by the linear combination theory since the spectrum intensity of W is predominately higher, almost 2-3 times that of the other composition, Cr. Comparison of the other 3 measurements with the synthesized ones (Figure 5-8(c)) also shows good agreement on spectrum shape, except that discrepancy in intensity is bigger and cross of the two spectra happens for one of the alloys ($Cr_{12}W_{88}$). Since SE spectra are not a function of beam energy, it can be concluded that this linear relationship can be applied to other energies.

Ichimura et al [139] found that the BSE spectra in the range of 40~1000 eV for Cu-Au alloys under beam energy of 10 keV were a linear combination of the elemental spectra of Cu and Au. They concluded that the linear relationship was originated form the similar slope of the BSE spectra for Cu and Au element. Our experiment proves that the SE spectra of Cr-W alloys are also linear combinations of the elemental ones, though Cr and W do not have similar SE spectral profile. There is currently no physical model to prove that Cr and W have similar electron scattering and cascading mechanisms except that these two elements belong to the same element group. An examination on the spectra (Figure 5-8 (a)) shows though the SE spectrum of Cr is different from that of W for E>20 eV due to the strong Cr MVV Auger transition, these two spectra almost overlaps to each other on the lower energy range where the main SE peak located. This phenomenon might be the evidence of similar SE generating and escaping behaviors between Cr and W. As a result both SE yields and the spectra have linear combination behavior.

The effect of surface cleanness on SE spectra is also analyzed in this experiment. In Figure 5-9, the difference of the sputter-cleaned SE spectra (normalized to their beam currents) from that of the as-received spectra (normalized to their beam currents too) after normalizing to their respective maximum are plotted for 3 alloys (W_7Cr_{93}, $W_{56}Cr_{44}$, $W_{69}Cr_{31}$) and element W. Neither spectra before nor after clean are calibrated by the

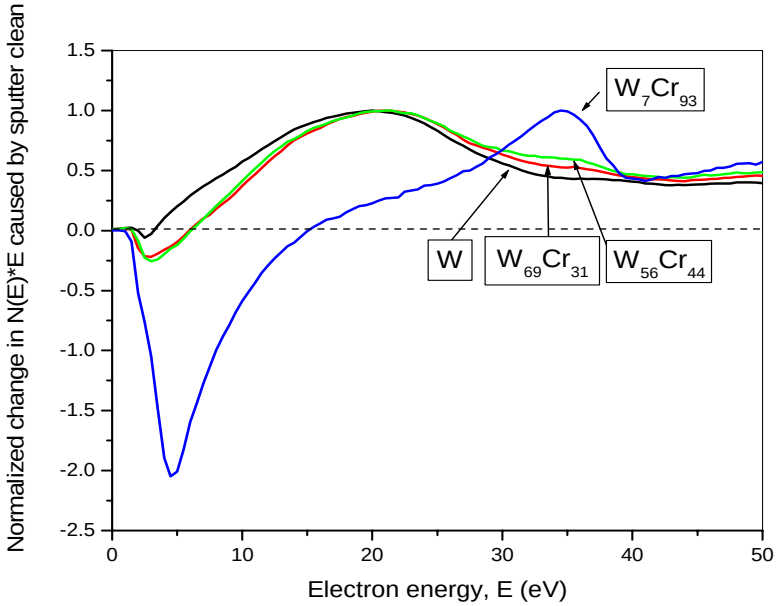

Figure 5-9: Normalized change in SE spectral intensity as a result of sputter clean applied on samples. It is calculated by subtracting spectra of the as-received samples from that of the cleaned. The differences are then normalized to their respective maximum. Spectra are collected under beam energy of 5 keV.

SASJ references in order to avoid mismatch that could be caused by energy realignment. The spectrum of W_7Cr_{93} can be deemed as that of pure Cr since they are very similar as illustrated in Figure 5-8 (a). Changes of SE spectra for alloys with W% larger than 80% overlap to that of pure W and thus are not plotted. It is shown that sputter clean has removed the contamination layers by reducing the SE signal around $5\,eV$ (spectral change is negative in this part), especially for the alloy (W_7Cr_{93}) with high concentration of easily oxidized element Cr. Removing of the contamination layers in turn has eased emission of secondaries of higher energies. Intensities for the Cr MVV Auger peak with small mean free path have been increased significantly. The higher the concentration of Cr, the more obvious improvement on the Auger signal can be brought out by the sputter clean.

5.4.2 Cu-Au alloys

The compositions of the Cu-Au alloys analyzed are $Cu_{40}Au_{60}$, $Cu_{50}Au_{50}$, $Cu_{70}Au_{30}$, and $Cu_{80}Au_{20}$, very linear with spatial positions that are picked from the wafer. Measurements were taken for beam energies ranging from $0.11\,keV$ up to $10\,keV$. This set of measurements was made when the PHI 680 SAN was less thoroughly calibrated and the MCP multiplier voltage applied was 2100 V, therefore the data is a little noisier. Both of the SE and BSE yields measured for the pure Au and Cu sample are either too low due to improper sample alignment or too high due to severe surface roughing, thus they could not be analyzed together with the alloys. It is not surprising that the SE spectra for the Cu-Au alloys have very similar profiles (Figure 5-10) since the spectra for pure Cu and Au almost overlap to each other (Figure 5-10 (a)). This in turn can explain the linear relationship of the SE and BSE yields with sample composition (Figure 5-11).

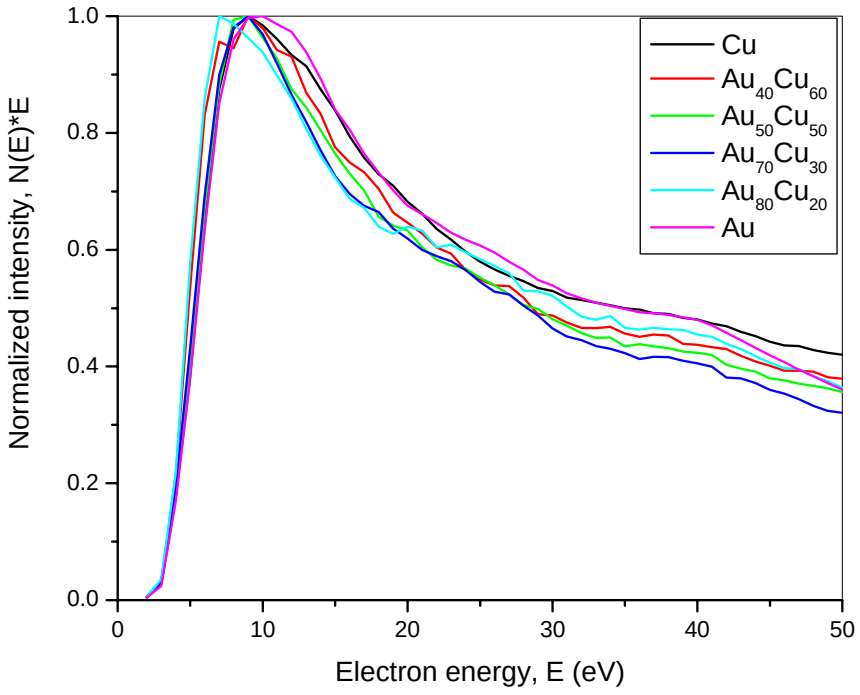

Figure 5-10: Normalized SE spectra of the Cu-Au alloys and pure Cu and Au under beam energy of 5 keV. The spectra are in the form of N(E)*E.

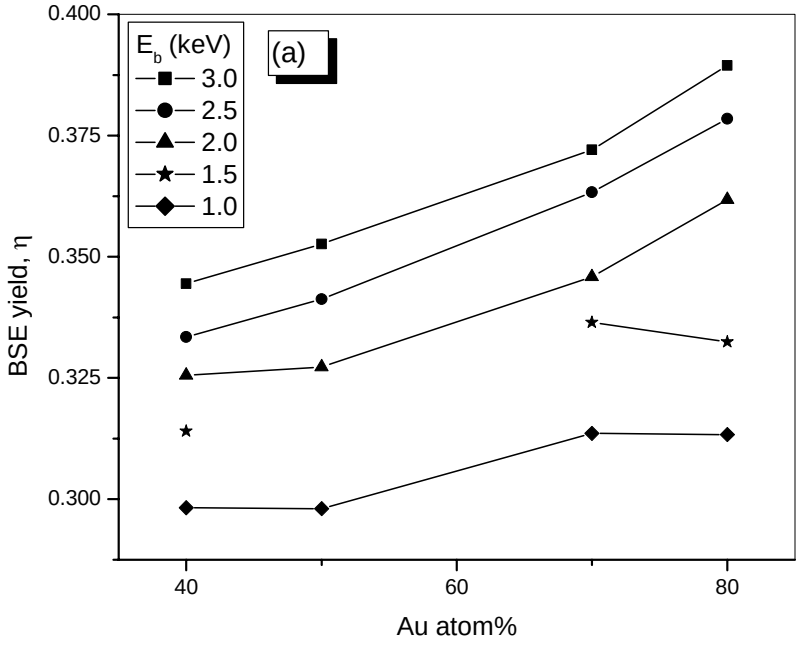

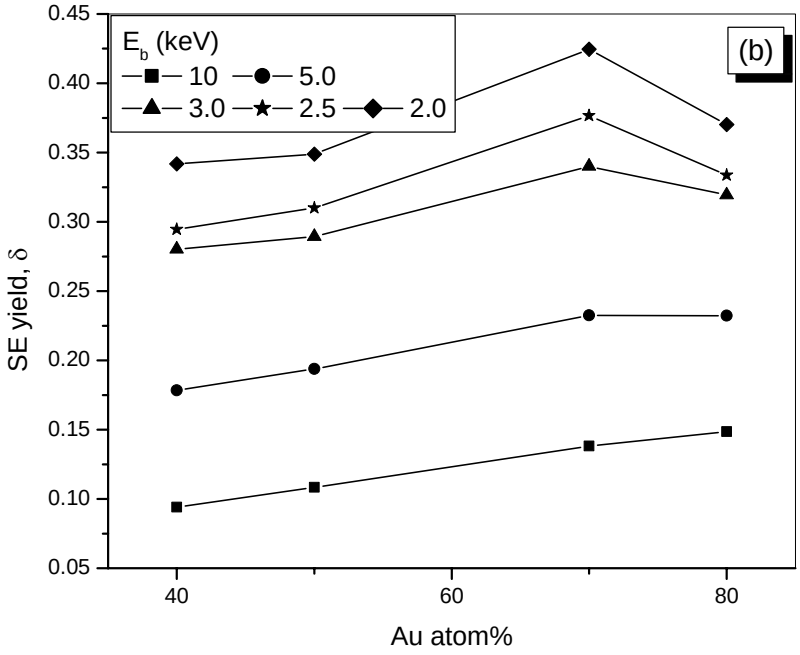

Figure 5-11: The variation of yields with element gradient in the Cu-Au binary alloys. (a) BSE yield linearly increases with Au atomic percent. (b) SE yield almost linearly increases with Au atomic percent.

5.5 Conclusions

Electron emission yields can be calculated from the calibrated AES spectra by normalizing areas under the spectra to the beam currents. BSE yields measured this way are very consistent with experimental measurements by other methods. SE yields calculated from the calibrated spectra are only about 50% of the optimized values. This is originated from the low efficiency for the SEs of the SASJ AES instrument that was used for collecting the reference spectra. The assumption of the cosine law on the angular distribution of the SE emission may have also caused error. Though the values are lower than expected, the systematic SE yields measured through AES spectra have all other characteristics such as following the universal curve and demonstrating atomic shell filling effect.

The SE and BSE yields for both Cr-W and Cu-Au alloys measured have linear relationship with atomic concentration of one element. A study proved that SE spectra of Cr-W alloys are linear combinations of the elemental spectra. Cr and W, as well as Cu and Au have similar spectral profiles in part or in the whole SE energy range, which may be the proof that these two sets of elements have similar SE production mechanisms, and as a result, the SE yields are linear with compositions.

6. Chapter Ⅵ: Summary and future work

Secondary electron yield is an important parameter for both explaining SEM images and evaluating models on electron-solid interactions. Study of the low energy secondaries has started since the beginning of the last century and has resulted in a lot of physical and simulation models and stacks of experimental data. But until today, satisfactorily models are in need to explain or predict some behavior of the secondaries; experimental database on the SE yield is neither consistent not complete. Profound studies on both theoretical models and experimental measurements are urgently needed in the field of microscopy and microanalysis.

The optimization on the SE yield database reduced scattering of the experimental measurements and provided valuable reference of optimized data for 44 elements. In addition, it indicated that the SE yields and some parameters describing the SE emission process (such as peak yield δ^m, corresponding primary energy E_{PE}^m, mean excitation energy ε, and mean attenuation length λ) followed an atomic shell filling effect when they are expressed as a function of atomic number, very similar to the variation trend of the mass density. To obtain more profound understanding on the SE yield property and the SE production process, a novel measurement method through the AES spectra was initiated and systematic measurements were taken on both elements and binary alloy sample Cr-W and Cu-Au.

The novel measurements were carried out on the PHI 680 SAN system. It is superior to the traditional experimental methods in many ways and is suited for analyzing samples with more complicated compositions. Before integrating areas under the AES spectra to obtain the SE, BSE yields, spectral intensities and energies need to be calibrated to correct the collection efficiency loss that is specific to each instrument. The response function $Q(E)$ of the PHI 680 is composed of CMA transmission function $T(E)$, the MCP detection efficiency $D(E)$ and the dead time effect of the electronic counting system, of which $T(E)$ makes the spectral intensity linearly increase with electron kinetic energy and $D(E)$ contributes most to the non-uniformity of the collection efficiency. The

calculated $Q(E)$ of the PHI 680 based on the reference spectra of SASJ and NPL agreed well to each other. SE spectra calibrated by this $Q(E)$ have much higher intensity for both the low energy secondaries and high energy BSEs and have sharper SE peak at around $10\,eV$.

Measurements were taken on several elements and two binary alloys: Cr-W and Cu-Au. BSE yields measured by this way on the elements agree well with the best estimated data. SE yields are only half of optimized data, which is most probably due to the low collection efficiency for SE of the SASJ instrument that is used to obtain the reference spectra. The measured SE yields for the elements demonstrated atomic shell filling effect. Both the SE and BSE yields of the Cr-W and Cu-Au alloys demonstrated linear relationship with atomic concentration of one component. Spectral analysis proved that the SE spectra of the alloys were linear combinations of the elemental spectra.

Since the absolute spectrum intensity calibration involves many steps of after processing and is greatly relied on the precision of the reference spectra, distortion on the calibrated SE spectra is unavoidable. Alignment of the PHI 680 SAN instrument is not easily especially when it comes to measure the low energy SE spectrum. Dr. Ronald E. Negri, senior R&D scientist in PHI electronics expressed it as follows [120]:

"…Overall…the 680 analyzer is not a good choice as a CMA for making absolute intensity measurement of secondaries (0-50eV). Rather, it is designed for maximum spatial resolution (with magnetic objective lens) and for high sensitivity (with multi-channel detector).

"A better choice would be PHI's 25-130 'spectroscopy' CMA which is the basis for the 650 and 4300 Auger instruments. First, the 25-130 use an electric e-gun objective lens whereas the 680 employs a magnetic one. The magnetic objective has stray magnetic fields that significantly reduce the sensitivity for secondaries. Second, the 25-130 has a spherical-sector post-filter after the CMA to eliminate scattered electrons. There is no easy way to eliminate these scattered electrons in the 680 multi-channel detector…Fourth, the 25-130 uses a channeltron detector rather HOT MCP's, so the detector has a well characterized plateau with applied voltage. Fifth, the 25-130 has variable apertures, the smallest corresponding to 0.3% energy resolution, making it easy using peak position to

set sample height reproducibly (typically within 0.1 mm). Sixth, the 25-130 has a low dark count rate because there is no negative high-voltage electrodes right in front of the detector as in the 680."

In the future for reproducible measurement, besides shifting to the 25-130 typed CMA, we can try to reduce the effect of the surface roughness by increasing the Ar ion sputtering angle so that most obvious topography can be smeared off. Measurements can be taken on elements with more continuous atomic numbers to reveal and prove the variation trends of the SE emission characteristics. To further test the linearity of the SE yields and spectra with the atomic compositions in the binary alloys, samples can be designed to be composed two elements that have very different atomic numbers and spectral shapes. Elements in different group can be a good choice, such as combination of Ti (Z=22) or Cr (Z=24) and Ag (Z=47) or Au (Z=79), or Cu (Z=29) and Mo (Z=42) or W (Z=74).

References

1. Joy D.C., Prasad M.S., and Meyer H.M.III, *Experimental secondary electron spectra under SEM conditions.* J. Microscopy, 2004. **215**(Secondary electron spectra under SEM conditions): p. 77-85.
2. Detrich W. and Seiler H., Energieverteilung von elektronrn, die durch ionen und elektronen in durchstrahlung dunner folien ausgel?st werden. Z. Phys., 1960. **157**: p. 567-585.
3. Luo S. and Joy D. C., *Monte Carlo calculations of secondary electron emission.* Scanning Microscopy Supplement, 1990. **4**: p. 127-146.
4. Chung M.S. and Everhart T.E., Simple calculation of energy distribution of low-energy secondary electrons emitted from metals under electron bombardment. J. Appl. Phys., 1974. **45**(2): p. 707-709.
5. Nickles N., Davies R.E., and Dennison J.R., *Applications of secondary electron energy- and angular-distribution to spacecraft charging.* 6th Spacecraft Charging Technology Conference, 2000: p. 275-280.
6. Henke B.L., Liesegang J., and Smith S.D., *Soft-x-ray induced secondary electron emission from semiconductors and insulators.* Phys. Rev. B, 1979. **19**: p. 3004-3021.
7. Seiler H., Secondary electron emission in the scanning electron microscope. J. Appl. Phys.,, 1983. **54**(11): p. R1-R18.
8. Jonker J.L.H., *Secondary electron emission from solids.* Philips Resaerch Repts., 1957. **12**: p. 249-3000.
9. Kanaya K. and Kawakatsu H., *Secondary electron rmission due to primary and backscattered electrons.* J. Phys. D: Appl. Phys., 1972. **10**: p. 1727-1742.
10. Koshikawa T. and Shimizu R., *A Monte Carlo calculation of low-energy secondary electron emission from metals.* J. Phys. D: Appl. Phys., 1974. **7**: p. 1303-1315.
11. Reimer L., *Image Formation in Low-Voltage Scanning ELectron Microscopy*. 1993, Bellingham, WA: SPIE Optical Engineering Press.
12. Seiler H., *Some problems if secondary electron emission.* Z. Phys., 1967. **22**: p. 249-263.
13. Goldstein J. I., et al., Scanning electron microscopy and x-ray microanalysis: a textbook for biologists, materials scientists, and geologists. 2nd ed. 1992, New York: Plenum Press.
14. Wells O.C., The construction of a SEM and its application to the study of fibers. 1957, Ph.D. dissertation, Cambridge University.
15. Everhart T.E. and Chung M.S., *Idealized spatial emission distribution of secondary electrons.* J. Appl. Phys., 1972. **43**(9): p. 3707-3711.
16. Everhart T.E., *Contrast formation in the SEM*. 1958, Ph.D. dissertation, Cambridge University.
17. Hasselbach F. and Rieke U. Spatial distribution of secondaries released by backscattered electrons in silicon and gold for 20-70keV primary energy. in 10th International Congress on Electron Microscopy. 1982. Hamburg.
18. Joy D.C., *Monte Carlo Modeling for Electron Microscopy and Microanalysis*. 1995, New York, Oxford: Oxford University Press.

19. Joy D.C. and Joy C.S., *Low voltage scanning electron microscopy.* Micron, 1996. **27**(3-4): p. 247-263.
20. Joy D.C., Contrast in high-resolution scanning electron microscope images. J. Microscopy, 1991. **161**: p. 343-355.
21. Shimizu R., Secondary electron yield with primary electron beam of kilo-electron-volts. J. Appl. Phys., 1974. **45**(5): p. 2107-2111.
22. Luo S. and Joy D.C., *Monte Carlo calculations of secondary electron emission.* Scanning Microscopy, 1988. **2**(4): p. 1901-1915.
23. Dekker A.J., *Solid State Physics*. 1957, Englewood Cliffs, N.J.: Prentice-Hall, Inc.
24. Vink T.J., et al., Materials with a high secondary-electron yield for use in plasma display. Appl. Phys. Lett., 2002. **80**(12): p. 2216-2218.
25. Kanter H., Energy dissipation and secondary electron emission in solids. Phys. Rev., 1961. **121**(3): p. 677-681.
26. Ono S. and Kanaya K., The energy dependence of secondary emission based on the range-energy retardation power formula. J. Phys. D: Appl. Phys., 1979. **12**: p. 619-634.
27. Cazaux J., Recent developments and new strategies in scanning electron microscopy. J. Microsc., 2005. **217**: p. 16-35.
28. Mohan A., Khanna N., and Joy D.C., Secondary electron imaging in the variable pressure scanning electron microscope. Scanning, 1998. **20**: p. 436-441.
29. Durkin R. and Shah J. S., Amplification and noise in high-pressure scanning electron microscopy. J. Microsc., 1993. **169**: p. 33-51.
30. Joy D.C., *Charge control during photomask critical dimension (CD) metrology*. 2004, International SEMATECH, technology transfer #03114452B-ENG.
31. Bethe H.A., *On the theory of secondary emission.* Phys. Rev., 1941. **59**: p. 940-949.
32. Sallow H., Phys. Z., 1940. **41**: p. 434.
33. Baroody E.M., *A theory of secondary electron emission from metals.* Phys. Rev., 1950. **78**(6): p. 780-787.
34. Jonker J.L.H., Philips Resaerch Repts., 1952. **7**: p. 1.
35. Bruining H., physics and Applications of Secondary Electron Emission. 1954, London: Pergamon Press LTD.
36. Wolff P.A., *Theory of secondary electron cascade in metals.* Phys. Rev.,, 1954. **95**(1): p. 56-66.
37. Cailler M. and Ganachaud J.P., J. Physique, 1972. **33**: p. 903.
38. Schou J., Transport theory for kinetic emission of secondary electrons from solids. Phys. Rev. B, 1980. **22**: p. 2141-2174.
39. Schou J., Secondary electron emission from solids by electron and proton impact. Scanning Microscopy, 1988. **2**: p. 607-632.
40. Devooght J., Dubus A., and Dehaes J. C., Improved age-diffusion model for low-energy electron transport in solids. I. Theory. Phys. Rev. B, 1987. **36**: p. 5093-5109.
41. Newbury D.E. and Myklebust R.L., *Analytical Electron Microscopy*, ed. G. R.H. 1981, San Francisco: San Francisco Press. 91.

42. Bishop H.E., Use of Monte Carlo Calculations in Electron Probe Microanalysis and Scanning Electron Microscopy. 1976. Washington D.C.: U.S. Department of Commerce, National Bureau of Standards., ed. Heinrich K.F.J., Newbury D.E., and Yakowits H. 1976: NBS Special Publication #460. 9.
43. Mott N.F., *The scattering of fast electrons by atomic nuclei.* Proc. R. Soc. A, 1929. **124**: p. 425-442.
44. Reimer L. and Krefting E.R., *Use of Monte Carlo Calculations in Electron Probe Microanalysis and Scanning Electron Microscopy*, ed. Heinrich K.F.J., Newbury D.E., and Y. H. 1976: NBS Special Publication #460. 45-95.
45. Yamazaki Y., *Ph.D Thesis.* 1977, Osaka University. p. 140-153.
46. Ding Z.-J. and Shimizu R., A Monte Carlo modeling of electron interaction with solids including cascade secondary electron production. Scanning, 1996. **18**: p. 92-113.
47. Kuhr J.-Ch. and Fitting H.-J., *Monte Carlo simulation of electron emission from solids.* J. Electron Spectrosc.Relat. Phenom., 1999. **105**: p. 257-273.
48. Ding Z.-J. and Shimizu R., *Inelastic collisions of kV electrons in solids.* Surf. Sci., 1989. **222**: p. 313-331.
49. Ashley J.C., Energy-loss probabilities for electrons, positrons, and protons in condensed matter. J. Appl. Phys., 1991. **69**(2): p. 674-678.
50. Tanuma S., Powell C.J., and Penn D.R., Calculations of electorn inelastic mean free paths. II. Data for 27 elements over the 50-2000 eV range. Surf. Interface Anal., 1991. **17**(13): p. 911-926.
51. Seah M.P. and Dench W.A., Quantitative electron spectroscopy of surface: a standars data base for electron inelastic mean free paths in solids. Surf. Interface Anal., 1979. **1**: p. 2-11.
52. Bethe H.A., Theory of passage of swift corpuscular rays through matter. Ann. Phys., 1930. **5**: p. 235-256.
53. Ritchie R.H., et al., Adv. Radiat. Roil., 1969. **3**: p. 1-28.
54. Shimizu R. and Ding Z.-J., *Microbeam Analysis*, ed. Michael J.R. and Ingram P. 1990, San Francisco: San Francisco Press. 6-16.
55. Shimizu R. and Ding Z.-J., *Monte Carlo modelling of electron-solid interactions.* Rep. Prog. Phys., 1992: p. 487-531.
56. Berger M.J. and Seltzer S.M., Studies in Penetration of Charged Particles in Matter, in Nuclear Science Series Report #39, Nas-NRC publication 1133. 1964: Washington D.C. p. 205.
57. Fitting H.-J., Phys. Status Solidi a, 1974. **26**: p. 525-535.
58. Rao-Sahib T.S. and Wittry D.B., *X-ray continuum from thick elemental targets for 10–50-keV electrons.* J. Appl. Phys., 1974. **45**: p. 5060-5068.
59. Joy D. C. and Luo S., Scanning, 1989. **11**: p. 176.
60. Powell C.J., Calculations of electron inelastic mean free paths from experimental optical data. Surf. Interface Anal., 1985. **7**: p. 263-274.
61. Penn D.R., Electron mean-free-path calculations using a model dielectric function. Phys. Rev. B,, 1987. **35**(2): p. 482-486.
62. Ding Z.-J. and Shimizu H., Monte Carlo study of backscattering and secondary electron generation. Surf. Sci., 1988. **197**: p. 539-554.

63. Kanaya K. and Okayama S., *Peneration and energy-loss theory of electrons in solid targets.* J. Phys. D.: Appl. Phys., 1972. **5**: p. 43-58.
64. Berger M.J., *Methods in Computationsl Physics*, ed. Alder B., Fernbath S., and Rotenberg M. Vol. 1. 1963, New York: Academic Press. 135-213.
65. Bishop H.E., *X-ray Optics and Microanalysis*, ed. Castaining R., Deschamps P., and Philibert J. 1965, Paris: Hermann. 112-119.
66. Shimizu R., Murata K., and Shinoda G., *X-ray Optics and Microanalysis*, ed. Castaining R., Deschamps P., and Philibert J. 1965, Paris: Hermann. 127-138.
67. Heinrich K.F.J., Newbury D.E., and Yakowits H. *Use of Monte Carlo Calculations in Electron Probe Microanalysis and Scanning Electron Microscopy*. 1976. Washington D.C.: U.S. Department of Commerce, National Bureau of Standards.
68. Rosler M. and Brauer W., Particle Induced Electron Emission I: Theory of Electron Emission from Nearly-Free-Electron Metals by Proton and Electron Bombardment, in Springer Tracts in Modern Physics, Hohler G., Editor. 1991, Springer-Verlag: Berlin Heidelberg.
69. Gryzinski M., *Two-particle collisions. I, II, III.* Phys. Rev., 1965. **138**(2A): p. 305-358.
70. Chung M.S. and Everhart T.E., Role of plasmon decay in secondary electron emission in the nearly-free-electron metals. Application to aluminum. Phys. Rev. B, 1977. **15**(10): p. 4699-4715.
71. Devooght J., et al., Particle Induced Electron Emission I: Theoretical Description of Secondary Electron Emission Induced by Electron or Ion Beam Impinging on Solids. Springer Tracts in Modern Physics, ed. Hohler G. Vol. 122. 1991, Berlin Heidelberg: Springer-Verlag.
72. Gries W.H. and Werner W., Take-off angle and film thickness dependences of the attenuation length of X-ray photoelectrons by a trajectory reversal method. Surf. Interface Anal., 1990. **16**(1-12): p. 149-153.
73. Werner W. and Gries W.H., Analytical expression describing the attenuation of Auger electrons and photoelectrons in solids. Surf. Interface Anal., 1991. **17**(10): p. 693-704.
74. Jablonski A., *Elastic scattering and quantification in AES and XPS.* Surf. Interface Anal., 1989. **14**(11): p. 659-685.
75. Murata K., Kyser D. F., and Ting C. H., *Monte Carlo simulation of fast secondary electron production in electron beam resists.* J. Appl. Phys., 1981. **52**(7): p. 4396-4405.
76. Ichimura S. and Shimizu R., *Backscattering correction for quantitative Auger analysis.* Surf. Sci., 1981. **112**(3): p. 386-408.
77. Evans R.D., *The Atomic Nucleus*. 1955, New York: McGraw Hill. p. 576.
78. Kyser D.F., *Spatial resolution limits in electron beam nanolithography.* J. Vac. Sci. Technol. B, 1983. **1**(4): p. 1391-1397.
79. Auday G., Guillot Ph., and Galy J., *Secondary emission of dielectrics used in plasma display.* J. Appl. Phys., 2000. **88**: p. 4871-4874.

80. Joy D.C., *A database of electron-solid interactions*. July 2004, <http://pciserver.bio.utk.edu/metrology/download/E-solid/database.doc>, UTK Metrology Group.
81. Young J.R., *Penetration of electrons in aluminum oxide films.* Phys. Rev., 1956. **103**(2): p. 292-293.
82. Lane R.O. and Zaffarano D.J., Transmission of 0-40 keV electron by thin films with application to beta-ray spectroscopy. Phys. Rev., 1954. **94**(4): p. 960-964.
83. Dionne G.F., Origin of secondary-electron-emission yield-curve parameters. J. Appl. Phys., 1975. **46**(8): p. 3347-3351.
84. Dionne G.F., Effects of secondary electron scattering on secondary emission yield curves. J. Appl. Phys., 1973. **44**(12): p. 5361-5364.
85. Joy D. C., A model for calculating secondary and backscattered electron yields. J. Microsc., 1987. **147**(1): p. 51-64.
86. *CRC Handbook of Chemistry and Physics*. 66 ed, ed. Weast R.C., Astle M.J., and Beyer W.H. Vol. E. 1985-1986, Boca Raton, FL: CRC press.
87. *Density Chart of the Elements - Periodic Table*. 2006, http://www.standnes.no/chemix/periodictable/density-chart-elements.htm, Chemistry Software.
88. Winter, M., *WebElements Periodic Table*. 2006, http://www.webelements.com/, The University of Sheffield and Webelements Ltd, UK.
89. Copeland P.L., Correlation between variation of secondary electron emission and atomic number. Phys. Rev., 1934. **46**(3): p. 167-168.
90. Sternglass E.J., *Secondary electron emission and atomic shell structure.* Phys. Rev., 1950. **80**: p. 925-926.
91. Hippler S., Hasselkamp D., and S. A., *The ion-induced electron yield as a function of the target material.* Nucl. Instrum. Meth. Phys. Res. B, 1988. **34**: p. 518-520.
92. Barut A.O., *The machanism of secondary electron emission.* Phys. Rev., 1954. **93**(5): p. 981-984.
93. Joy D.C., *A database on electron-solid interactions.* Scanning, 1995. **17**: p. 270-275.
94. Seiler H., *Secondary electron emission*. Electron Beam Interactions with Solids for Microscopy, Microanalysis & Microlithography, ed. Kyser D. F., et al. 1982, AMF O'Hare, IL: Scanning Electron Microscopy. 33-43.
95. Powell C.J., Erickson N.E., and Madey T.E., Results of a joint Auger.ESCA round robin sponsored by ASTM committee E-42 on surface analysis. Part II. Auger results. J. Electron Spectrosc.Relat. Phenom., 1982. **25**: p. 87-118.
96. Seah M.P. and Smith G.C., Quantitative AES: reducing error in measured analogue spectral intensities through control of the electron detector. Surf. Interface Anal., 1990. **15**: p. 701-704.
97. Seah M.P. and Smith G.C., Quantitative AES: calibration of spectrometers for true spectral measurements-results of a VAMAS round robin and recommendations for acquiring reference data banks. Surf. Interface Anal., 1990. **16**: p. 168-172.

98. Seah M.P. and Smith G.C., Quantitative AES and XPS: determination of the electron spectrometer transmission function and the detector sensitivity energy dependencies fot the production of true electron emission spectra in AES and XPS. Surf. Interface Anal., 1990. **15**(751-766).
99. Omhura T. and Shimizu R., *Analytical Electron Microscopy*, ed. Joy. D.C. 1987, CA: San Francisco Press. 325.
100. Seah M.P., *A system for the intensity calibration of electron spectrometers.* J. Electron Spectrosc.Relat. Phenom., 1995. **71**: p. 191-204.
101. Goto K., Sakakibara N., and Sakai Y., A novel cylindrical mirror analyzer for absolute measurements of Auger electron standard spectra. Microbeam Anal., 1993. **2**: p. 123-131.
102. Sar-EL H.Z., Cylindrical capacitor as an analyzer I: nonrelative part. Rev. Sci. Instrum., 1967. **38**(9): p. 1210-1216.
103. Sar-EL H.Z., *Criterion for comparing analyzers.* Rev. Sci. Instrum., 1970. **41**(4): p. 561-564.
104. Seah M.P., *Chapter 3: Electron and ion energy analysis*, in *Methods of surface analysis*, Walls J.M., Editor. 1989, Cambridge University Press: Cambridge [Cambridgeshire]; New York. p. 57-80.
105. Seah M.P. and Hunt C.P., Auger electron spectroscopy: method for the accurate measurement of signal and noise and a figure of merit for the performance of AES instrument sensitivity. Rev. Sci. Instrum., 1988. **59**(2): p. 217-227.
106. Keshi-Rahkonen O. and K. M.O., *Relativistic effects in the calibration of electrostatic electron analyzers. I. Toroidal analyzers.* J. Electron Spectrosc.Relat. Phenom., 1978. **13**(2): p. 107-113.
107. Goto K., *Standard Auger spectra taken with standard CMA.* J. Surf. Anal., 1995. **1**(162-165).
108. Sickafus E.N. and Holloway D.M., Specimen position effects on energy shifts and signal intensity in a sigle-stage cylindrical-mirror analyzer. Surf. Sci., 1975. **51**: p. 131-139.
109. Palmberg P.W., J. Vac. Sci. Technol., 1975. **12**: p. 379.
110. Seah M.P. and Smith G.C., AES: accurate intensity calibration of electron spectrometers-results of a BCR interlaboratory comparison co-sponsored by the VAMAS SCA TWP. Surf. Interface Anal., 1991. **17**: p. 855-874.
111. Geller J.D., *A novel CMA alignment technique for Auger spectroscopy.* Applications of Surf. Sci., 1984. **18**: p. 18-27.
112. Bakush T.A.El and Gomati M.M.El, *Internal scattering in a single pass cylindrical mirror analyses.* J. Electron Spectrosc.Relat. Phenom., 1995. **74**: p. 109-120.
113. Gomati M.M.El and Bakush T.A.El, *Source of internal scattering of electrons in a cylindrical mirror analyzer(CMA).* Surf. Interface Anal., 1996. **24**: p. 152-162.
114. Seah M.P., Scattering in electron spectrometers, diagnosis and avoidance. II. Cylindrical mirror analysers. Surf. Interface Anal., 1993. **20**: p. 876-890.
115. Yoshitake M. and Yoshihara K., Round robin on spectrometer transmission calibration for AES in the common data processing system. Surf. Interface Anal., 1997. **25**: p. 209-216.

116. Wiza J.L., *Microchannel plate detectors.* Nuclear Instrum. and Methods, 1979. **162**: p. 587-601.
117. *Microchannel plates*. 2006, http://imagine.gsfc.nasa.gov/docs/science/how_l2/microchannels.html.
118. Seah M.P., Channel electron multipliers: quantitative intensity measurement-efficiency, gain, linearity and bias effects. J. Electron Spectrosc.Relat. Phenom., 1990. **50**: p. 137-157.
119. Seah M.P., Lim C.S., and Tong K.L., Channel electron multiplication efficiencies: the effect of the pulse height distribution on spectrum shape in Auger electron spectroscopy. J. Electron Spectrosc.Relat. Phenom., 1989. **48**: p. 209-218.
120. Personal communication with Dr. Negri R. E. in PHI Electronics through Meyer H. M. in Jan 05, 2006.
121. Seah M.P. and Tosa M., *Linearity in electron counting and detection systems.* Surf. Interface Anal., 1992. **18**: p. 240-246.
122. Muller J.W., *Dead-time problems.* Nuclear Instrum. and Methods, 1973. **112**: p. 47-57.
123. Lawrence D.E., et al., *Handbook of Auger electron spectroscopy*. 2 ed. A reference book of standard data for identification and interpretation of Auger electron spectroscopy data. 1976, Eden Prairie, MN: Physical Electronics Division, Perkin-Elmer Corporation.
124. McGuire G.E., *Auger Electron Spectroscopy Reference Manual*. 1979, Plenum, New York.
125. Shiokawa Y., Isida T., and Hayashi Y., *Auger Electron Spectra Catalogue: A Data Collection of Elements*. 1979, Anelva, Tokyo.
126. Sekine T., et al., *Handbook of Auger Electron Spectroscopy*. 1982, JOEL, Tokyo.
127. Seah M.P., Data compilations: their use to improve measurement certainty in surface analysis by AES and XPS. Surf. Interface Anal., 1986. **9**: p. 85-98.
128. Seah M.P. and Gilmore I.S., High resolution digital Auger database of true spectra for Auger electron spectrodcopy intensities. J. Vac. Sci. Technol., 1996. **14**: p. 1401-1407.
129. Goto K., et al., *True Auger spectral shapes: a step to standars spectra.* Surf. Interface Anal., 1994. **22**: p. 75-78.
130. Seah M.P. and Gilmore I.S., Quantitative AES VIII: analysis of Auger electron intensities from elemental data in a digital Auger database. Surf. Interface Anal., 1998. **26**: p. 908-929.
131. Smith G.C. and Seah M.P., Quantitative AES: the establishment of a standard reference spectrum for the accurate determination of spectrometer transmission function. Surf. Interface Anal., 1988. **12**: p. 105-109.
132. Personal communication with Dr. Tanuma S. in Jan. 2005.
133. Goto K. and Takeichi Y., Carbon reference Auger electron spectra measured with a high-performance cylindrical mirror analyzer. J. Vac. Sci. Technol. A, 1996. **14**(3): p. 1408-1414.
134. Yoshihara K. and Yoshitake M., Sharing of Auger electron spectroscopy and x-ray photoelectron spectroscopy spectral data through the internet. J. Vac. Sci. Technol. B, 1998. **16**(3): p. 1388-1393.

135. Seah M.P. and Gilmore I.S., *AES: energy calibration of electron spectrometers. III-genaral calibration rules.* J. Electron Spectrosc.Relat. Phenom., 1997. **83**: p. 197-208.
136. Cumpson P.J. and Shawyer R.E., *NPL AES Intensity Calibration Software, A1 V2.0 (r27).* 1998, National Physical Lab.
137. Neubert G. and Rogaschewski S., Phys. Status Solidi A, 1980. **59**: p. 35.
138. Hunger H.-J. and Kuchler L., Phys. Status Solidi A, 1979. **56**: p. K45.
139. Ichimura S., et al., *Use of EN(E) spectra for quantitative AES analysis of Au-Cu alloys.* Surf. Interface Anal., 1988. **11**: p. 94-102.

Appendixes

Appendix 1: Table A-1: Dark count of the MCP in the PHI 680 SAN, Response function based on the SASJ reference spectra, and the intensity calibration template.

As-received spectrum		Correct Dead Time	**Dark Count**	Correct Dark Count	**Response Function**	True Spectrum	True Spectrum
		1*		2*			
Energy	Intensity	Intensity	**Intensity**	Intensity		intensity	intensity
E	$N_0(E)*E$	$N_1(E)*E$	**$N_2(E)*E$**	$N_3(E)*E$	**Q(E)**	N(E)*E	N(E)
eV	nps	nps	**nps**	nps	**cps/nA**	nA	nA/eV
0	0	0	15	0	0.00E+00		
5	0	0	0	0	7.47E+05		
10	0	0	0	0	3.37E+05		
15	0	0	0	0	3.98E+05		
20	0	0	20	-20	4.76E+05		
25	0	0	15	-15	5.26E+05		
30	0	0	20	-20	5.74E+05		
35	0	0	20	-20	6.27E+05		
40	0	0	35	-35	6.84E+05		
45	0	0	25	-25	7.65E+05		
50	0	0	55	-55	8.43E+05		
55	0	0	35	-35	9.19E+05		
60	0	0	60	-60	9.92E+05		
65	0	0	105	-105	1.06E+06		
70	0	0	70	-70	1.13E+06		
75	0	0	95	-95	1.20E+06		
80	0	0	75	-75	1.26E+06		
85	0	0	70	-70	1.32E+06		
90	0	0	100	-100	1.39E+06		
95	0	0	90	-90	1.44E+06		
100	0	0	100	-100	1.50E+06		
105	0	0	85	-85	1.55E+06		
110	0	0	110	-110	1.61E+06		
115	0	0	65	-65	1.66E+06		
120	0	0	75	-75	1.71E+06		
125	0	0	70	-70	1.76E+06		
130	0	0	80	-80	1.80E+06		
135	0	0	60	-60	1.85E+06		
140	0	0	60	-60	1.89E+06		
145	0	0	80	-80	1.93E+06		
150	0	0	85	-85	1.98E+06		
155	0	0	55	-55	2.02E+06		

1* Correct dead time τ = 34 ns: N1 = N0 / (1 – N0 * τ)
2* Correct dark count: N3 = N1 – N2

160			70		2.05E+06		
165			90		2.09E+06		
170			65		2.13E+06		
175			75		2.16E+06		
180			110		2.20E+06		
185			85		2.23E+06		
190			75		2.26E+06		
195			75		2.29E+06		
200			85		2.32E+06		
205			120		2.35E+06		
210			95		2.38E+06		
215			115		2.41E+06		
220			100		2.43E+06		
225			70		2.46E+06		
230			100		2.48E+06		
235			95		2.51E+06		
240			115		2.53E+06		
245			85		2.55E+06		
250			90		2.57E+06		
255			120		2.60E+06		
260			115		2.62E+06		
265			115		2.64E+06		
270			125		2.65E+06		
275			110		2.67E+06		
280			125		2.69E+06		
285			150		2.71E+06		
290			155		2.72E+06		
295			140		2.74E+06		
300			135		2.76E+06		
305			145		2.77E+06		
310			140		2.79E+06		
315			150		2.80E+06		
320			120		2.81E+06		
325			175		2.83E+06		
330			160		2.84E+06		
335			140		2.85E+06		
340			155		2.86E+06		
345			150		2.88E+06		
350			180		2.89E+06		
355			195		2.90E+06		
360			210		2.91E+06		
365			165		2.92E+06		
370			190		2.93E+06		
375			160		2.94E+06		
380			210		2.95E+06		
385			190		2.95E+06		

390			205		2.96E+06		
395			195		2.97E+06		
400			220		2.98E+06		
405			180		2.99E+06		
410			235		2.99E+06		
415			210		3.00E+06		
420			240		3.01E+06		
425			205		3.01E+06		
430			250		3.02E+06		
435			190		3.02E+06		
440			245		3.03E+06		
445			230		3.04E+06		
450			190		3.04E+06		
455			275		3.04E+06		
460			260		3.05E+06		
465			210		3.05E+06		
470			250		3.06E+06		
475			335		3.06E+06		
480			205		3.07E+06		
485			260		3.07E+06		
490			235		3.07E+06		
495			290		3.08E+06		
500			250		3.08E+06		
505			365		3.08E+06		
510			275		3.08E+06		
515			255		3.09E+06		
520			290		3.09E+06		
525			225		3.09E+06		
530			300		3.09E+06		
535			290		3.10E+06		
540			275		3.10E+06		
545			275		3.10E+06		
550			290		3.10E+06		
555			310		3.10E+06		
560			280		3.10E+06		
565			280		3.10E+06		
570			345		3.10E+06		
575			305		3.11E+06		
580			280		3.11E+06		
585			330		3.11E+06		
590			280		3.11E+06		
595			255		3.11E+06		
600			350		3.11E+06		
605			375		3.11E+06		
610			250		3.11E+06		
615			285		3.11E+06		

620			295		3.11E+06		
625			285		3.11E+06		
630			350		3.11E+06		
635			360		3.11E+06		
640			235		3.11E+06		
645			375		3.11E+06		
650			330		3.10E+06		
655			280		3.10E+06		
660			270		3.10E+06		
665			385		3.10E+06		
670			320		3.10E+06		
675			340		3.10E+06		
680			330		3.10E+06		
685			390		3.10E+06		
690			320		3.10E+06		
695			295		3.10E+06		
700			375		3.09E+06		
705			335		3.09E+06		
710			285		3.09E+06		
715			395		3.09E+06		
720			325		3.09E+06		
725			345		3.09E+06		
730			425		3.08E+06		
735			310		3.08E+06		
740			415		3.08E+06		
745			370		3.08E+06		
750			410		3.08E+06		
755			365		3.07E+06		
760			335		3.07E+06		
765			420		3.07E+06		
770			345		3.07E+06		
775			375		3.07E+06		
780			410		3.06E+06		
785			355		3.06E+06		
790			355		3.06E+06		
795			345		3.06E+06		
800			355		3.05E+06		
805			375		3.05E+06		
810			370		3.05E+06		
815			400		3.05E+06		
820			415		3.04E+06		
825			375		3.04E+06		
830			365		3.04E+06		
835			395		3.04E+06		
840			365		3.03E+06		
845			440		3.03E+06		

850			395		3.03E+06		
855			460		3.03E+06		
860			370		3.02E+06		
865			335		3.02E+06		
870			375		3.02E+06		
875			405		3.01E+06		
880			445		3.01E+06		
885			345		3.01E+06		
890			300		3.01E+06		
895			375		3.00E+06		
900			355		3.00E+06		
905			380		3.00E+06		
910			445		2.99E+06		
915			420		2.99E+06		
920			440		2.99E+06		
925			360		2.99E+06		
930			440		2.98E+06		
935			490		2.98E+06		
940			385		2.98E+06		
945			460		2.97E+06		
950			390		2.97E+06		
955			445		2.97E+06		
960			480		2.96E+06		
965			345		2.96E+06		
970			430		2.96E+06		
975			440		2.95E+06		
980			405		2.95E+06		
985			385		2.95E+06		
990			455		2.94E+06		
995			435		2.94E+06		
1000			400		2.94E+06		
1005			360		2.93E+06		
1010			405		2.93E+06		
1015			480		2.93E+06		
1020			405		2.92E+06		
1025			435		2.92E+06		
1030			410		2.92E+06		
1035			410		2.91E+06		
1040			420		2.91E+06		
1045			430		2.91E+06		
1050			430		2.90E+06		
1055			455		2.90E+06		
1060			455		2.90E+06		
1065			490		2.89E+06		
1070			395		2.89E+06		
1075			425		2.89E+06		

1080			500		2.88E+06		
1085			405		2.88E+06		
1090			420		2.88E+06		
1095			475		2.87E+06		
1100			395		2.87E+06		
1105			435		2.87E+06		
1110			380		2.86E+06		
1115			525		2.86E+06		
1120			470		2.86E+06		
1125			425		2.85E+06		
1130			480		2.85E+06		
1135			500		2.85E+06		
1140			365		2.84E+06		
1145			450		2.84E+06		
1150			450		2.84E+06		
1155			460		2.83E+06		
1160			500		2.83E+06		
1165			370		2.83E+06		
1170			435		2.82E+06		
1175			455		2.82E+06		
1180			415		2.82E+06		
1185			485		2.81E+06		
1190			485		2.81E+06		
1195			465		2.81E+06		
1200			445		2.80E+06		
1205			480		2.80E+06		
1210			390		2.80E+06		
1215			480		2.79E+06		
1220			505		2.79E+06		
1225			470		2.78E+06		
1230			535		2.78E+06		
1235			530		2.78E+06		
1240			460		2.77E+06		
1245			430		2.77E+06		
1250			455		2.77E+06		
1255			425		2.76E+06		
1260			495		2.76E+06		
1265			455		2.76E+06		
1270			450		2.75E+06		
1275			460		2.75E+06		
1280			480		2.75E+06		
1285			465		2.74E+06		
1290			415		2.74E+06		
1295			445		2.74E+06		
1300			485		2.73E+06		
1305			450		2.73E+06		

1310			490		2.73E+06		
1315			470		2.72E+06		
1320			465		2.72E+06		
1325			395		2.72E+06		
1330			455		2.71E+06		
1335			390		2.71E+06		
1340			495		2.71E+06		
1345			435		2.70E+06		
1350			485		2.70E+06		
1355			450		2.70E+06		
1360			535		2.69E+06		
1365			425		2.69E+06		
1370			425		2.69E+06		
1375			420		2.68E+06		
1380			430		2.68E+06		
1385			485		2.68E+06		
1390			455		2.67E+06		
1395			540		2.67E+06		
1400			510		2.67E+06		
1405			460		2.67E+06		
1410			535		2.66E+06		
1415			550		2.66E+06		
1420			480		2.66E+06		
1425			475		2.65E+06		
1430			440		2.65E+06		
1435			510		2.65E+06		
1440			520		2.64E+06		
1445			465		2.64E+06		
1450			505		2.64E+06		
1455			435		2.63E+06		
1460			465		2.63E+06		
1465			420		2.63E+06		
1470			390		2.63E+06		
1475			455		2.62E+06		
1480			515		2.62E+06		
1485			465		2.62E+06		
1490			540		2.61E+06		
1495			490		2.61E+06		
1500			495		2.61E+06		
1505			525		2.60E+06		
1510			445		2.60E+06		
1515			380		2.60E+06		
1520			475		2.60E+06		
1525			475		2.59E+06		
1530			430		2.59E+06		
1535			545		2.59E+06		

1540			520		2.58E+06		
1545			515		2.58E+06		
1550			475		2.58E+06		
1555			455		2.58E+06		
1560			545		2.57E+06		
1565			480		2.57E+06		
1570			455		2.57E+06		
1575			515		2.56E+06		
1580			535		2.56E+06		
1585			495		2.56E+06		
1590			595		2.56E+06		
1595			520		2.55E+06		
1600			465		2.55E+06		
1605			460		2.55E+06		
1610			450		2.54E+06		
1615			485		2.54E+06		
1620			460		2.54E+06		
1625			465		2.54E+06		
1630			455		2.53E+06		
1635			435		2.53E+06		
1640			460		2.53E+06		
1645			455		2.52E+06		
1650			450		2.52E+06		
1655			500		2.52E+06		
1660			515		2.52E+06		
1665			520		2.51E+06		
1670			500		2.51E+06		
1675			460		2.51E+06		
1680			400		2.51E+06		
1685			485		2.50E+06		
1690			545		2.50E+06		
1695			440		2.50E+06		
1700			480		2.49E+06		
1705			455		2.49E+06		
1710			515		2.49E+06		
1715			530		2.49E+06		
1720			580		2.48E+06		
1725			435		2.48E+06		
1730			530		2.48E+06		
1735			510		2.47E+06		
1740			410		2.47E+06		
1745			480		2.47E+06		
1750			500		2.47E+06		
1755			510		2.46E+06		
1760			455		2.46E+06		
1765			430		2.46E+06		

1770			460		2.46E+06		
1775			480		2.45E+06		
1780			590		2.45E+06		
1785			505		2.45E+06		
1790			525		2.44E+06		
1795			465		2.44E+06		
1800			495		2.44E+06		
1805			495		2.44E+06		
1810			480		2.43E+06		
1815			470		2.43E+06		
1820			450		2.43E+06		
1825			510		2.43E+06		
1830			515		2.42E+06		
1835			440		2.42E+06		
1840			465		2.42E+06		
1845			515		2.41E+06		
1850			490		2.41E+06		
1855			500		2.41E+06		
1860			430		2.41E+06		
1865			495		2.40E+06		
1870			480		2.40E+06		
1875			485		2.40E+06		
1880			540		2.40E+06		
1885			470		2.39E+06		
1890			480		2.39E+06		
1895			535		2.39E+06		
1900			445		2.39E+06		
1905			530		2.38E+06		
1910			590		2.38E+06		
1915			455		2.38E+06		
1920			510		2.37E+06		
1925			470		2.37E+06		
1930			490		2.37E+06		
1935			450		2.37E+06		
1940			545		2.36E+06		
1945			440		2.36E+06		
1950			515		2.36E+06		
1955			500		2.36E+06		
1960			555		2.35E+06		
1965			505		2.35E+06		
1970			410		2.35E+06		
1975			455		2.35E+06		
1980			495		2.34E+06		
1985			540		2.34E+06		
1990			490		2.34E+06		
1995			500		2.34E+06		

2000			520		2.33E+06		
2005			465		2.33E+06		
2010			480		2.33E+06		
2015			495		2.33E+06		
2020			455		2.32E+06		
2025			435		2.32E+06		
2030			525		2.32E+06		
2035			505		2.32E+06		
2040			435		2.31E+06		
2045			465		2.31E+06		
2050			555		2.31E+06		
2055			520		2.30E+06		
2060			440		2.30E+06		
2065			515		2.30E+06		
2070			520		2.30E+06		
2075			530		2.29E+06		
2080			510		2.29E+06		
2085			465		2.29E+06		
2090			510		2.29E+06		
2095			485		2.29E+06		
2100			490		2.28E+06		
2105			560		2.28E+06		
2110			515		2.28E+06		
2115			520		2.28E+06		
2120			440		2.27E+06		
2125			550		2.27E+06		
2130			470		2.27E+06		
2135			550		2.27E+06		
2140			475		2.26E+06		
2145			525		2.26E+06		
2150			515		2.26E+06		
2155			520		2.26E+06		
2160			465		2.25E+06		
2165			485		2.25E+06		
2170			480		2.25E+06		
2175			555		2.25E+06		
2180			475		2.24E+06		
2185			535		2.24E+06		
2190			495		2.24E+06		
2195			480		2.24E+06		
2200			595		2.23E+06		
2205			450		2.23E+06		
2210			465		2.23E+06		
2215			435		2.23E+06		
2220			475		2.23E+06		
2225			470		2.22E+06		

2230			445		2.22E+06		
2235			505		2.22E+06		
2240			460		2.22E+06		
2245			495		2.21E+06		
2250			585		2.21E+06		
2255			540		2.21E+06		
2260			515		2.21E+06		
2265			460		2.20E+06		
2270			495		2.20E+06		
2275			540		2.20E+06		
2280			510		2.20E+06		
2285			570		2.20E+06		
2290			480		2.19E+06		
2295			465		2.19E+06		
2300			520		2.19E+06		
2305			555		2.19E+06		
2310			490		2.18E+06		
2315			490		2.18E+06		
2320			530		2.18E+06		
2325			465		2.18E+06		
2330			380		2.18E+06		
2335			525		2.17E+06		
2340			465		2.17E+06		
2345			485		2.17E+06		
2350			495		2.17E+06		
2355			515		2.16E+06		
2360			480		2.16E+06		
2365			505		2.16E+06		
2370			530		2.16E+06		
2375			500		2.16E+06		
2380			530		2.15E+06		
2385			545		2.15E+06		
2390			550		2.15E+06		
2395			445		2.15E+06		
2400			515		2.14E+06		
2405			470		2.14E+06		
2410			460		2.14E+06		
2415			520		2.14E+06		
2420			525		2.14E+06		
2425			510		2.13E+06		
2430			460		2.13E+06		
2435			535		2.13E+06		
2440			400		2.13E+06		
2445			410		2.13E+06		
2450			580		2.12E+06		
2455			525		2.12E+06		

2460			495		2.12E+06		
2465			510		2.12E+06		
2470			440		2.12E+06		
2475			480		2.11E+06		
2480			505		2.11E+06		
2485			395		2.11E+06		
2490			515		2.11E+06		
2495			440		2.10E+06		
2500			635		2.10E+06		
2505			525		2.10E+06		
2510			495		2.10E+06		
2515			570		2.10E+06		
2520			520		2.09E+06		
2525			545		2.09E+06		
2530			520		2.09E+06		
2535			535		2.09E+06		
2540			540		2.09E+06		
2545			570		2.08E+06		
2550			525		2.08E+06		
2555			450		2.08E+06		
2560			495		2.08E+06		
2565			545		2.08E+06		
2570			530		2.07E+06		
2575			560		2.07E+06		
2580			505		2.07E+06		
2585			505		2.07E+06		
2590			600		2.07E+06		
2595			485		2.06E+06		
2600			525		2.06E+06		
2605			535		2.06E+06		
2610			475		2.06E+06		
2615			540		2.06E+06		
2620			535		2.05E+06		
2625			465		2.05E+06		
2630			505		2.05E+06		
2635			515		2.05E+06		
2640			515		2.05E+06		
2645			500		2.05E+06		
2650			540		2.04E+06		
2655			440		2.04E+06		
2660			475		2.04E+06		
2665			525		2.04E+06		
2670			565		2.04E+06		
2675			460		2.03E+06		
2680			500		2.03E+06		
2685			520		2.03E+06		

2690			480		2.03E+06		
2695			505		2.03E+06		
2700			530		2.02E+06		
2705			540		2.02E+06		
2710			505		2.02E+06		
2715			560		2.02E+06		
2720			485		2.02E+06		
2725			560		2.02E+06		
2730			505		2.01E+06		
2735			500		2.01E+06		
2740			495		2.01E+06		
2745			480		2.01E+06		
2750			575		2.01E+06		
2755			480		2.00E+06		
2760			445		2.00E+06		
2765			505		2.00E+06		
2770			405		2.00E+06		
2775			545		2.00E+06		
2780			500		1.99E+06		
2785			460		1.99E+06		
2790			570		1.99E+06		
2795			480		1.99E+06		
2800			495		1.99E+06		
2805			535		1.99E+06		
2810			555		1.98E+06		
2815			500		1.98E+06		
2820			510		1.98E+06		
2825			480		1.98E+06		
2830			585		1.98E+06		
2835			590		1.98E+06		
2840			450		1.97E+06		
2845			550		1.97E+06		
2850			510		1.97E+06		
2855			520		1.97E+06		
2860			575		1.97E+06		
2865			495		1.96E+06		
2870			455		1.96E+06		
2875			525		1.96E+06		
2880			465		1.96E+06		
2885			525		1.96E+06		
2890			505		1.96E+06		
2895			530		1.95E+06		
2900			515		1.95E+06		
2905			550		1.95E+06		
2910			510		1.95E+06		
2915			530		1.95E+06		

2920			520		1.95E+06		
2925			535		1.94E+06		
2930			520		1.94E+06		
2935			565		1.94E+06		
2940			570		1.94E+06		
2945			520		1.94E+06		
2950			500		1.94E+06		
2955			445		1.93E+06		
2960			630		1.93E+06		
2965			540		1.93E+06		
2970			500		1.93E+06		
2975			505		1.93E+06		
2980			450		1.93E+06		
2985			525		1.92E+06		
2990			540		1.92E+06		
2995			475		1.92E+06		
3000			505		1.92E+06		
3005			475		1.92E+06		
3010			600		1.92E+06		
3015			470		1.91E+06		
3020			520		1.91E+06		
3025			525		1.91E+06		
3030			530		1.91E+06		
3035			485		1.91E+06		
3040			490		1.91E+06		
3045			560		1.90E+06		
3050			535		1.90E+06		
3055			485		1.90E+06		
3060			590		1.90E+06		
3065			495		1.90E+06		
3070			510		1.90E+06		
3075			515		1.89E+06		
3080			470		1.89E+06		
3085			490		1.89E+06		
3090			585		1.89E+06		
3095			525		1.89E+06		
3100			565		1.89E+06		
3105			475		1.89E+06		
3110			540		1.88E+06		
3115			510		1.88E+06		
3120			515		1.88E+06		
3125			505		1.88E+06		
3130			540		1.88E+06		
3135			445		1.88E+06		
3140			535		1.87E+06		
3145			485		1.87E+06		

3150			485		1.87E+06		
3155			515		1.87E+06		
3160			550		1.87E+06		
3165			420		1.87E+06		
3170			530		1.87E+06		
3175			495		1.86E+06		
3180			505		1.86E+06		
3185			555		1.86E+06		
3190			515		1.86E+06		
3195			460		1.86E+06		
3200			530		1.86E+06		

Appendix 2: Intensity response function of the PHI 680 SAN output from the NPL AES Intensity Calibration Software, A1 V2.0 (r27), 1998, National Physical Lab, written by P.J. Cumpson and R.E. Shawyer. (page 163 ~ page 167)

CERTIFICATE OF CALIBRATION

ISSUED by UTK

DATE OF ISSUE: Sun 11/06/05 SERIAL NUMBER 1/0/7

Checksum: C3857-341-22479-4716-48-AQ4F4089 APPROVED SIGNATORY

Calibration For:

Calibrating Laboratory
UTK
1414 Circle Dr. Rm. 232
Knoxville
TN 37996-0840
U.S.A.

Order Number:

AES Spectrometer Intensity Calibration

This certificate describes the Intensity/Energy response function, Q(E), derived using NPL software A1 V2.0 (r27) (see *J. Elec. Spectrosc.* **71**, 191-204, 1995). Kinetic energy *E* is referred to the Fermi level. This calibration is for AES data recorded in accordance with the Spectrum Acquisition Guide.

1. Details of Instrument and Calibration Conditions

Instrument owned by:
Instrument Model: Serial Number:
Analyser Type : CMA Signal Mode: Pulse Counting
Anal. Mode: FRR Retard Ratio: 1
Slit Identifier, etc:

This calibration was performed by Yinghong Lin.
Spectra used for the calibration were acquired on 02/11/2005 by Yinghong Lin.
These spectra were acquired from reference material SCAA87, batch number: ,
using a Channel Electron Multiplier (CEM) voltage of : 2300V.

The relative uncertainty in the energy dependence of Q(E) (based on a standard uncertainty multplied by a coverage factor of k = 2, which provides a level of confidence of approximately 95%), ignoring the uncertainty of the method, U_I, is 11.2%.

Copyright of this certificate is owned jointly by the Crown and the issuing laboratory and it may not be reproduced other than in full except with the prior written approval of the issuing laboratory and the Chief Executive Officer of NPL.

CERTIFICATE OF CALIBRATION

SERIAL NUMBER 1/0/7

Checksum: C3857-341-22479-4716-48-AQ4F4089

Names of the files used in this calibration follow. Units are either counts (C) or counts per second (CPS).
100_AG.ASC(CPS) 103_CU.ASC(CPS) 105_AU.ASC(CPS)

Ag Energy Range: 2eV-2500eV
Ag i_B / nA 1.1130000E+01
Ag Δ values Not Applicable

Cu Energy Range: 2eV-2500eV
Cu i_B / nA 1.1130000E+01
Cu Δ values Not Applicable

Au Energy Range: 2eV-2500eV
Au i_B / nA 1.1130000E+01
Au Δ values Not Applicable

2. Calibrated Spectrometer Response Function Q(E)

Over the interval E_{min} to E_{max} (the values of which are on page 3 of this certificate), Q(E) is given by:

$$Q(E)/E = \frac{a_0 + a_1\varepsilon + a_2\varepsilon^2 + a_3\varepsilon^3 + a_4\varepsilon^4}{1 + b_1\varepsilon + b_2\varepsilon^2 + b_3\varepsilon^3 + b_4\varepsilon^4} \quad \text{Ao/eV units}$$

where $\varepsilon = (E - 1000\text{eV}) / 1000\text{eV}$,

$a_0 = +5.363159$

$a_1 = +5.874861$	$b_1 = +1.298816$
$a_2 = -2.187136$	$b_2 = -0.094891$
$a_3 = -2.714023$	$b_3 = -0.601437$
$a_4 = -0.008793$	$b_4 = -0.136697$

Note that 1 Ao unit = 3.14×10^{-4} ($\pm 0.19 \times 10^{-4}$) sr eV. Values for Q(E) in the case of FAT, or Q(E)/E in the case of FRR, from this calibration have been filed at 1eV intervals, as a digital annex to this certificate under the file name Q_FRR.VMS.

The reported uncertainty is based on a standard uncertainty multplied by a coverage factor of k = 2, which provides a level of confidence of approximately 95%.

CERTIFICATE OF CALIBRATION

SERIAL NUMBER 1/0/7

Checksum: C3857-341-22479-4716-48-AQ4F4089

3. Supplementary Data

For definition of terms see the User's Guide and *J. Elec. Spectrosc.* **71**, 191-204, 1995.

Quantity	Symbol	Units	Value
Minimum valid calibration energy	E_{min}	eV	20
Maximum valid calibration energy	E_{max}	eV	2500
Response at E = 1000eV	Q(1000eV)	Ao/eV	5.3632E+3
Percentage rms scatter	r	%	1.577
Energy calibration shift indicated	ΔE_{ind}	eV	+2.00
Energy calibration shift used	ΔE_{used}	eV	+2.00
Spectrometer dead time	τ	ns	32.8
Divergence from the means	$\bar{R}_{Ag}$		1.025
	$\bar{R}_{Au}$		0.982
	$\bar{R}_{Cu}$		0.993
Scattering diagnosis f-values	f(329,Ag)		0.097
	f(879,Cu)		0.094

The absolute uncertainty in the scale of Q(E) depends on the accuracy of the primary beam current measurements. Ignoring any systematic error in the ammeter calibration, the absolute uncertainty in Q(E) can be estimated from the Δ values (page 2) and the divergences from the means, as a percentage. In this calibration this absolute uncertainty, Ua, is 12.1%.

The reported uncertainty is based on a standard uncertainty multplied by a coverage factor of k = 2, which provides a level of confidence of approximately 95%.

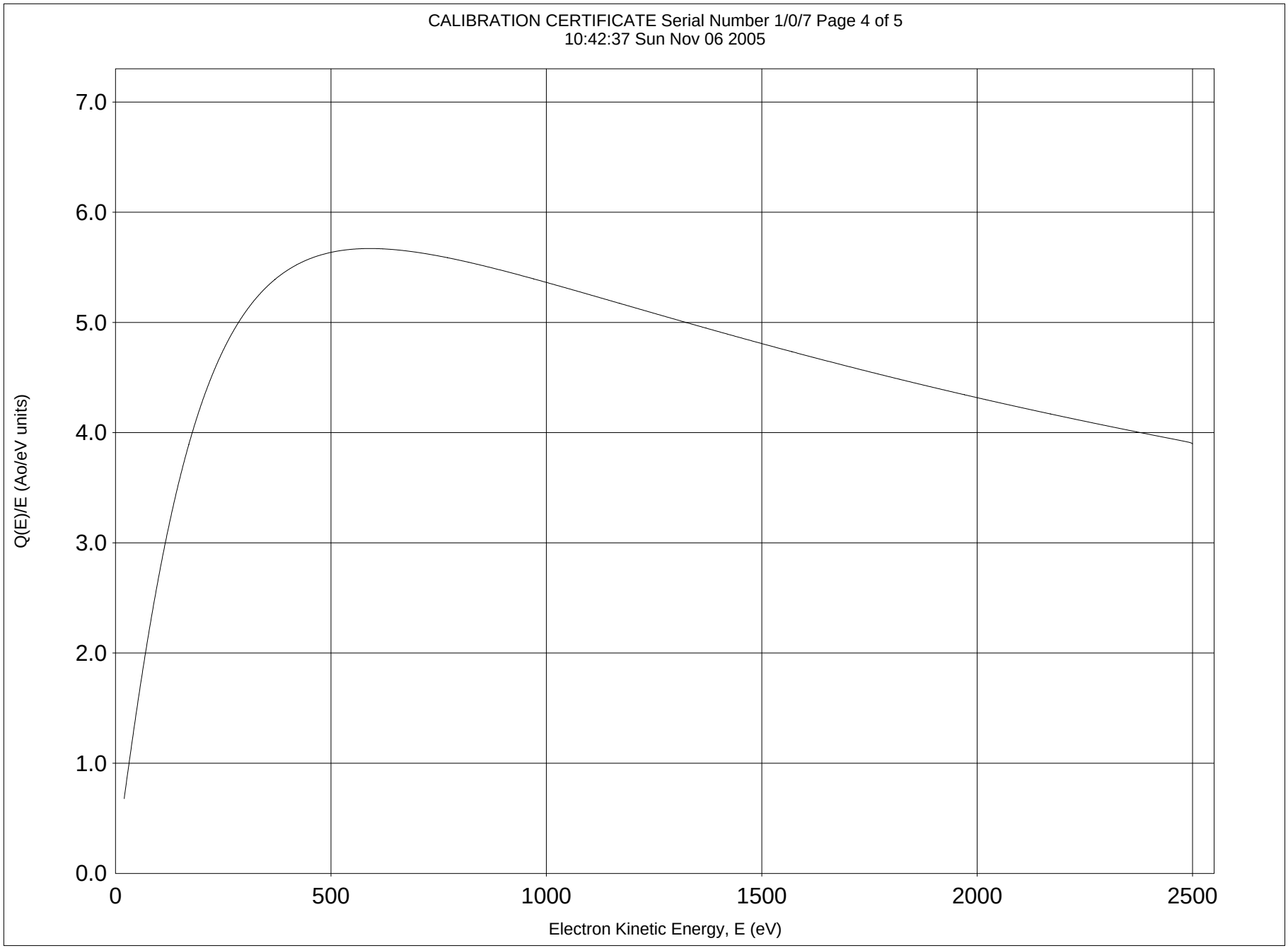
7.0
6.0
5.0
4.0
3.0
2.0
1.0
0.0
Q(E)/E (Ao/eV units)
0
500
1000
1500
2000
2500
Electron Kinetic Energy, E (eV)

10:42:37 Sun Nov 06 2005

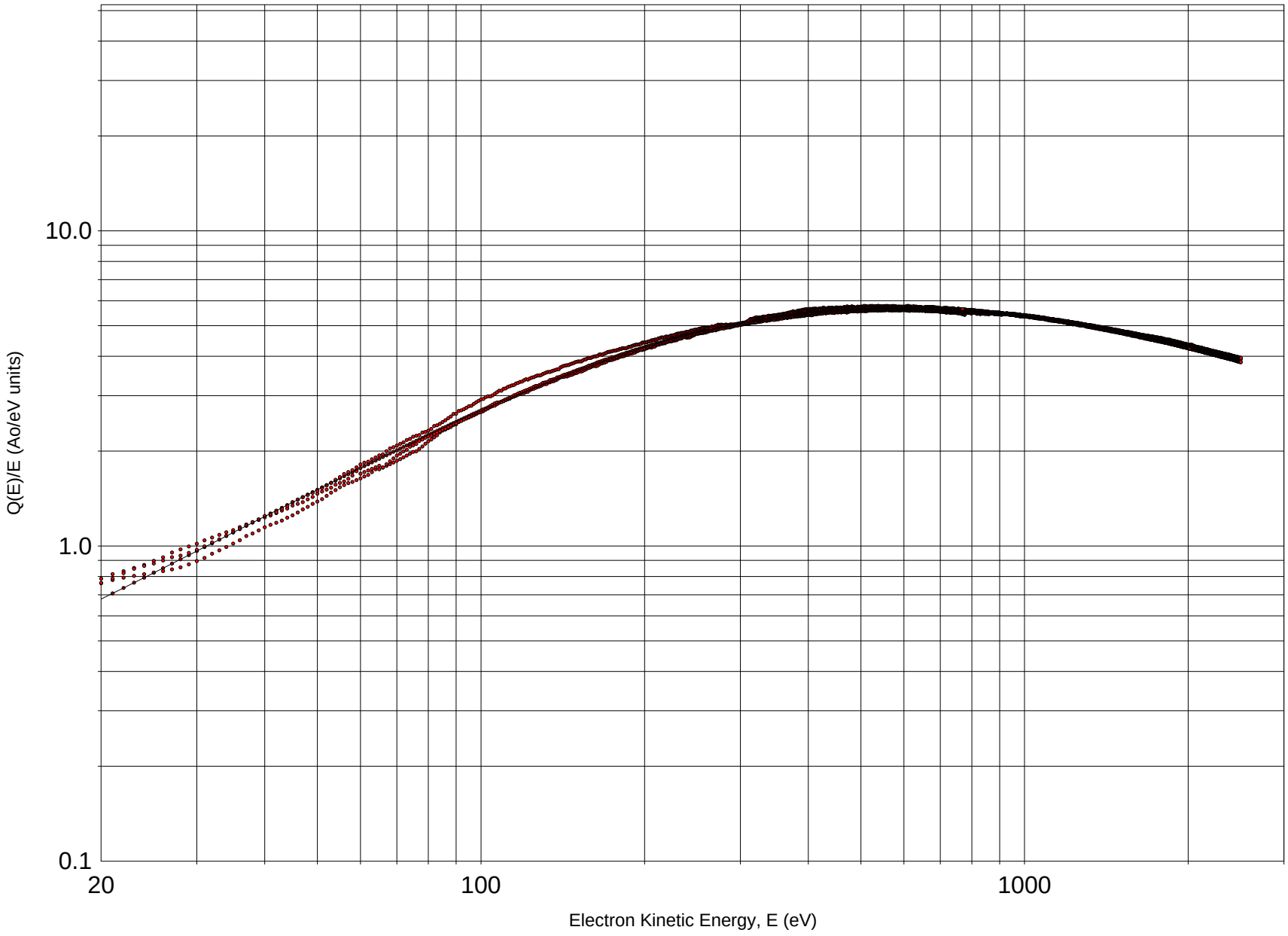

Vita

Yinghong Lin was born in Hubei, China on January 11, 1976. She gained her Bachelor's degree in Materials Science and Engineering in 1999 from the Powder Metallurgy Research Institute of the Central South University (CSU), Changsha, China. Her graduating project was fabrication of Li-B alloy as a potential electrode material for fuel cells. As an undergraduate acquired top GPA among peer students, she was awarded the Baogang National Outstanding College Student Scholarship in 1998. She was admitted to the graduate program of the same institute in CSU in 1999 with entrance exam exempted and completed her Master's degree in July, 2002. Her Master's research was focused on the structure evolution of aluminum alloys under simultaneous rapid solidification and deformation and was advised by Dr. Baiyun Huang, academician of Chinese Academic of Engineering. She started her research advised by Dr. David. C. Joy in January, 2003 in the department of Materials Science Engineering at the University of Tennessee, Knoxville, USA. Her research was focused on the electron-solid interactions and the secondary electrons. She gained her PhD degree in December, 2007. During summer of 2006, she interned at KLA-Tencor, a leading semiconductor inspection company in San Jose, CA on a project closely related to her thesis research.